# Measurement of Nuclear Reaction Cross Sections for Applications in Radiotherapy with Protons, Helium and Carbon Ions

**Dissertation**

vorgelegt von **Felix Ernst Horst**

zur Erlangung des akademischen Grades
**Doktor der Naturwissenschaften (Dr. rer. nat.)**

am Fachbereich **Mathematik und Informatik, Physik, Geographie**
der **Justus-Liebig-Universität Giessen**
in Kooperation mit der **Technischen Hochschule Mittelhessen**
und dem **GSI Helmholtzzentrum für Schwerionenforschung**

Referent: **Prof. Dr. Kai-Thomas Brinkmann**
Korreferent: **Prof. Dr. Klemens Zink**

Giessen, den 20.12.2019

**Measurement of Nuclear Reaction Cross Sections for Applications in Radiotherapy with Protons, Helium and Carbon Ions**

**Messung von Kernreaktionsquerschnitten für Anwendungen in der Strahlentherapie mit Protonen, Helium- und Kohlenstoffionen**

**Tag der Disputation:** 27.02.2020

**Prüfungskommission:**
Prof. Dr. Kai-Thomas Brinkmann
Prof. Dr. Klemens Zink
Prof. Dr. Christoph Scheidenberger
Prof. Dr. Marco Durante

## Abstract

This thesis studies nuclear fragmentation induced by protons, $^{4}$He and $^{12}$C ions in the energy range used for radiotherapy through two different experimental setups. A comprehensive understanding of these nuclear reactions is essential for accurate dose calculation in patients and for verification of the treatment via positron emission tomography (PET).
In the first experiment, conducted at the Heidelberger Ionenstrahl-Therapiezentrum, charge- and mass-changing cross sections were measured for the colliding systems $^{4}$He $+^{1}$ H, $^{4}$He $+^{12}$ C, $^{4}$He $+^{16}$ O and $^{4}$He $+^{28}$ Si in the energy range of $70 - 220$ MeV/u. The cross sections were obtained via the attenuation method where a $\Delta$E $-$ E scintillator telescope was used for particle identification. These data will have particular relevance for future applications of $^{4}$He ions in ion beam radiotherapy as this technique relies on precise nuclear reaction models for an accurate dose calculation. The widely used parametrization for the total reaction cross section $\sigma_R$ by Tripathi et al. under-predicts the new experimental cross sections for $^{4}$He ions in the therapeutic energy range by up to 30%, which can lead to considerable dose calculation uncertainties. Therefore, the parameters in the Tripathi model were optimized and the FLUKA nuclear reaction model was adjusted accordingly. The new models were validated by comparing radiation transport calculations against available $^{4}$He depth dose measurements. The impact of the nuclear model changes for $^{4}$He ions on their relative biological effectiveness was studied through radiobiological calculations based on the local effect model.
In the second experiment, conducted at the Marburger Ionenstrahl-Therapiezentrum, cross sections were measured for the production of $^{10}$C, $^{11}$C and $^{15}$O by protons ($40 - 220$ MeV) and $^{12}$C ions ($65 - 430$ MeV/u) on C and O targets. The cross sections were obtained via activation measurements of irradiated graphite and BeO targets using a set of three scintillators coupled by a coincidence logic. The measured cross sections are relevant for the particle range verification method by PET where accurate predictions of the $\beta^{+}$-emitter distribution produced by therapeutic beams in the patient tissue are required. This dataset will be useful for validation and optimization of proton-nucleus and nucleus-nucleus reaction models within radiation transport codes. For protons there is a good agreement between a radiation transport calculation using the measured cross sections and a thick target PET measurement from the literature. For $^{12}$C-induced nuclear reactions the novel cross sections are a good basis for further model developments.

## Zusammenfassung

Die vorliegende Arbeit handelt von Untersuchungen zur Kernfragmentierung induziert durch Protonen, $^4$He- und $^{12}$C-Ionen im zur Strahlentherapie genutzten Energiebereich mittels zweier unterschiedlicher Experimente. Ein umfangreiches Verständnis derartiger Kernreaktionen ist die Voraussetzung für eine genaue Dosisberechnung im Patienten sowie für die Therapie-Verifikation mittels Positronen-Emissions-Tomographie (PET).
In der ersten Messreihe, durchgeführt am Heidelberger Ionenstrahl-Therapiezentrum, wurden Wirkungsquerschnitte (Ladungs- und Massenänderung) für die Systeme $^4\mathrm{He} +^1 \mathrm{H}$, $^4\mathrm{He} +^{12} \mathrm{C}$, $^4\mathrm{He} +^{16} \mathrm{O}$ und $^4\mathrm{He} +^{28} \mathrm{Si}$ im Energiebereich $70 - 220$ MeV/u bestimmt. Diese Wirkungsquerschnitte wurden mit der Schwächungsmethode ermittelt, wobei ein $\Delta\mathrm{E} - \mathrm{E}$ Szintillatorteleskop zur Teilchenidentifikation verwendet wurde. Die so gewonnenen Daten haben besondere Relevanz für zukünftige Anwendungen von $^4$He-Ionen in der Partikeltherapie, da diese Technik auf präzise Kernreaktionsmodelle für eine genaue Dosisberechnung angewiesen ist. Die weit verbreitete Parametrisierung des totalen Reaktionsquerschnitts $\sigma_R$ von Tripathi et al. unterschätzt die neuen experimentellen Wirkungsquerschnitte für $^4$He-Ionen im therapeutischen Energiebereich um bis zu 30%, was zu erheblichen Unsicherheiten in der Dosisberechnungs führen kann. Daher wurden die Parameter im Tripathi-Modell sowie das Modell in FLUKA auf Basis der neuen Wirkungsquerschnitte optimiert. Die optimierten Modelle wurden durch den Vergleich von Strahlungstransportrechnungen mit veröffentlichten $^4$He-Tiefendosismessungen validiert. Die Auswirkungen der Anpassung der nuklearen Modelle für $^4$He-Ionen auf deren relative biologische Wirksamkeit wurden durch strahlenbiologische Berechnungen auf Grundlage des Local Effect Modells untersucht.
In der zweiten Messreihe am Marburger Ionenstrahl-Therapiezentrum wurden Wirkungsquerschnitte für die Produktion von $^{10}$C, $^{11}$C und $^{15}$O durch Protonen ($40 - 220$ MeV) und $^{12}$C-Ionen ($65 - 430$ MeV/u) an C und O Targets bestimmt. Diese wurden durch Aktivierungsmessungen von bestrahlten Graphit- und BeO-Targets unter Verwendung eines Aufbaus aus drei Szintillatoren, gekoppelt durch eine Koinzidenzlogik, ermittelt. Die gemessenen Produktionsquerschnitte sind für die in-vivo-Reichweitenverifikationsmethode mittels PET relevant. Bei dieser sind genaue Vorhersagen der $\beta^+$-Emitterverteilung, die vom therapeutischen Strahl im Patientengewebe erzeugt wird, erforderlich. Auch dieser Datensatz ist nützlich für die Validierung und Optimierung von Proton-Kern- and Kern-Kern-Reaktionsmodellen in Strahlungstransport-Codes. Für Protonen stimmen Strahlungstransportrechnungen unter Verwendung der gemessenen Produktionsquerschnitte gut mit der PET-Messung eines bestrahlten dicken Targets aus der Literatur überein. Für $^{12}$C-induzierte Kernreaktionen sind die neu gewonnenen Wirkungsquerschnitte eine gute Grundlage zur Weiterentwicklung von Modellen.

# Contents

**List of Figures** **V**

**List of Tables** **VI**

**1 Introduction** **1**

**2 Theoretical Background** **3**
2.1 Radiotherapy with Protons and Heavy Ions . . . 3
2.2 History of Proton and Heavy Ion Therapy . . . 5
2.3 Interaction of Heavy Charged Particles with Matter . . . 9
2.3.1 Electronic Energy Loss . . . 9
2.3.2 Elastic Scattering . . . 12
2.3.3 Nuclear Fragmentation . . . 13
2.3.3.1 Activation . . . 14
2.3.3.2 Influence on Dose Profiles . . . 15
2.3.3.3 Data Situation with Regard to Particle Therapy . . . 16
2.4 Radiobiological Aspects . . . 16
2.4.1 Local Effect Model . . . 18
2.4.2 RBE Effects on Dose Profiles . . . 19
2.5 Dose Calculation Methods . . . 20
2.5.1 Pencil Beam Algorithms . . . 21
2.5.2 Monte Carlo Radiation Transport Simulation . . . 22
2.6 Radiotherapy with Helium Ions . . . 23
2.7 PET Range Verification . . . 24
2.8 Nuclear Reaction Cross Sections . . . 26
2.8.1 Cross Section Definitions . . . 26
2.8.2 Parametrization of the Total Reaction Cross Section . . . 27
2.8.2.1 Geometrical Model by Bradt and Peters . . . 27
2.8.2.2 Parametrization by Tripathi . . . 28
2.9 Synergies with Space Radiation Research . . . 29
2.10 Scintillation Detectors . . . 30
2.10.1 Plastic Scintillators . . . 30
2.10.2 $BaF_2$ Scintillators . . . 30
2.10.3 Particle Identification with Scintillator Telescopes . . . 31

**3 Materials and Methods** **33**
3.1 Data Acquisition . . . 33
3.2 Data Processing . . . 33
3.3 $BaF_2$ Pulse Shape Analysis . . . 33
3.4 Experimental Setup I: Projectile Fragmentation . . . 34
3.4.1 Targets . . . 36
3.4.2 Alignment and Beamspot Characterization with CMOS Sensor . . . 37
3.4.3 Data Analysis . . . 38
3.4.3.1 Selection of Valid Triggers . . . 38

3.4.3.2 Identification of He ions . . . 39
3.4.3.3 Separation of the Identified He Ions into $^{3}$He and $^{4}$He . . . 42
3.4.3.4 Cross Section Calculation . . . 43
3.4.3.5 Uncertainty Estimation . . . 43
3.5 Experimental Setup II: Target Fragmentation . . . 44
3.5.1 The Measurement Concept . . . 44
3.5.2 Experimental Setup . . . 45
3.5.3 Beam Application . . . 45
3.5.4 Coincidence Trigger and Data Acquisition . . . 46
3.5.5 Targets . . . 48
3.5.6 Beamspot Characterization . . . 49
3.5.7 Efficiency Calculation . . . 50
3.5.8 Data Analysis . . . 52
3.5.8.1 Cross Section Calculation . . . 52
3.5.8.2 Uncertainty Estimation . . . 53
3.6 Radiation Transport Calculations . . . 53
3.6.1 Monte Carlo Codes Geant4 and FLUKA . . . 53
3.6.2 Treatment Planning System TRiP98 . . . 54
3.6.3 Depth Dose Profiles by $^{4}$He Ions in Water . . . 55
3.6.4 RBE Profiles by $^{4}$He Ions . . . 55
3.6.5 PET Isotope Production by Protons in a Tissue Phantom . . . 55

**4 Results and Discussion** **57**
4.1 Projectile Fragmentation Experiments . . . 57
4.1.1 He and $^{4}$He Attenuation Curves . . . 57
4.1.2 Charge- and Mass-Changing Cross Sections for $^{4}$He Ions . . . 58
4.1.3 Optimization of Tripathi Parametrization . . . 61
4.2 Target Fragmentation Experiments . . . 62
4.2.1 Measured Decay Curves of Activated Targets . . . 62
4.2.2 PET Isotope Production Cross Sections . . . 63
4.3 Radiation Transport Calculations . . . 69
4.3.1 Nuclear Reaction Model Optimization for $^{4}$He Ions . . . 69
4.3.1.1 Validation of Optimized Tripathi Parametrization . . . 69
4.3.1.2 Optimization of the $^{4}$He Nuclear Reaction Model in FLUKA 72
4.3.1.3 Impact of Nuclear Model Adjustments on $^{4}$He RBE Profiles 73
4.3.2 PET Isotope Production by Protons . . . 75

**5 Conclusion and Outlook** **77**

**Bibliography** **IX**

# List of Figures


2.1 Depth dose profiles of photons, protons, $^4$He and $^{12}$C ions . . . . . 4
2.2 Lateral dose profiles of photons, protons, $^4$He and $^{12}$C ions . . . . . 5
2.3 Photographs of heavy ion treatment in Berkeley and Marburg . . . . . 6
2.4 Energy loss of protons, $^4$He and $^{12}$C ions in water . . . . . 9
2.5 CSDA ranges of protons, $^4$He and $^{12}$C ions in water . . . . . 10
2.6 Energy loss distribution by protons, $^4$He and $^{12}$C ions in a thin water slice 11
2.7 Broadening of proton, $^4$He and $^{12}$C pencil beams due to elastic scattering . 12
2.8 Illustration of nuclear fragmentation reactions for protons, $^4$He and $^{12}$C ions 13
2.9 Influence of nuclear reaction model on a $^4$He SOBP . . . . . 15
2.10 Photon and heavy ion cell survival curves . . . . . 17
2.11 Absorbed dose and RBE-weighted dose profiles by protons, $^4$He and $^{12}$C ions 19
2.12 Activity profiles produced in PMMA by protons and $^{12}$C ions . . . . . 25
2.13 Photo of $BaF_2$ crystal . . . . . 31

3.1 Measured $BaF_2$ signals recorded for protons, $^4$He and $^{12}$C ions . . . . . 34
3.2 Schematic and photo of the experimental setup used at HIT for $^4$He fragmentation measurements . . . . . 35
3.3 Signal waveforms of start, $\Delta$E and E detectors . . . . . 35
3.4 Photo of the experimental setup used at HIT for measuring $^4$He fragmentation in a $H_2O$ target . . . . . 37
3.5 $^4$He beamspots at low intensity measured with a CMOS sensor . . . . . 37
3.6 Accepted trigger rate of the data acquisition system as a function of time during a $^4$He ion experiment at HIT . . . . . 38
3.7 Identification of primary $^4$He events with the start scintillator . . . . . 39
3.8 Examples of $\Delta$E-E spectra and $\Delta$E-pulse-shape spectra for $^4$He ions with and without target . . . . . 40
3.9 $\Delta$E spectra for $^4$He ions with and without target . . . . . 42
3.10 Schematic of the experimental setup for measuring production cross sections for PET isotopes at MIT . . . . . 45
3.11 Flow chart of the trigger logic for the activation experiments at MIT . . . 46
3.12 Waveforms for the three scintillator channels for 180° and 90° coincidence events . . . . . 47
3.13 Energy spectra of the events detected by the 180° detector pair and by the 90° detector pair . . . . . 47
3.14 Decay curve of the $\beta^+$-activity induced by protons in a graphite target . . 48
3.15 Proton and $^{12}$C ion beamspots measured with EBT3 films . . . . . 49
3.16 Illustration of the spatial distribution of the produced activity on the detection efficiency . . . . . 51

4.1 $^4$He attenuation curves in C and $H_2O$ targets . . . . . 57
4.2 Measured charge- and mass-changing cross sections for $^4$He ions on C, O, Si and H targets . . . . . 59
4.3 Measured decay curves of graphite and BeO targets irradiated with protons and $^{12}$C ions . . . . . 62

4.4 $^{10}$C and $^{11}$C production cross sections for protons on C targets . . . . . 64
4.5 $^{10}$C and $^{11}$C production cross sections for $^{12}$C ions on C targets . . . . . 65
4.6 Ratio of the $^{10}$C and $^{11}$C production cross sections for protons and $^{12}$C ions on C targets . . . . . 66
4.7 $^{15}$O production cross sections for protons and $^{12}$C ions on O targets . . . . 67
4.8 $^{4}$He Bragg curves in water calculated with Geant4 compared to HIT measurements . . . . . 70
4.9 $^{4}$He SOBP in water calculated with Geant4 compared to HIT measurements 70
4.10 $^{4}$He Bragg curves in water calculated with Geant4 compared to Berkeley measurements . . . . . 71
4.11 $^{4}$He Bragg curve in water calculated with TRiP98 for 192 MeV/u $^{4}$He ions 71
4.12 $^{4}$He Bragg curves in water calculated with FLUKA compared to HIT measurements . . . . . 72
4.13 $^{4}$He RBE profiles calculated with TRiP98 for 192 MeV/u $^{4}$He ions . . . . . 73
4.14 Dose-averaged linear energy transfer profiles calculated with TRiP98 for 192 MeV/u $^{4}$He ions . . . . . 74
4.15 Cross section models for $^{12}$C(p, pn)$^{11}$C and $^{16}$O(p, pn)$^{15}$O reactions . . . . 75
4.16 Calculated activity profiles produced by protons in a tissue phantom compared with PET measurements . . . . . 76

# List of Tables

3.1 List of targets used for $^{4}$He cross section measurements. . . . . 36

4.1 $^{4}$He mass- and charge-changing cross sections on C, $CH_2$, Si, $SiO_2$, $H_2O$, H and O targets . . . . . 58
4.2 $^{4}$He charge- and mass-changing cross sections on $H_2O$ targets . . . . . 60
4.3 Measured $^{10}$C and $^{11}$C production cross sections for protons and $^{12}$C ions on C targets . . . . . 68
4.4 Measured $^{15}$O production cross sections for protons and $^{12}$C ions on O targets 68

# 1 Introduction

Cancer remains to be one of the most severe health problems and its incidence is steadily growing. Killing of the tumor tissue by means of ionizing radiation is among the key methods to counteract this disease. About every second cancer patient in Germany is treated with radiotherapy, either alone or in combination with other therapy modalities like surgery or chemotherapy. Most commonly, high energy photons produced by electron linear accelerators are used for irradiation of the tumor, but also proton or heavy ion (typically $^{12}$C) radiotherapy is growing in popularity [1]. Proton and $^{12}$C ion therapy are technically complex and expensive compared to the standard photon therapy methods as they require large accelerators with high power consumption and operating expenses. However, due to the physical and radiobiological properties of heavy charged particles, the treatment outcome can potentially be improved and healthy tissue toxicity can be reduced [2, 3].

One emerging innovation in the field of particle radiotherapy is the reintroduction of $^{4}$He ion therapy which is currently under preparation at the Heidelberger Ionenstrahl-Therapiezentrum (HIT) [4, 5]. Up to now, $^{4}$He ions have only been used for radiotherapy in a clinical trial at the Lawrence Berkeley National Laboratory which ended in 1993 [6, 7]. Afterwards, the particle therapy community focused entirely on protons and $^{12}$C ions. By reestablishing $^{4}$He ions to the treatment spectrum the flexibility in therapy will be increased, as they have properties intermediate between protons and $^{12}$C.

In radiotherapy, a thorough understanding of the interactions of the particles used for irradiation with the atoms and nuclei in the tissue is essential for planning and validation of the dose delivery. If the underlying radiation physics is understood and modeled with good precision, the models for the different interaction types can be combined in a single radiation transport code (e.g. Monte Carlo codes like Geant4 [8] or FLUKA [9, 10, 11]) to calculate the dose distribution inside a reference medium, typically water, or directly inside the patient. On one hand, the electromagnetic interaction of heavy charged particles is modeled with remarkable precision in modern transport codes - proton and ion ranges are predicted correctly with sub-millimeter accuracy over the entire energy range used for radiotherapy. On the other hand, the more complex nuclear interactions are far less well modeled but have a large influence on the dose distributions [12, 13]. In most radiation transport codes, nuclear reactions are described by semi-empirical models and parametrizations, which are validated and optimized against measured cross sections. For projectile-target combinations and energies where no experimental data are available, the models are interpolated and scaled in a proper way to estimate the respective cross sections. However, for systems of special interest where the radiation transport calculation must be as precise as possible, validation of the nuclear models against experimental data is usually inevitably.

During the preparation work for $^{4}$He ion therapy at HIT, it was found that common transport codes used in the field of ion beam therapy, among them the GSI treatment planning system TRiP98 and the FLUKA Monte Carlo code, could not accurately reproduce measured dose distributions due to inaccurate nuclear reaction models. This finding has motivated a series of experiments, carried out at HIT within the scope of this thesis,

where projectile fragmentation cross sections for $^4$He ions on different materials of interest for radiotherapy (H, C, O, Si) were obtained. On basis of these new experimental data, the Tripathi parametrization of the nuclear reaction cross section $\sigma_R$ (implemented in TRiP98, and also found in Monte Carlo codes like Geant4) was optimized and the FLUKA nuclear reaction model was adjusted. This nuclear reaction model optimization eliminated the remaining dose calculation inaccuracies for $^4$He ions. Therefore, the work presented in this thesis will allow $^4$He dose calculations with the clinically desired accuracy.

Additionally, the impact of these nuclear model adjustments on the relative biological effectiveness of $^4$He ions was studied through calculations based on the local effect model.

Though nuclear fragmentation reactions degrade and blur the dose distributions of heavy ions, the produced fragments can also be exploited for in-vivo treatment verification [14]. An online treatment verification method could potentially mitigate the issue of particle range uncertainties which are a critical problem for radiotherapy with protons and heavy ions. One proposed in-vivo range verification method is the imaging of the spatial distribution of $\beta^+$-activity induced in the irradiated tissue using a positron emission tomography (PET) camera [15, 16]. This method is based on the knowledge of how the activation pattern is related to the dose distribution, which is deduced by recalculation of the treatment plan with a suitable radiation transport code. However, for the reaction channels which produce isotopes that can be measured by means of PET, mainly $^{10}$C, $^{11}$C and $^{15}$O, the nuclear reaction models in the common Monte Carlo transport codes still have large uncertainties [17]. This was the motivation for a series of experiments with protons and $^{12}$C ions carried out at the Marburger Ionenstrahl-Therapiezentrum which make up the second part of this thesis. Production cross sections for $^{10}$C and $^{11}$C on C and $^{15}$O on O were obtained by irradiating thin graphite and BeO targets and monitoring the decay of the induced $\beta^+$-activity. These data will also contribute to future improvements of Monte Carlo transport models.

In the following chapters, the two experimental setups used for the cross section measurement as well as the data analysis methods are described. The obtained cross section data are compared with reference data from the literature and with nuclear reaction models. The validity of these nuclear reaction models is demonstrated by comparing radiation transport calculations with measured data available in the literature. For $^4$He ions, those reference data are depth dose profiles in water while for protons, the model calculations are compared with profiles of induced $\beta^+$-activity in a tissue equivalent gel phantom measured with a PET camera.

# 2 Theoretical Background

This chapter summarizes the theoretical background of the research presented in this thesis.

## 2.1 Radiotherapy with Protons and Heavy Ions

In conventional radiotherapy the patient is irradiated with high-energy photons, typically produced as bremsstrahlung by electron linear accelerators with electron energies between 6 and 18 MeV. To spare the healthy tissue surrounding the tumor, the radiation field is shaped with collimators to match the tumor contours. By irradiating the patient from different angles with the beams intersecting in the target volume the dose to the tumor is increased while the dose to the critical organs is kept low. The evolution of photon therapy technology in the past decades, especially the introduction of inverse treatment planning and intensity modulated radiotherapy (IMRT) [18, 19, 20, 21] have resulted in substantial improvements of the radiotherapy treatment outcome and cancer survival in general. Millions of patients worldwide have been treated with modern photon radiotherapy.
However, there are still clinical cases where the dose conformity of modern photon therapy techniques is not sufficient, e.g. brain tumors near critical structures like the brainstem, or where the low dose bath of the normal tissue typical for IMRT treatments should be avoided, e.g. for pediatric patients. These cases have motivated the development of more sophisticated radiotherapy techniques, in particular the irradiation of the tumor with proton or heavy ion beams - known as ion beam therapy or particle therapy - which represents the spearhead of today's high-tech medicine. Proton or heavy ion beams (in this thesis all ions heavier than a proton are called heavy ions) can achieve a better dose conformity than high energy photons due to the underlying radiation physics and other additional advantages due to radiobiological effects [2].
Figure 2.1 shows the depth dose profile of 15 MV photons in water compared to the depth dose profiles of protons, $^{4}$He and $^{12}$C ions with ranges of $\sim$ 30 cm. The inverse depth dose curve of heavy charged particles with the so-called Bragg peak at the end of their range is the main rationale for their application in radiotherapy. This dose maximum can be shifted by changing the particle energy. Therefore a large fraction of the energy of a proton or heavy ion beam can be specifically transported and deposited into a tumor while the healthy tissue before and behind is spared. This is not possible with photon beams where the dose build-up is limited to the first few centimeters of the irradiated object. It can be observed that the depth dose profiles of protons, $^{4}$He and $^{12}$C ions look quite different, which is mainly a result of nuclear fragmentation reactions occurring along their penetration through the absorber. The fraction of the primary protons or ions that actually reach the Bragg peak depth without undergoing nuclear reactions decreases with increasing projectile mass which is the reason for the degradation of the Bragg peak height towards heavier ions. Furthermore the depth dose profiles of $^{4}$He and $^{12}$C ions have a characteristic tail behind the primary ion range due to the higher range of the lighter

projectile fragments. Because protons do not fragment but only generate heavy target fragments and secondary protons with low energy, there is no dose behind the proton Bragg peak. The degradation of the depth dose maximum due to nuclear fragmentation is mostly compensated for the heavy ions by radiobiological effects (as described in more detail in Section 2.4).

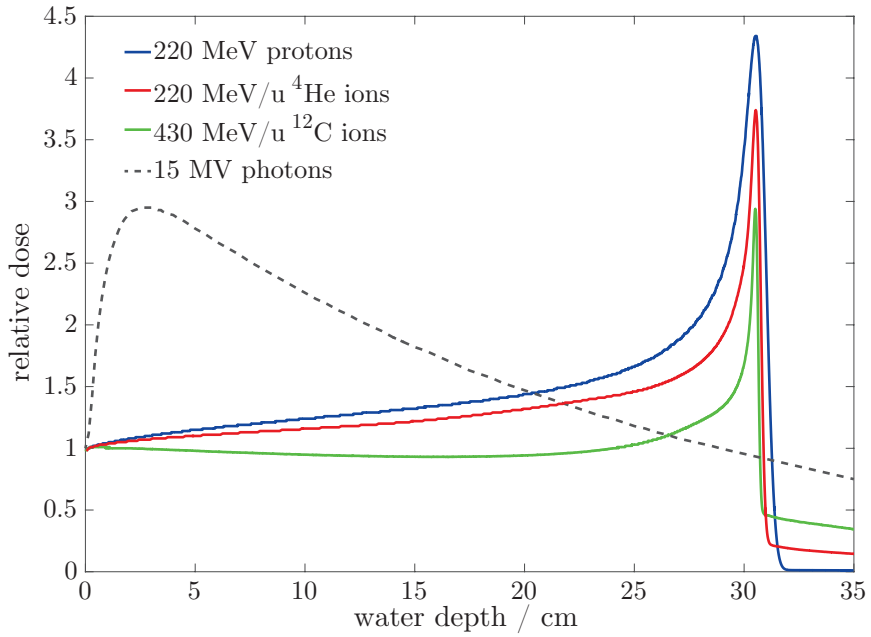


**Figure 2.1:** Depth dose profiles in water generated by high-energy photons, protons, $^4$He and $^{12}$C ions obtained by Monte Carlo simulations. The photon simulation was performed with the EGSnrc code [22] and for the heavy charged particle simulations the FLUKA code (version 2011.2x.2 for protons and $^{12}$C and the development version 2018.2 for $^4$He) was used. Only absorbed dose without any radiobiological weighting is shown.

When looking at the physical depth dose profiles only, heavy ions appear not to be superior to protons especially because of their fragmentation tail. The real advantage of heavy ions is based on their lateral dose profile rather than in their depth dose profile as well as on their increased biological effectiveness in the target area. With a view at the lateral profiles of protons, $^4$He and $^{12}$C ions in Figure 2.2 the advantages of heavy ion beams over proton beams for the irradiation of deep-seated tumors close to critical organs get clear. The protons are strongly scattered with increasing depth while the lateral profiles of $^4$He and $^{12}$C have a sharp fall-off even at 30 cm water depth. The reason for the reduced lateral scattering of heavy ions is their higher mass and thus higher forward momentum compared with protons. Beyond the lateral fall-off all heavy charged particle dose profiles show long extensions, the so called dose halo [23]. This halo consists of dose components originating from large-angle elastically scattered primary particles and doses from secondary fragments produced in inelastic nuclear reactions. The 15 MV photons generally produce much higher out-of-field doses than the heavy charged particles because the secondary electrons released by the Compton scattered photons can have ranges of

several centimeters and easily scatter out of the collimated field. Remarkably, the shape of the central field in the photon lateral profiles does not change considerably from 10 cm to 30 cm water depth which is in contrast to the heavy charged particles where the profiles are inevitably widened with increasing depth by the multiple Coulomb scattering.

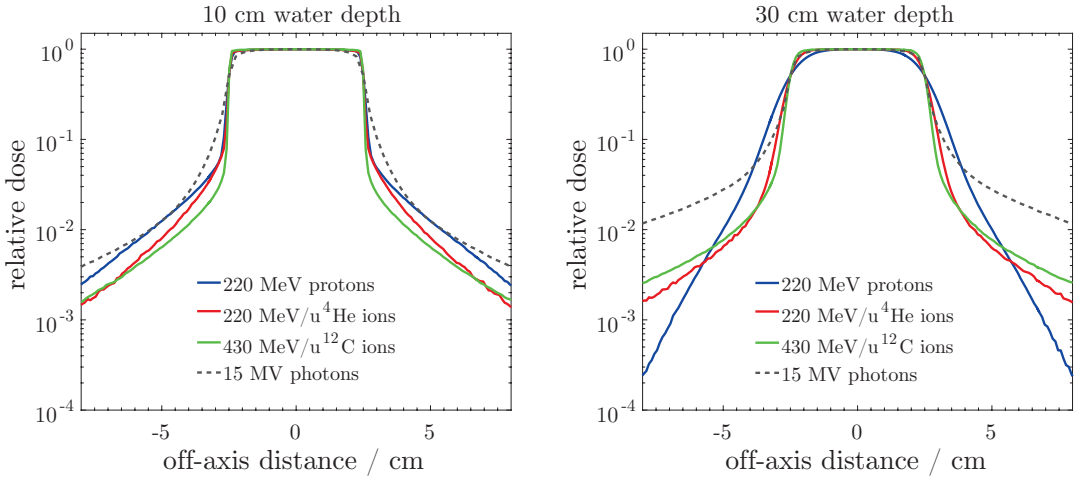


**Figure 2.2:** Lateral dose profiles in water generated by a $5 \times 5$ cm$^2$ square field of high-energy photons, protons, $^4$He and $^{12}$C ions obtained by Monte Carlo simulations. The photon simulation was performed with the EGSnrc code and for the heavy charged particle simulations the FLUKA code (version 2011.2x.2 for protons and $^{12}$C and the development version 2018.2 for $^4$He) was used. A perfect beam application and collimation as well as parallel beams were assumed in the simulations and only absorbed dose without any radiobiological weighting is shown.

The comparison of the dose profiles above shows that the physical characteristics of different radiation types differ strongly. There are a lot of factors (possible beam directions, location of the tumor, location of the organs at risk, size of the patient, etc.) that have to be considered in order to optimally exploit the interaction properties of different radiation types to achieve the desired treatment outcome. The situation gets even more complicated if radiobiological effects are taken into account [24]. In the end there is not a unique choice for the best radiation type to be used for radiotherapy.

## 2.2 History of Proton and Heavy Ion Therapy

The development of proton and heavy ion therapy was marked by several scientific, technological and methodological milestones which are summarized in this chapter. The idea of exploiting the depth dose characteristics of proton and heavy ion beams for radiotherapy came originally from Wilson in 1946 when he performed shielding measurements at cyclotrons [25]. Not even one decade later in 1954, the first patient was irradiated with protons at the Berkeley Radiation Laboratory in California (today known as Lawrence Berkeley National Laboratory). 72 patients were treated from 1957 to 1976 with protons at the Svedberg Laboratory in Uppsala, Sweden. In 1961 the Harvard university started with proton treatments and became the main center for proton therapy promotion. For the next decades proton therapy was a pure experimental technique and only available for

very small patient numbers at research facilities using the accelerators that were originally built for nuclear physics experiments. In the 1970s the invention of computer tomography (CT) and the availability of the first commercial CT scanners opened up new possibilities for proton therapy and for radiotherapy in general. This novel imaging technology allowed for the first time an individual 3D treatment planning and dose calculation. In 1977, 23 years after the first proton patient was treated in Berkeley, also the worldwide first heavy ion therapy project was set up there using beams from the Bevalac accelerator [26]. Like in all proton trials before, the beam application in the US heavy ion therapy project was fully passive: only few fixed energies were available and the dose distributions were shaped using scatter foils, absorbers and collimators [27]. 2054 patients were treated with $^{4}$He ions in the Berkeley trial and further 433 patients were irradiated with heavier ions, mostly with $^{20}$Ne but also some with $^{28}$Si and $^{40}$Ar [28, 29]. The shutdown of the Bevalac in 1993 marked the end of heavy ion therapy in the USA. However, the technical developments and experiences that have been gained in the US heavy ion trials were transferred to Japan where a dedicated heavy ion treatment and research center was built at the National Institute for Radiological Science (NIRS) in Chiba. Since its completion in 1994 many clinical $^{12}$C ion trials have been performed and heavy ion therapy has been continuously expanded in Japan in collaboration with industry partners like Hitachi and Mitsubishi [30]. The first dedicated hospital-based proton therapy center was built in Loma Linda in California and started the treatment of patients in 1990. Today the USA are the country with by far the most proton centers in the world but with no operational heavy ion center.

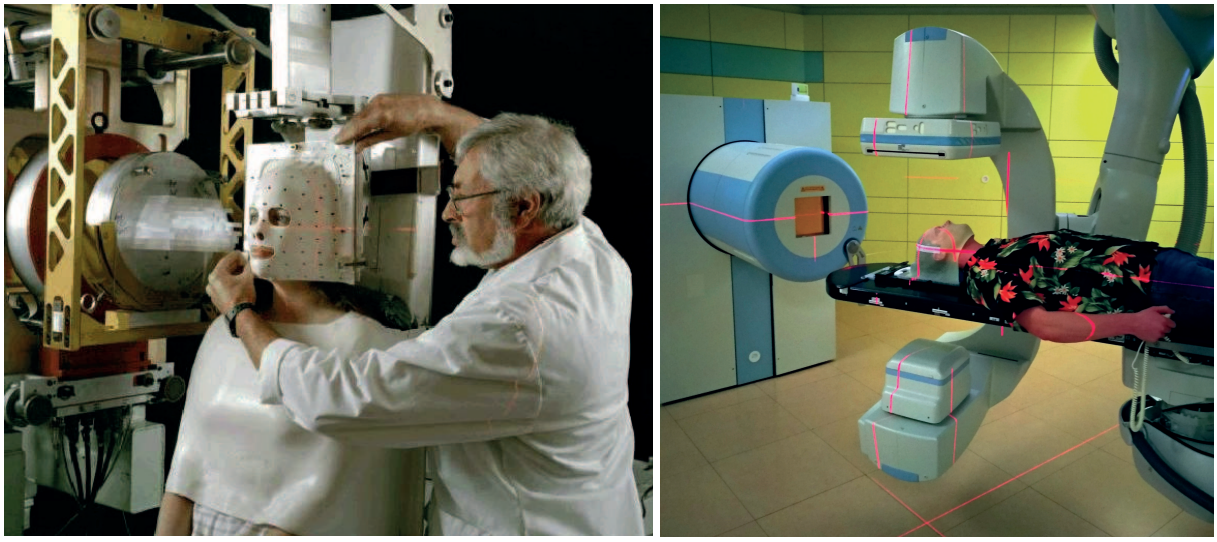

**Figure 2.3:** Heavy ion treatment at the Lawrence Berkeley Laboratory (left) and at the Marburger Ionenstrahl-Therapiezentrum (right). In the historical Berkeley setup the patients were treated in sitting position while nowadays the lying position on a treatment couch is preferred. In the past the dose distributions were passively shaped by range compensators in front of the patient while today beam scanning with active energy switching is the standard technique. Modern treatment rooms are also equipped with imaging devices to support the positioning of the patient like the x-ray system on a robotic arm shown on the right.

One particular technical innovation in the middle of the 1990s had a decisive impact on proton and heavy ion therapy in their present form: beam scanning [31]. Simultaneous developments of this technique took place at the Paul Scherrer Institute (PSI) in Switzerland for protons [32] and at the Gesellschaft für Schwerionenforschung (GSI) in Germany for $^{12}$C ions [33]. Instead of the passive broadening of the beam with scatter foils and collimators as it was practice until then, the new technique employs a sharp pencil beam that is scanned over the irradiation volume using adjustable magnetic deflection. This improves significantly the conformity of the dose distributions and reduces the secondary neutron dose to the patients as compared with the passive techniques [34]. At PSI 1D proton spot scanning (spot-by-spot scanning using a magnet in horizontal direction and moving the treatment couch in the vertical direction) was developed and first used for treating a patient in 1996. One year later, in 1997, the first patient was treated with a scanned $^{12}$C ion beam at GSI. The major innovations in the GSI pilot project were the fully active beam application (magnetic scanning in vertical and horizontal direction as well as active variation of the beam energy by the synchrotron, called *raster scanning*), novel treatment planning methods combined with improved radiobiological models [35, 36] and the introduction of in-vivo treatment monitoring using positron emission tomography [15, 16]. Today, beam scanning is the state-of-the-art dose application technique and every newly built commercial particle therapy system is equipped with a magnetic scanner. The success of the GSI $^{12}$C ion pilot project - 440 patients were treated between 1997 and 2008 with good clinical results - led to the planning and construction of the Heidelberger Ionenstrahl-Therapiezentrum (HIT) by the University Hospital Heidelberg in collaboration with GSI and Siemens [5]. Since 2009 a few hundred patients per year have been treated at HIT with protons and $^{12}$C ions. For research purposes the accelerator was also designed for $^{4}$He and $^{16}$O ions. Meanwhile $^{4}$He ions are used for pre-clinical studies and should soon be added to the treatment spectrum of the center (see Section 2.6).
The GSI technology and know-how was transferred to Siemens and they have built three combined proton-carbon synchrotron facilities: one in Marburg, another in Kiel and a third in Shanghai. The facility in Kiel was dismantled again before it was put into operation due to issues with the business plan. The same threatened to happen also with the facility in Marburg, but could be prevented by establishment of a joint venture with HIT. Since 2015 the center is treating patients under the name Marburger Ionenstrahl-Therapiezentrum (MIT). A major problem for proton and heavy ion therapy centers is that only a small fraction of the overall radiotherapy patients are suitable for particle therapy (at current status in the order of 10%). Therefore such a facility must either be small (e.g. single room proton therapy systems), be located in a metropolitan region or have a large patient acquisition area to work at full capacity.
The two other combined proton-$^{12}$C facilities in Europe are the Centro Nazionale di Adroterapia Oncologica (CNAO) in Italy and MedAustron in Austria. They are only partly based on the GSI technology but use a synchrotron design developed at CERN in the Proton-Ion Medical Machine Study (PIMMS) [37]. While all existing medical heavy ion accelerators are synchrotrons which can vary the energy actively most of the centers that use solely protons are equipped with a fixed-energy cyclotron and the energy is varied passively in a degrader-based energy selection system. Commercial proton therapy systems are available from companies like IBA or Varian.
There are currently many research topics of interest: One is the radiobiology of proton beams. While in clinical practice a fixed RBE of 1.1 is used there is strong evidence of an

increasing RBE towards the end of the range [38] which is suspected to cause unwanted side effects in some patients [39]. Another is the question if it would be beneficial to use also other ions instead of protons and $^{12}$C (like $^{4}$He or $^{16}$O) for treatment [24] or if they could even be combined in a multi-ion treatment [40]. Along with the high precision of particle therapy comes also a high sensitivity of the dose distributions against several different factors like anatomical changes, imaging artifacts or inaccuracies in the conversion from HU values to stopping power [41] and the particle range uncertainties resulting from these influences are among the major critical problems in modern particle therapy. Therefore, a reliable method to verify the range predicted by the treatment planning system, either directly during the treatment (online) or between two fractions (offline), would be highly beneficial to better exploit the full potential of particle therapy. Also the problem how to treat moving organs (e.g. lung tumors) with proton or ion beams is a current research topic [42]. An effective motion mitigation technique would increase the number of patients that can be treated with particle therapy and therefore contribute to a better utilization of the treatment center capacities. This already points out that besides technical challenges it is also important to consider economical and management aspects. There are several clinical studies ongoing to investigate which tumor entities actually benefit from particle therapy compared to conventional photon therapy [43]. The results of these studies, in the case they are positive for the heavy charged particles, will have the potential to increase the patient numbers and simplify the reimbursement or covering of the treatment costs by the health insurance companies. The facilities required for proton or heavy ion therapy are very large, expensive to build and complex to operate - therefore these treatment modalities are only available in specialized centers. Technical solutions which would make the facilities smaller and less complex (e.g. new accelerator designs) could contribute to a wider dissemination of proton and heavy ion therapy.
Today 88 particle therapy centers are in operation and they are spread over 20 different countries. Most of them are proton therapy centers, but 13 of them also treat patients with $^{12}$C ions. Per end of 2018, 220 000 patients have been treated with protons (190 000) and heavy ions (30 000) [44].

## 2.3 Interaction of Heavy Charged Particles with Matter

Protons and heavy ions are counted as heavy charged particles in contrast to the much lighter electrons and positrons. Heavy charged particles can interact in different ways with the material they penetrate through. The most important interactions and their significance for radiotherapy are briefly described in the following.

### 2.3.1 Electronic Energy Loss

When a heavy charged particle penetrates through matter it transfers energy to atomic electrons via the Coulomb interaction. The multiple electronic collisions that are undergone by the particle can in a good approximation be summarized to a continuous energy loss. The energy fraction $dE$ lost per unit path length $dx$ in a specific target material is given by the Bethe-Bloch formula [45, 46]

$$-\frac{dE}{dx} = 4\pi N_A r_e^2 m_e c^2 \rho \frac{Z_T}{A_T}\frac{Z_P^2}{\beta^2}\left[\frac{1}{2}ln\left(\frac{2m_e c^2\beta^2\gamma^2 T_{max}}{I^2}\right) - \beta^2 - \frac{\delta(\beta\gamma)}{2}\right] \tag{2.1}$$

where $N_A$ is the Avogadro constant, $r_e$ is the electron radius, $m_e$ is the electron mass, $c$ is the speed of light and $\beta$ and $\gamma$ have their usual meaning ($\beta = v/c$ and $\gamma = 1/\sqrt{1-\beta^2}$). $Z_T$ and $A_T$ are the atomic and mass number and $\rho$ is the density of the target material, $Z_P$ is the atomic number of the projectile, $T_{max}$ is the maximum energy transfer to an electron, $I$ is the mean ionization potential and $\delta(\beta\gamma)$ is the density effect correction which gets relevant at relativistic energies ($> 1$ GeV/u) [47]. The quantity $dE/dx$ is also called stopping power and is a material property for a given charged particle at a given energy. For heavy charged particles where radiative energy losses (e.g. bremsstrahlung) are negligible also the *linear energy transfer* (LET) is practically equal to $dE/dx$.

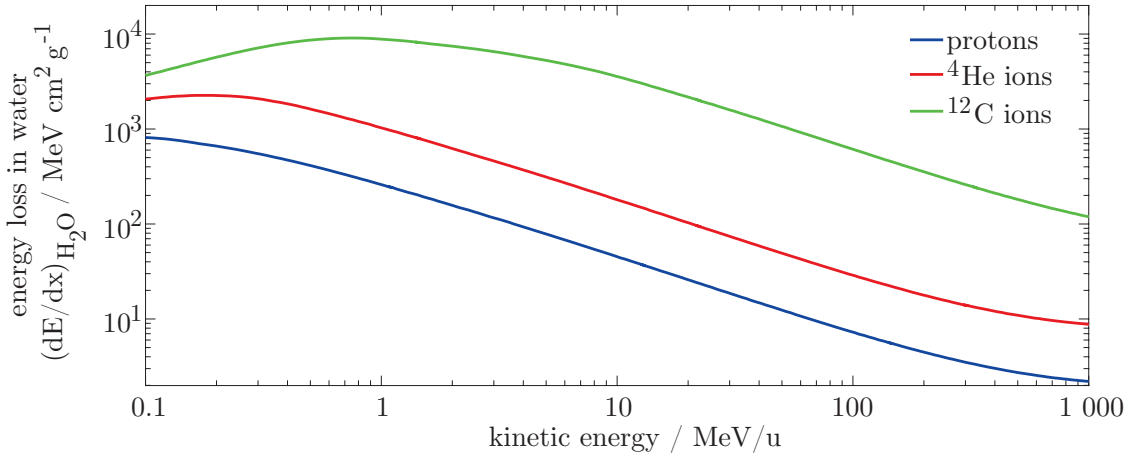


**Figure 2.4:** Energy loss of protons, $^4$He and $^{12}$C ions in water as a function of their kinetic energy. The tables were extracted from the FLUKA code.

Figure 2.4 shows the energy loss of protons, $^4$He and $^{12}$C ions as a function of their kinetic energy expressed in MeV/u because this so-called *specific energy* is proportional to the

velocity $\beta$ (unlike the total energy) [2]. The energy loss increases as the particle slows down due to the $1/\beta^2$ dependence of $dE/dx$ (see Equation 2.1). This is the reason for the Bragg peak at the end of the particle range. For $^4$He and $^{12}$C ions it can be seen that towards very low energies ($< 1$ MeV/u) the energy loss drops down again which is due to the decrease of the effective ion charge when they re-capture electrons into their atomic shells [48]. As also seen in Equation 2.1 the energy loss for different ions at the same velocity scales with $Z_P^2$. At very low energies (below $\sim 0.1$ MeV/u) also the nuclear stopping power which describes the energy transfer from the penetrating charged particle to recoiling atoms has to be taken into account [49]. However, for radiation transport calculations related to particle radiotherapy the nuclear stopping power is negligible since it affects only the last micrometers of the particle range.

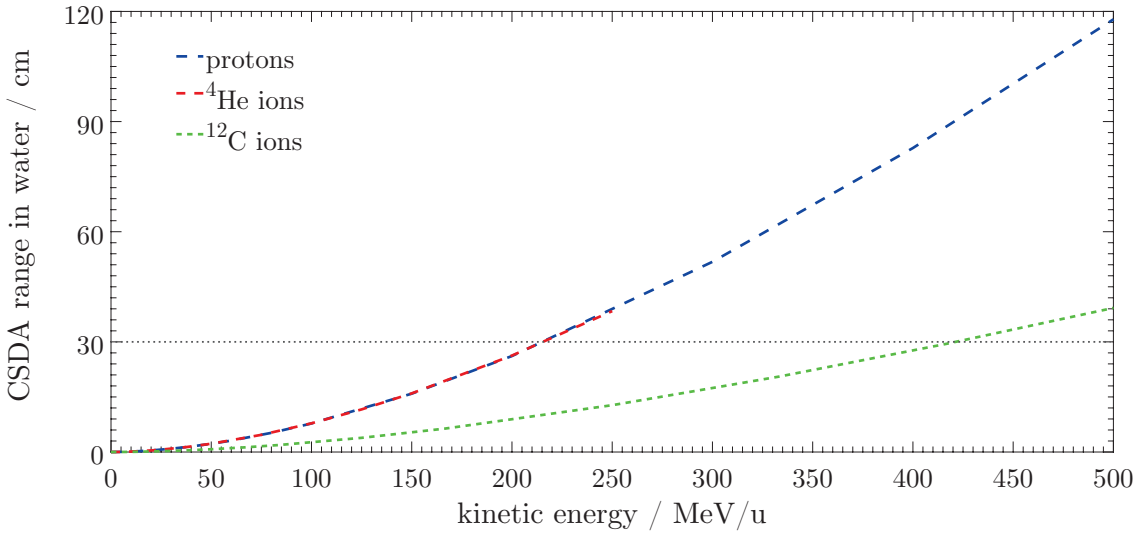


**Figure 2.5:** CSDA ranges of protons, $^4$He and $^{12}$C ions in water as a function of kinetic energy. The values were taken from the ICRU90 report [49]. The dotted line marks the energies that are required to penetrate 30 cm of water.

Figure 2.5 shows the ranges of protons, $^4$He and $^{12}$C ions in water as a function of kinetic energy under the continuous slowing down approximation (CSDA range). The range at the same velocity scales with $A/Z^2$, therefore the proton and $^4$He ion curves are overlapping while for $^{12}$C ions a higher acceleration is needed to reach the same depth. For particle ranges of 30 cm in water, protons and $^4$He ions need to be accelerated to an energy of 220 MeV/u while $^{12}$C ions need a higher specific energy of 430 MeV/u. These are the typical maximum energies therapy accelerators are designed for because with a range of 30 cm one can potentially reach every point in the human body with the Bragg peak.
If an ion changes its $A/Z^2$-ratio in a nuclear fragmentation reaction then this affects also its range. Therefore the fragment dose is deposited mostly before and behind the range of the primary ions where the Bragg peak is located (see Figure 2.1). These nuclear fragmentation reactions are the main phenomenon investigated within this thesis, therefore they are described in further detail in Section 2.3.3.
Equation 2.1 gives the mean energy loss of a heavy charged particle per unit path length, but actually the energy that is lost in a thin absorber shows statistical fluctuations around this mean value, the so-called energy loss straggling. These microscopic fluctuations add

up to a macroscopic range straggling and notably affect the shape of the resulting Bragg curve. The energy loss straggling has also an important influence on the peak widths and shapes in charged particle energy loss spectra measured with thin detectors, e.g. plastic scintillators.

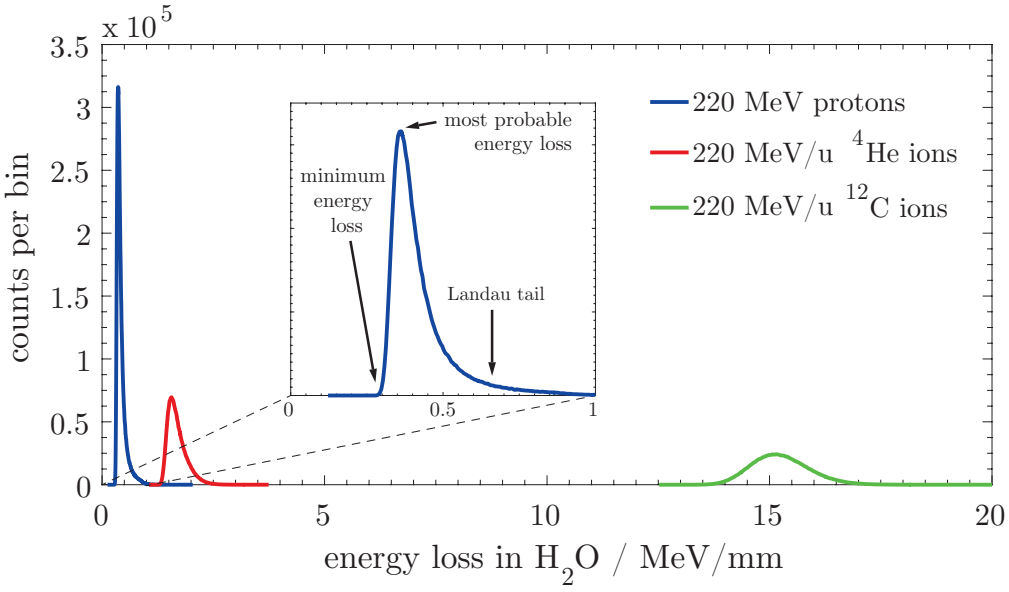


**Figure 2.6:** Energy loss distribution in a water slice of 1 mm thickness by 220 MeV/u protons, $^{4}$He and $^{12}$C ions simulated with the FLUKA Monte Carlo code ($10^6$ primary particle histories scored with 40 keV energy bins).

Figure 2.6 shows the energy loss distribution of protons, $^{4}$He and $^{12}$C ions at the same specific energy of 220 MeV/u in a 1 mm water slice. Such energy loss distributions have a characteristic asymmetric shape and can approximately be described with a Landau distribution [50]. Since in the example shown in Figure 2.6 the velocity of the different ions is the same, their mean energy loss scales with $Z^2$ according to Equation 2.1. The absolute peak width increases towards heavier projectiles while the relative energy loss straggling (peak width divided by mean energy loss) decreases. It can be seen that there is a minimum energy transfer, therefore every charged particle has a definite maximum range defined by the initial energy. While the energy loss fluctuates only very limited to the lower energy side, there is a long extension towards high energy transfers (the so-called *Landau tail*) which also reflects in the production of high-energy delta electrons that can travel up to millimeter distances away from their production point before stopping. The maximum kinetic energy $T_{max}$ that can be transferred to a delta electron according to the binary encounter model [51] can be estimated with Equation 2.2

$$T_{max} = 4\frac{m_e}{m_P}E_P \tag{2.2}$$

where $m_e$ is the electron mass, $m_P$ is the projectile mass and $E_P$ is the projectile kinetic energy. For 220 MeV/u protons and $^{4}$He ions this calculation yields 480 keV while 430 MeV/u $^{12}$C ions (corresponding to the same range of 30 cm in water, see Figure 2.5) can produce delta electrons with energies of up to 935 keV.

### 2.3.2 Elastic Scattering

The multiple collisions with atomic electrons undergone by a heavy charged particle as it traverses matter affect its direction only negligibly due to their large mass difference. However, there is also the possibility that a heavy charged particle gets scattered by the atomic nuclei of the target. Most of these elastic scatter processes happen by deflection of the projectile in the repulsive Coulomb field of target nuclei. The elastic scattering processes lead to a broadening of proton and heavy ion beams as they traverse matter. The effect of many single scatter events on a particle beam can be approximated well by multiple Coulomb scattering models [52, 53]. If the projectile moves very close to a target nucleus (as close as a few fm) it can also be elastically scattered by the short-range attracting nuclear force.

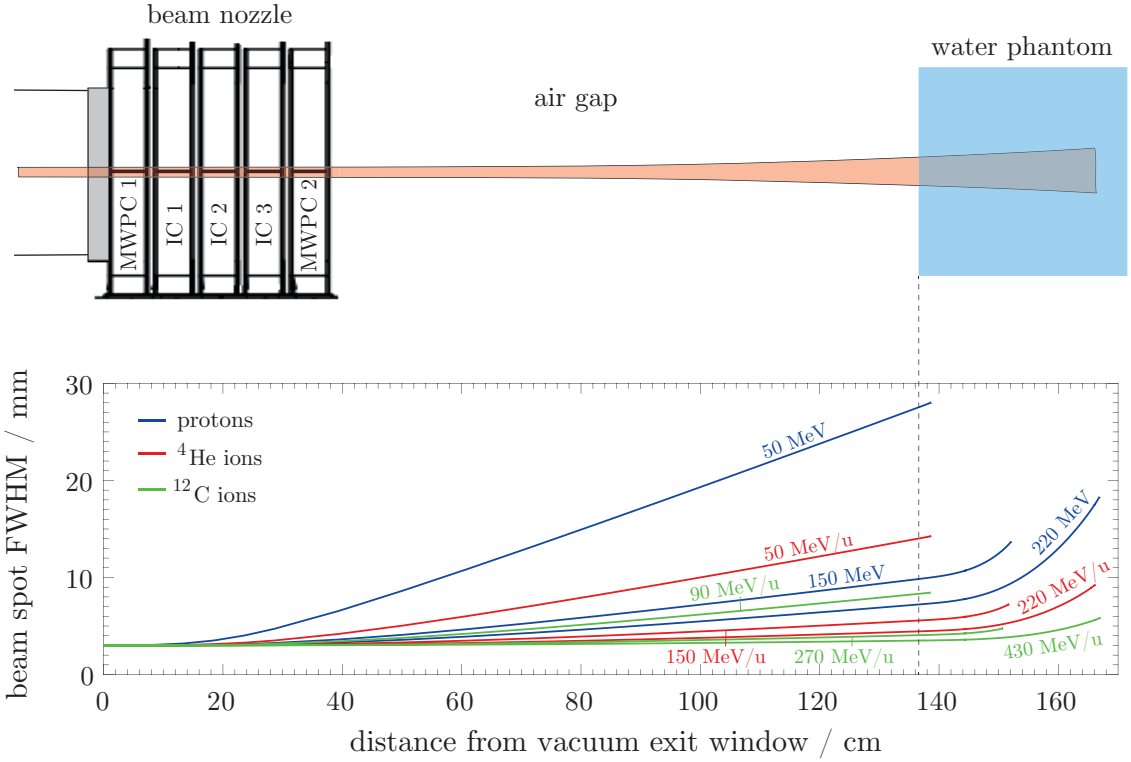


**Figure 2.7:** Broadening of proton, $^{4}$He and $^{12}$C pencil beams in a typical particle therapy setup due to elastic scattering calculated with the analytical SCATTMAN multiple Coulomb scatter and transport code [2]. The beam application is controlled by the beam nozzle detectors: a set of three ionization chambers (ICs) for the intensity and two multi wire proportional chambers (MWPCs) for the position. After an airgap of 1 m the beam hits the patient or in this example a water phantom. For the calculations the initial FWHM of all beams was set to 3 mm and no initial divergency was taken into account.

Figure 2.7 shows the full width at half maximum (FWHM) of proton, $^{4}$He and $^{12}$C pencil beams at three representative energies in a realistic therapy setup including the beam monitoring system upstream of the patient (mimicking the Siemens nozzle at HIT and MIT). The energies chosen correspond to the the maximum and minimum penetration depths of typical therapy accelerators as well as an intermediate energy. For $^{4}$He and

$^{12}$C ions the beam broadening due to lateral scattering is strongly reduced due to their higher mass and forward momentum compared with the lighter protons (compare also Figure 2.2). In this setup not only the beam spreading due to scattering in the patient tissue needs to be considered but also that due to scattering in the exit window, beam monitor ionization chambers and multi wire chambers upstream of the patient. These components which form the so-called beam nozzle typically have a total water-equivalent thickness of 2 mm. That seems small but due to the distance from nozzle to patient of typically 1 m even a small angular spread can translate into a significant enlargement of the beam spot at the patient surface. This scatter component is particularly important for proton pencil beams and for low beam energies. The beam spot sizes due to this effect can be reduced by shifting the patient closer to the nozzle [2].

### 2.3.3 Nuclear Fragmentation

If the projectile and target nuclei overlap during the collision and the kinetic energy exceeds the Coulomb barrier they can undergo inelastic nuclear reactions. Three examples of nuclear reactions as relevant for particle therapy are illustrated in Figure 2.8: For each of the three projectiles investigated in this work (protons, $^{4}$He and $^{12}$C ions) a reaction with a $^{12}$C target nucleus is shown.

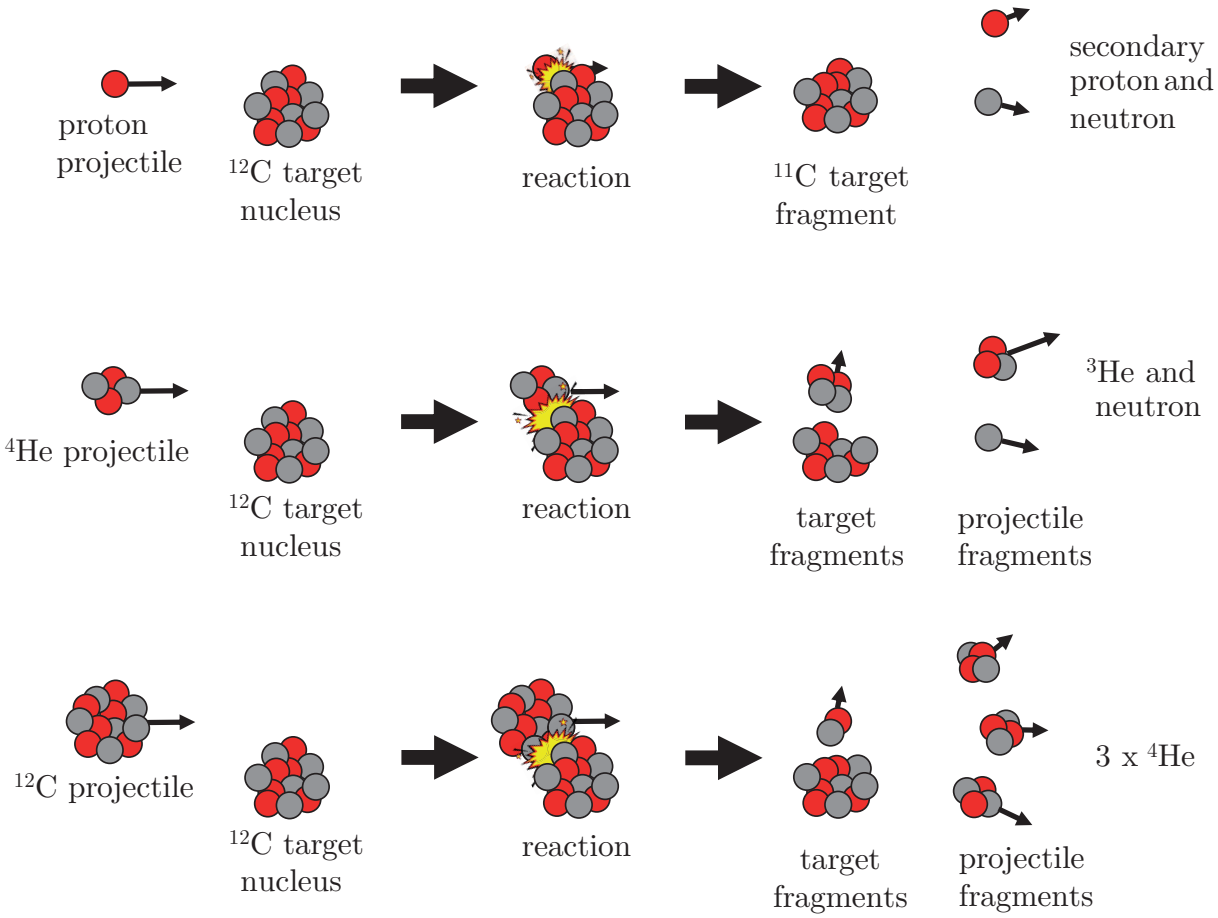


**Figure 2.8:** Illustration of selected nuclear fragmentation reaction channels by incident protons, $^{4}$He and $^{12}$C ions colliding with $^{12}$C target nuclei.

The first example shows a proton which knocks out a neutron of the $^{12}$C target nucleus. The proton gets deflected and loses some energy (the binding energy required to release the neutron plus its kinetic energy) and will consequently have a shorter range than the primary protons (after the reaction it is called a secondary proton). The other shown ejectile is a neutron and they usually have very long penetration lengths. For proton and also heavy ion therapy the secondary neutrons are important to take into account because they can cause out-of-field doses far from the target region and are the main concern concerning radiation protection and shielding of particle therapy facilities. The energy transfer to the $^{11}$C nucleus is low and therefore such heavy target fragments usually stop in the target close to their production point.
In nucleus-nucleus reactions like the two other examples not only the target nucleus but also the projectile nucleus can fragment. In a simplified model, the velocity of the target fragments is close to zero and the velocity of the projectile fragments is approximately equal that of the projectile ion. The range of the projectile fragments differs from the primary ion range according to the $A/Z^2$ scaling (see Section 2.3.1). A common model to describe nucleus-nucleus collisions is the abrasion-ablation model [54, 55]. In this model the nuclear reaction is considered as a two-step process where first the overlapping zone of projectile and target is abraded and forms a so-called fireball while the remaining pieces of the projectile and target nuclei have only a passive role and are called spectators. In the following ablation step, the spectators and the fireball de-excite by emission of nucleons which can also coalesce into light nuclei and by emission of prompt gamma photons. The abrasion-ablation model is well suited to describe collisions of heavy nuclei but comes to its limits for the light systems relevant for particle therapy. For $^4$He projectiles most of the peripheral collisions can actually be better described as direct reactions without the formation of an intermediate state [56]. In the $^4$He $+^{12}$ C example the $^4$He strips off a neutron and what remains is a $^3$He fragment. A special characteristic of $^4$He-induced reactions is that projectile fragmentation reactions only lead to combinations of a remarkably small number of fragment species, namely $^3$He, $^3$H, $^2$H, protons and neutrons. Also nucleon-pickup reactions lead only to unbound nuclei which immediately decay back into these species. The example reaction for the $^{12}$C $+^{12}$ C collision shows the fragmentation of the projectile into three $^4$He nuclei which has an increased probability due to the high stability of the $^4$He nucleus [2].
A reaction is considered inelastic if the sum of the kinetic energies in the final state is not equal to that in the initial state. Inelastic reactions in the energy range used for radiotherapy usually lead to fragmentation of the participating projectile and target nuclei. Nuclear reactions induced by $^4$He ions might be an exception of this: Due to the unique properties and extraordinary stability of the $^4$He nucleus (first excited state at $\sim$ 20 MeV, no bound excited state) a non-negligible contribution of inelastic scatter reactions, where the target nucleus fragments but the projectile stays intact, has been predicted [56].

#### 2.3.3.1 Activation

Most of the fragments produced in nuclear reactions are unstable. This causes that material gets activated after proton and heavy ion irradiation. Many of the radioactive nuclei produced are neutron-deficient isotopes like $^{11}$C and therefore $\beta^+$-emitters which can be exploited for in-vivo range verification (see Section 2.7). Light materials (like plastic or

biological tissue) typically decay within a few minutes or hours after irradiation because the half-lives of the produced nuclides are rather short. In heavy materials like brass, steel or lead also longer-lived nuclides are produced which can make it necessary that irradiated metal components (e.g. collimators) have to be permanently stored. Protons do not fragment themselves but only produce target fragments while in nucleus-nucleus reactions also the production of radioactive projectile fragments is possible. If these projectile fragments stop inside the irradiated target they also contribute to its activation.

#### 2.3.3.2 Influence on Dose Profiles

Nuclear fragmentation reactions have a strong influence on the dose profiles of protons and heavy ions (see Figure 2.1 and 2.2), especially for large penetration depths [2, 12, 57]. Therefore precise models to describe these reactions are an important requirement for radiation transport codes to be used for dose calculation. Figure 2.9 shows a spread out Bragg peak (SOBP) produced by $^4$He ions calculated with different nuclear reaction cross sections $\sigma_R$ (see Section 2.8.1). Such SOBPs can be generated by subsequent irradiation with different energies which is the common method in particle radiotherapy to cover the target volume with a homogeneous dose in depth.

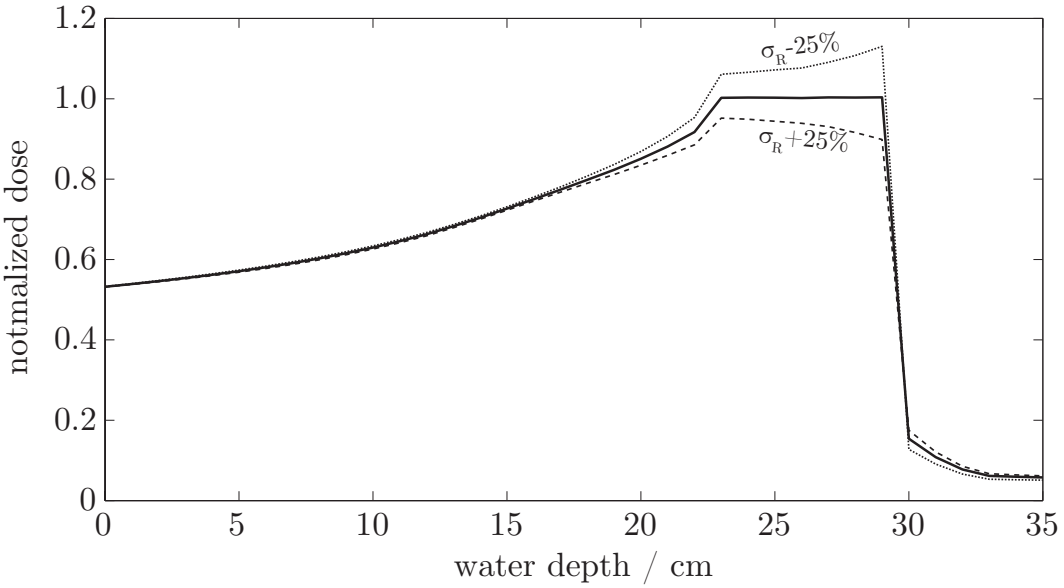


**Figure 2.9:** Influence of the nuclear reaction model on a $^4$He SOBP in water studied with a simplified transport model based on a 1D forward calculation.

With an increasing nuclear reaction cross section the SOBP dose decreases because more ions fragment before reaching the Bragg peak depth and consequently the dose in the fragment tail increases and vice versa. A flat SOBP that has been optimized with inaccurate nuclear models can actually appear with a gradient during the real irradiation [58]. The fragments have broader angular distributions than the primary ions as also shown in the illustrations in Figure 2.8. Therefore the fragments are a strong contributor to the dose halo visible in Figure 2.2.
Especially for protons, also the entrance channel of the depth dose profile is affected by

nuclear reactions. A proton itself cannot fragment but can generate secondary protons and target fragments [59, 60] which have shorter ranges than the primary particle. This causes a dose build-up in the first few centimeters of proton Bragg curves [61]. Similar build-up effects in the entrance channel have also been observed for high-energy $^{4}$He ion beams [62].

#### 2.3.3.3 Data Situation with Regard to Particle Therapy

While nuclear fragmentation of heavy projectiles like $^{16}$O [63] or $^{20}$Ne [64] had already been investigated during the Berkeley heavy ion therapy project there was still a lack of data for fragmentation of $^{12}$C ions in the beginning of the 1990s when the GSI therapy program was set up. Therefore the fragmentation of $^{12}$C ions has been extensively studied during the entire therapy project at GSI [65, 66, 67, 68] but also by other groups, e.g. in Japan [69, 70]. Now before the reintroduction of $^{4}$He ion therapy at HIT the community is facing the same lack of nuclear reaction data as for the $^{12}$C ions in the 1990s. Therefore different $^{4}$He fragmentation experiments [71, 72, 73] have recently been performed. However, there were still remaining dose calculation issues left and this was the major motivation to carry out the $^{4}$He experiments that are part of the work presented in this thesis (see also Section 2.6).
Another point where common nuclear models and Monte Carlo codes are known to have problems and experimental cross section data are lacking is the production of $\beta^{+}$-emitters [17, 74]. A PET camera can be used to locate the induced $\beta^{+}$-radioactivity produced along the beam path in the patient tissue for verification of the treatment (see Section 2.7). This technique requires an accurate radiation transport code to calculate the reference activity pattern which is then compared to the measured PET image. Several experiments focused on imaging of the induced activity in thick targets using a PET scanner to support nuclear reaction modeling [75, 76, 77, 78, 79], however, cross sections measured on thin targets are better suited for this purpose. Therefore in the other experiments performed within the scope of this thesis, production cross sections for the most common PET isotopes $^{10}$C, $^{11}$C and $^{15}$O by protons and $^{12}$C ions on C and O targets were measured.

## 2.4 Radiobiological Aspects

Ionizing radiation is able to damage biological systems very efficiently because it can destroy their DNA structures - directly via breakup of the DNA molecules by ionization or indirectly via the production of radicals in the cell nucleus which can then react with the DNA. The harmful effects of ionizing radiation were already observed shortly after the discovery of x-rays and radioactivity and it also got clear soon that the magnitude of the biological damage increases with the radiation dose. The introduction of standardized dosimetry in the 1930s revealed the fact that different radiation types induce different biological effects at the same absorbed dose level [80, 81]. It was postulated that the response of a biological system is not only determined by the absorbed dose but also by another characteristic property which was called *radiation quality*. Today it is known that the physical reason for that are the microscopic and nanoscopic ionization patterns which vary considerably among different radiation types. As a general trend, densely ionizing

radiation (high-LET radiation) is more effective than sparsely ionizing radiation (low-LET radiation) because a dense ionization pattern produces more lesions to the DNA helix. Furthermore the damages get more complex, e.g. clustered double-strand breaks, with increasing ionization density [82, 83, 84, 85].
Radiobiological studies are often carried out with isolated cells (in-vitro) instead of real organisms (in-vivo). A typical observable after irradiation of isolated cells with a known absorbed dose is how many of them are still able to reproduce and what fraction of the cells got inactivated. By doing that for different dose levels a *cell survival curve* as illustrated in Figure 2.10 for two different radiation types is obtained.

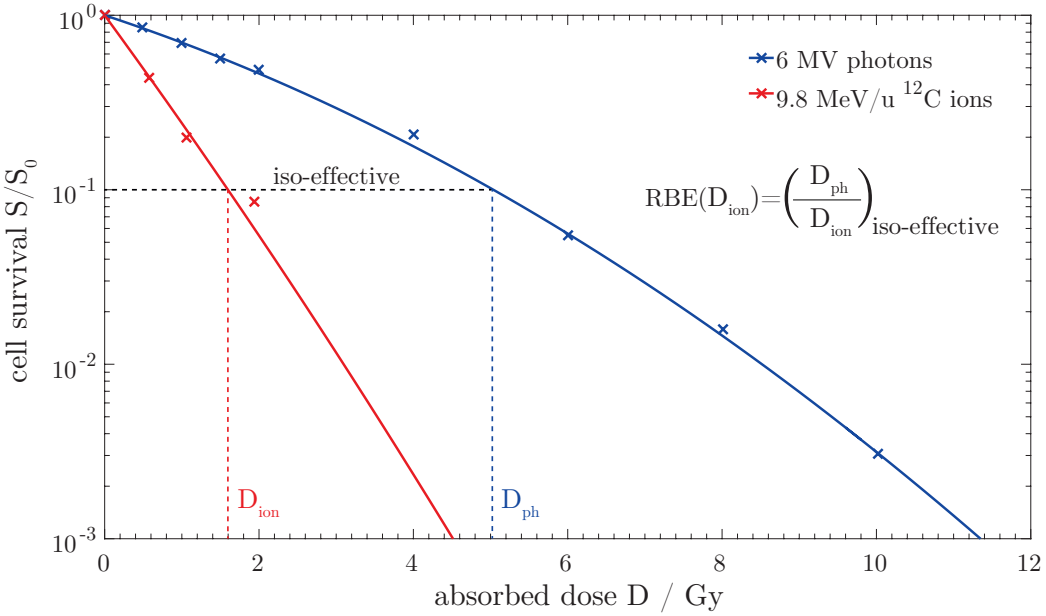


**Figure 2.10:** Cell survival curves for photons and $^{12}$C ions. The $^{12}$C data have been measured at the GSI UNILAC and for the reference irradiations 6 MV photons from a conventional radiotherapy linac have been used. The data were taken from Kamlah et al. [86]. The cells used in the experiments are A549 human lung adenocarcinoma cells.

Cell survival curves (relative survival $S/S_0$ as a function of absorbed dose $D$) can be described with a linear-quadratic function according to Equation 2.3

$$\frac{S}{S_0} = e^{-(\alpha D + \beta D^2)} \tag{2.3}$$

The linear-quadratic shape of the survival curves can be interpreted with the target theory: The linear term $\alpha$ corresponds to lethal DNA damages induced by single hits, e.g. the creation of a clustered double-strand break by one single particle. On the other hand, the quadratic term $\beta$ describes the probability of cell inactivation due to damages induced by multiple hits, e.g. two particle traversals each producing a double-strand break close to each other which sum up to an irreparable DNA damage. The $\alpha$ and $\beta$ values observed with low-LET radiation are characteristic parameters to describe qualitatively the radiobiological properties of a given tissue (i.e. the repair capacity).
The magnitude of the shoulder in the low-LET reference survival curve (measured e.g.

with high energy photons) is a measure of the repair capacity of a cell line: If low doses are well tolerated and a steep drop in cell survival is only obtained at high doses then the cell line can be considered radioresistant (small $\alpha/\beta$-ratio) while a sensitive cell line will show only a small shoulder (large $\alpha/\beta$-ratio). In high-LET heavy ion survival curves the shoulder is missing completely because even at low doses the DNA damages are too severe for the cell to repair due to the high local energy deposition along the particle tracks.
The ratio of the doses of a low-LET reference radiation and the radiation quality of interest (e.g. heavy ions) that produce the same biological effect is defined as the relative biological effectiveness (RBE). In radiotherapy, the absorbed dose is weighted by the RBE so that treatment plans for different radiotherapy techniques get comparable in form of *biologically equivalent doses* (see Figure 2.10). Besides the radiation quality the RBE depends also on many other factors like tissue type, dose level, dose rate and also on the biological endpoint being considered. The typical endpoint of interest for in-vitro experiments is cell inactivation (the cell cannot reproduce anymore) while clinical (in-vivo) endpoints of interest are for instance tumor control or normal tissue complication.
Heavy charged particles with high LET show an increased RBE which is due to the concentrated energy deposition along their tracks making the induction of irreparable DNA damages more probable than for low-LET radiation. However, as can be seen in the example of Figure 2.10 the actual RBE value of a given radiation quality depends also strongly on the dose. Due to the several factors which determine the RBE, a biophysical model which can predict RBE values accurately and fast for every voxel of a patient CT is required for the biological treatment plan optimization in heavy ion therapy.

### 2.4.1 Local Effect Model

For this purpose the local effect model (LEM) was developed during the GSI heavy ion pilot project. Its basic idea is that on a microscopic scale the same local doses produce equal biological effects, independent of the radiation type [87]. With this assumption, the microscopic energy deposition pattern of the radiation quality of interest can be used together with the response of a biological system to low-LET radiation (where the dose pattern is assumed to be homogeneous even on the microscopic level) to estimate the macroscopic biological effect and thus the RBE. Some important input parameters to the LEM are tissue-specific, in particular the $\alpha$ and $\beta$ values and the dose $D_{cut}$ where the survival curve changes from linear-quadratic to purely linear (at very high doses the linear-quadratic model underestimates the survival) as well as the cell nucleus size. Further an accurate ion track structure model which describes the microscopic dose distribution around the particle tracks as well as precise knowledge about the composition of the radiation field at every point in the patient are required. For the latter, energy spectra of all particle species (primary ions and all fragment species that can be produced) as a function of water depth have to be provided as an input for the RBE calculation. Their calculation requires a radiation transport code with realistic nuclear reaction models. The nuclear reaction cross sections obtained in the experiments presented in this work also have an impact on RBE calculation because they are used for optimization of such nuclear reaction models. Therefore basic nuclear physics experiments with therapy ions contribute not only to a better physical description of ion beams but also to a more precise understanding and modeling of their radiobiological effectiveness.
The LEM is used at all carbon ion therapy centers in Europe and China, however, still

in its first version LEM I. Meanwhile the initial model has been further developed and improved step-wise from LEM I up to the recent version LEM IV [88, 89, 90]. At the Japanese $^{12}$C ion therapy centers the RBE calculation is based on the microdosimetric kinetic model (MKM).

### 2.4.2 RBE Effects on Dose Profiles

When a patient is irradiated with a beam of heavy charged particles the RBE depends not only on the particle species but also on the depth and on the tissue type.

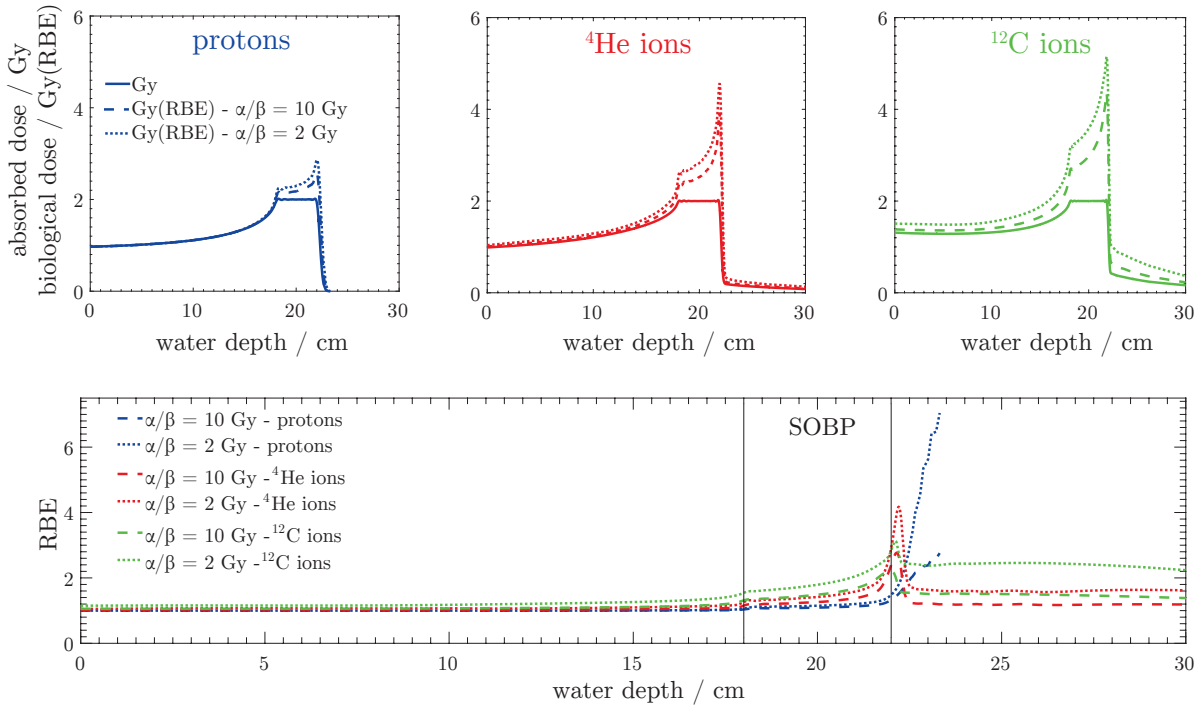


**Figure 2.11:** Examples of a SOBP produced by protons, $^{4}$He and $^{12}$C ions. Absorbed dose, biologically equivalent dose and RBE profiles were calculated with TRiP98 (calculation by D. Boscolo, GSI) for two different tissue models using LEM IV tables (also used in a study by Grün et al. [91]). The LEM IV input parameters were $\alpha = 0.1$ Gy$^{-1}$, $\beta = 0.05$ Gy$^{-2}$ and $D_{cut} = 8$ Gy for the normal tissue ($\alpha/\beta = 2$ Gy) and $\alpha = 0.5$ Gy$^{-1}$, $\beta = 0.05$ Gy$^{-2}$ and $D_{cut} = 14$ Gy for the tumor tissue ($\alpha/\beta = 10$ Gy).

The ionization density and consequently the RBE is higher in the Bragg peak region than in the entrance channel. Therefore, depending on the irradiated tissue and the dose level, the degradation of the heavy ion Bragg peaks due to nuclear fragmentation as visible in Figure 2.1 is compensated or even turned around by weighting the absorbed dose profiles with their corresponding RBE profiles.
Figure 2.11 shows a spread out Bragg peak (SOBP) produced by protons, $^{4}$He and $^{12}$C ions. In this example the SOBPs were optimized for a flat absorbed dose of 2 Gy with an extension of 4 cm centered at a water depth of 20 cm. The absorbed dose profiles are shown together with the RBE-weighted dose profiles and below also the corresponding RBE profiles are plotted. The optimization and calculation was done with TRiP98 using

LEM IV tables for two different tissues: One has an $\alpha/\beta$-ratio of 10 Gy and should represent typical tumor tissue. The other tissue has a lower $\alpha/\beta$-ratio of 2 Gy and should mimic normal tissue which is typically more radioresistant. In a real treatment scenario one would optimize for a flat biological dose in the SOBP instead of a flat absorbed dose. However, in the present example only the dependence of the RBE on the depth, tissue type and particle species should be compared and therefore the same treatment plan had to be used for the different tissues.
The RBE peak for $^{12}$C ions lies almost at the same depth as the absorbed dose peak which leads to an optimal amplification of the high physical dose through a high biological effectiveness [92, 93]. This interplay of radiation physics and biology makes $^{12}$C a radiobiological optimum which was the main reason why $^{12}$C ions were selected for the heavy ion project at GSI and are the standard heavy ion used for radiotherapy today. For ions lighter than $^{12}$C the RBE maximum is located behind the dose maximum and for heavier ions (like $^{16}$O or $^{20}$Ne) it is located before. However, $^{12}$C ions show RBE effects not only in the target region but at all depths and their magnitude strongly depends on the radioresistance of the tissue. This can introduce uncertainties in the normal tissue reaction and in the tumor response if the basic input data for the RBE calculation ($\alpha$, $\beta$, $D_{cut}$) are not well known.
Protons show only weak RBE effects (values close to 1) until the end of their range where their ionization pattern gets dense enough to cause complex DNA damages. Remarkably, in the single-field irradiation example shown in Figure 2.11 the protons show the highest RBE maximum of the three ion species, but because this maximum lies behind the SOBP region it does not translate into a high biological dose. In clinical practice the proton RBE is considered to have a fixed value of 1.1 independent of the depth or dose level which has mainly historical reasons. It is widely discussed in the proton therapy community if this assumption is still reasonable [94]. In principle, modern radiobiological models like LEM IV are considered to be suitable for biological treatment planning not only for heavy ions but also in proton therapy [95].
The normal tissue radiobiology of $^{4}$He ions is comparable to protons because they show only moderate RBE effects in the non-target region (entrance channel and fragment tail) while in the tumor region their biological effectiveness is strongly increased like for $^{12}$C ions. These properties together with their lateral scattering which is more similar to the heavier $^{12}$C ions (see Figure 2.2 and 2.7) make them a good compromise between protons and $^{12}$C ions for clinical cases where RBE effects in the normal tissue regions should be avoided but a sharp lateral fall-off at large depths is required (see also Section 2.6).

## 2.5 Dose Calculation Methods

In modern radiotherapy, the 3D dose calculation and treatment planning is performed on a CT image of the patient where a radiooncologist has contoured the target volume which should be irradiated with the prescribed dose and the organs at risk that should be spared. To perform a proton or heavy ion dose calculation on such a treatment planning CT, the HU-values (which represent x-ray attenuation) need to be converted, either into material composition or directly into stopping power ratios by applying a CT-scanner-specific look-up table. Because a HU value does not have a unique relation to a certain stopping power this conversion can lead to uncertainties in the particle ranges predicted

by the treatment planning system [41]. These uncertainties can potentially be reduced by using a dual energy CT [96] but single energy CT is still the standard technique used in most particle therapy centers.
In modern radiotherapy with photons but also proton and heavy ion therapy, an inverse treatment planning is performed: A medical physicist specifies dose levels and limits as well as some other parameters like number of fields or beam angles and an algorithm optimizes the pencil beam scanning patterns (deflection in lateral direction and energy variation to cover the target volume in depth) to obtain a dose distribution which matches the specifications. The dose is re-calculated multiple times during the iterative optimization process, therefore the speed of the dose calculation algorithm determines how long it takes to obtain a treatment plan. There are different dose calculation methods with different precision levels but also different speeds available. In the clinical routine the treatment planning is mostly based on pencil beam algorithms because they are very fast. As a support for the routine treatment planning also the use of Monte Carlo codes is becoming more and more popular because they provide a very accurate dose calculation, even close to density inhomogeneities where pencil beam algorithms get imprecise. However, a major limitation for Monte Carlo algorithms are their long computation times which can only be reduced by parallel computing, e.g. on a CPU cluster, or by simplification of the radiation transport models, potentially at the cost of accuracy.

### 2.5.1 Pencil Beam Algorithms

Most commercial treatment planning systems available for protons and heavy ions use pencil beam algorithms for dose calculation because only a fast method can be used for optimization of a treatment plan in reasonable time. The concept which is described in the following was one of the developments made for the GSI $^{12}$C therapy project which had some special requirements on the treatment planning system due to the novel scanned beam application which were not fulfilled by any commercial product at that time. It was implemented in the treatment planning system TRiP98 [35, 36] and later translated into the commercial product syngo RT by Siemens.
A pencil beam algorithm makes use of physical basic data for pencil beams of the ion species used, preferably for all energies that are available from the accelerator. A typical basic dataset includes laterally integrated depth dose distributions, the lateral dose profiles as a function of depth in parametrized form (single Gaussian in older algorithms, double Gaussian in newer ones) as well as primary particle and fragment spectra at different depths for RBE calculation. All of these basic data are calculated in advance using a detailed radiation transport code - either by a full Monte Carlo simulation (e.g. FLUKA as used at HIT [97]) or by a deterministic 1D forward calculation (e.g. the YIELD module in TRiP98 as used in the GSI pilot project [35]). Because the radiation transport is calculated in water ($H_2O$), the reference medium in radiotherapy, the code must have accurate nuclear reaction models for H and O targets implemented. The basic dataset is stored in the form of look-up tables from which the pencil beam algorithm can read them. The voxel information from the treatment planning CT image which has been converted from HU values into stopping power ratios relative to water is used to calculate the water equivalent path lengths in beam direction for all irradiation angles. The depth dose profiles are then put along those lines and the lateral profiles are applied according to the parametrization in the basic data as described by Equation 2.4

$$D(\vec{r}) = ddd(z) \cdot D_{lat,z}(\sqrt{x^2 + y^2}) \tag{2.4}$$

where $ddd(z)$ is the depth dose distribution and $D_{lat,z}(\sqrt{x^2 + y^2})$ is the lateral dose distribution parametrized in depth.
The biologically equivalent dose $D_{biol}$ at a certain point $\vec{r}$ within the patient can be calculated according to Equation 2.5 [67]

$$D_{biol}(\vec{r}) = \sum_{Z=1}^{Z_P} \int_0^{E_{max}} \Phi(Z, E, \vec{r}) \cdot LET(Z, E) \cdot RBE(\Phi) \cdot \frac{1}{\rho(\vec{r})}\, dE \tag{2.5}$$

where $Z$ is the ion charge (all charges up to the primary projectile charge $Z_P$ have to be considered), $E$ is their kinetic energy, $\Phi$ is their fluence, LET is their energy loss and $\rho$ is the local density of the tissue. The fluence as a function of particle species, kinetic energy and water depth is stored in the physical data base, the LET as a function of $Z$ and $E$ can either be calculated using the Bethe-Bloch equation (Equation 2.1) or retrieved from pre-calculated energy loss tables and the local density is available from the CT image. The RBE is calculated online for each voxel from the primary ion and fragment spectra and a pre-calculated LEM table for the tissue of interest.
The biological dose distribution is optimized to fulfill the criteria that were specified by the medical physicist. Usually this includes a homogeneous coverage of the target volume at the dose level as prescribed by the radiooncologist while the dose to the critical organs should be kept under certain limits. The optimizer varies the particle number applied to each raster point until a satisfactory dose distribution is reached. If that is not possible under the given boundary conditions the medical physicist could e.g. add additional beam angles, relax the dose limits to the critical organs or switch to another ion species.
Some dose calculation uncertainties can occur with pencil beam algorithms if the beam penetrates through objects that are far from being water-equivalent, e.g. titanium implants or gold markers. Furthermore the lateral scattering at density inhomogeneities (e.g. in the lung) may be predicted inaccurately because a pencil beam algorithm simply scales the dose distribution in forward direction and does not account for in-scattering from lateral surrounding voxels [98]. Therefore partial beam or edge scatter effects can not be described appropriately by pencil beam algorithms.

### 2.5.2 Monte Carlo Radiation Transport Simulation

The most precise dose calculation method available is the Monte Carlo simulation technique [99]. Indeed, an exact analytical description of a radiation transport problem with a complex geometry as in radiotherapy is often not possible. Because of the stochastic nature of radiation interaction with matter such a problem can alternatively be simulated using random numbers and models that reflect the individual interaction probabilities e.g. in form of cross sections. The quantity of interest (dose, fluence, spectral fluence, number of interactions, ...) can then be scored during simulation of the radiation transport. The random numbers are generated arithmetically by pseudorandom number generators [100]. The series of the numbers from such a generator depends on the start value, the so-called

random seed, therefore the simulation is fully reproducible if the random seed is known. The results of Monte Carlo simulations are in general normalized per primary particle. Averaging over many primary particle histories then leads to an estimate of the quantity of interest. The average value converges against the *true* value when the number of histories goes towards infinite. The statistical uncertainty resulting from the finite number of histories can be estimated by calculating the standard deviation between the average values of individual runs.
If the underlying physics models and cross sections are well developed and benchmarked, a full Monte Carlo dose calculation typically agrees with measurements better than one percent [101, 102]. However as mentioned above, a Monte Carlo dose calculation can take very long, depending on the complexity of the problem and the desired statistical uncertainty [103]. This is still a restriction for the usability of Monte Carlo codes in clinical practice. However, as described above, it is common practice to calculate the physical basic data for treatment planning systems based on pencil beam algorithms in advance by Monte Carlo simulations and, if necessary, a treatment plan re-calculation can be performed to check the standard dose calculation. Typical Monte Carlo codes used for particle therapy applications are FLUKA [9, 10, 11], Geant4 [8] and PHITS [104].

## 2.6 Radiotherapy with Helium Ions

So far it has been common practice in particle radiooncology to avoid the use of $^{12}$C ions in the case of pediatric patients if possible [105]. Due to their high LET $^{12}$C ions show increased RBE values already in the entrance channel (see Figure 2.11) and it is speculated that this could also be associated with an increased late effect and secondary cancer risk even though to date there is no clinical evidence for that [105, 106, 107, 108]. Since pediatric patients are known to be more radio-sensitive than adults [34, 105, 109] and their remaining lifespan after the therapy can be up to many decades one should be especially cautious when there is a risk of late effects. In some pediatric cases where the tumor is located close to a sensitive organ the lateral dose fall-off that could be achieved with protons may not be sufficient (see Figure 2.2). For such cases it would be beneficial to use an ion where RBE effects in the healthy tissue are less pronounced than for $^{12}$C (see Figure 2.11) but which can spare the critical structures close to the tumor better than protons. Cell experiments and treatment planning studies have shown that $^{4}$He ions might be a good choice for such scenarios [4, 91, 110, 111, 112].
As mentioned in Section 2.2, $^{4}$He ions have already been used to treat 2054 patients in Berkeley until 1993 [6, 7] and now their clinical revival is being prepared at HIT in Heidelberg. During the preparation studies it turned out that the FLUKA Monte Carlo code (and also the YIELD module of TRiP98) could not accurately reproduce measured $^{4}$He Bragg curves, especially for large penetration depths. For monoenergetic beams the dose deviations were as large as 8% in the Bragg peak region for FLUKA [113] and even larger for TRiP98 [4]. Such disagreements would not be acceptable for a clinical use and since FLUKA is the standard transport code used at HIT [97] for calculation of the basic data for the clinical treatment planning system (see also Section 2.5.1) an optimization of its physics models was required. The dose calculation inaccuracies were suspected to be caused by inaccurate nuclear reaction models in the code but their improvement was not possible due to a lack of experimental data in the therapeutic energy range. This was

the main motivation for the $^4$He fragmentation experiments presented in this work.
If it turns out in the future HIT studies that $^4$He ion therapy is worth the technical effort then every existing synchrotron facility could in principle be upgraded by adding an extra $^4$He ion source like at HIT. It is a known challenge that during the acceleration of $^4$He ions the beam can get contaminated with ions of the same $Z/A$-ratio ($^{12}$C, $^{14}$N, $^{16}$O) due to their same magnetic rigidity. For that reason in the original planning of the HIT facility the use of $^3$He instead of $^4$He ions was foreseen [5], however, the issue could be solved by setting up a dedicated $^4$He source where it is ensured that the source gas is kept clean and today the accelerator provides $^4$He ion beams without notable contamination [79].
Another advantage is that $^4$He ions need to be accelerated only up to 220 MeV/u which makes the construction of cyclotrons easier than for $^{12}$C ions because relativistic effects are still moderate at this velocity [114]. The company IBA is developing a therapy cyclotron called C400 which is designed to accelerate protons, $^4$He and $^{12}$C ions to 400 MeV/u [115]. Like the proton therapy cyclotrons available on the market it will also be a fixed-energy machine and the energy has to be varied in a degrader, typically equipped with graphite wedges [116]. Besides the lateral scattering in the degrader, also the transmission reduction due to nuclear fragmentation reactions has to be taken into account. Therefore, the $^4$He $+^{12}$ C cross sections presented in this thesis might also be interesting for the degrader design in such kind of $^4$He therapy accelerators.

## 2.7 PET Range Verification

Nuclear fragmentation does not only bring disadvantages but can also be exploited for in-vivo range verification [14] because the primary protons or ions interact with the target nuclei along their path until they stop. A well-developed range-verification technique would be a valuable tool for particle radiotherapy to mitigate the range uncertainties, e.g. due to the CT to stopping power conversion (see Section 2.5). Different strategies have been proposed to detect the spatial distribution of nuclear reactions occuring in the patient body which provides the range information. One of these methods is particle therapy positron emission tomography (PT-PET), where the spatial distribution of positron emitting nuclear fragments (e.g. $^{10}$C, $^{11}$C or $^{15}$O) is measured using a PET camera, either in-beam [15, 75, 117], in-room [118] or offline [119, 120].
There is not a direct correlation between the $\beta^+$-activity distribution and the dose distribution since both result from different physical processes (nuclear and electromagnetic interaction). However, by comparing a PET image recorded during or after irradiation of the patient with the *expected* activity pattern, it is possible to evaluate how successful the beam application has been. Therefore, the common method is to calculate a reference $\beta^+$-activity pattern using a suitable radiation transport code and to compare it to the measured PET image. The treatment delivery can be considered range-error-free if the activity pattern obtained from the PET measurement matches the calculated one while large deviations can indicate problems. This can then be taken into account for the next therapy fraction (e.g. recording a new treatment planning CT). While positron emitting target fragments are produced by protons and heavy ions, $^{12}$C ions represent a special case because they have also distinct reaction channels for the production of positron emitting projectile fragments ($^{10}$C and $^{11}$C). As shown in Figure 2.12 the target fragments have

only low energies and stop practically at their production point and therefore generate a rather flat $\beta^+$ activity profile until close before the end of the particle range. For $^{12}$C projectiles this target fragment continuum is additionally overlaid by a $\beta^+$ activity peak close before the primary ion range. This peak originates from the projectile fragments which are produced at about the same velocity as the projectiles: Due to their slightly lower mass the fragments stop shortly before the primary ions - the $^{11}$C at $\sim 11/12$ and the $^{10}$C at $\sim 10/12$ of the primary $^{12}$C range (see Section 2.3.3). Effects on the measured activity profiles that have to be considered in addition are the biological washout of the generated isotopes, the resolution of the PET scanner and possible image reconstruction artifacts.

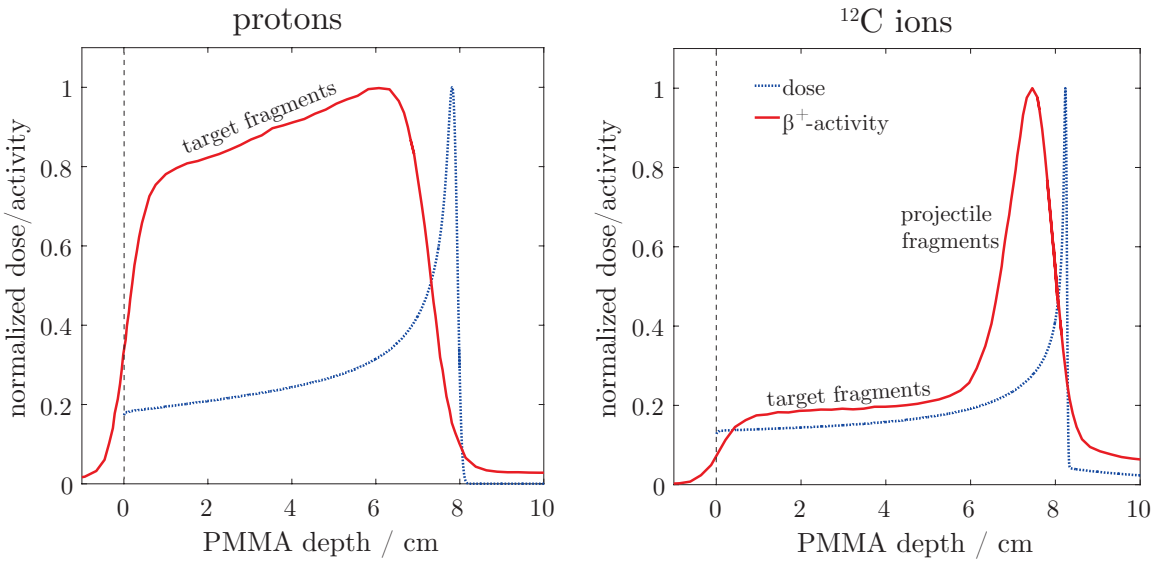


**Figure 2.12:** Profiles of the $\beta^+$-activity produced in a PMMA target by 110 MeV protons and 212 MeV/u $^{12}$C ions compared to the depth dose profiles. The activity profiles have been measured at the GSI in-beam PET scanner and were taken from [17] and the dose profiles were calculated with FLUKA. The broadening of the activity profiles is due to the limited PET resolution.

The sensitivity of the PT-PET method depends strongly on the accuracy of the nuclear reaction models within the radiation transport code used as reference [77, 121] because uncertainties in the prediction of the positron emitter yields may cause deviations between measurement and calculation even if the treatment is delivered without any range errors. Major errors in the treatment (e.g. irradiation through an empty frontal sinus instead of a filled one as described by Enghardt et al. [16]) could already be well detected with the PT-PET method in the GSI $^{12}$C ion therapy project where all fractions were monitored with an in-beam PET camera. By further optimizing the nuclear reaction models predicting the positron emitter production also smaller errors might become detectable and the clinically desired millimeter accuracy could be reached [121, 122]. However, the available experimental cross section data for the relevant reaction channels at high energies are scarce [17, 74]. This was the motivation for the activation experiments with protons and $^{12}$C ions presented in this thesis.

## 2.8 Nuclear Reaction Cross Sections

Nuclear reaction probabilities are usually expressed in the form of cross sections which represent the area that the target nucleus presents to the projectile for the interaction process of interest. Cross sections in nuclear and particle physics are typically given in the unit barn (1 b = $10^{-28}$ m$^2$).

### 2.8.1 Cross Section Definitions

The total cross section $\sigma_T$ gives the probability for an interaction in a system of colliding nuclei.

$$\sigma_T = \sigma_R + \sigma_{el} \tag{2.6}$$

$\sigma_T$ consists of the elastic cross section $\sigma_{el}$ for elastic scattering of the projectile from the target nucleus (see Section 2.3.2) and the reaction cross section $\sigma_R$ for inelastic nuclear reactions (see Section 2.3.3) [123, 124]. The values of $\sigma_R$ and $\sigma_{el}$ are typically in the same order of magnitude.
The relative number of ions that penetrate a thin target with thickness $z$ without undergoing a nuclear reaction can be calculated with Equation 2.7

$$\frac{N}{N_0} = e^{-z \cdot \frac{n}{V} \cdot \sigma_R} \tag{2.7}$$

where $\frac{n}{V}$ is the number of target nuclei per volume.
It is difficult to measure $\sigma_R$ directly: Target fragments have only very low energies and most of them will not even leave the target and excitation of the projectile or target nuclei might only result in slight changes of the kinetic energies and angles. This makes it difficult to detect all types of nuclear reactions that can occur, however, in the intermediate energy range investigated in this work most nuclear reactions lead to fragmentation of the projectile. Therefore, measured quantities like the charge-changing cross section $\sigma_{\Delta Z}$ (projectile loses at least one proton) and the mass-changing cross section $\sigma_{\Delta A}$ (projectile loses at least one nucleon) which only require an appropriate particle identification method can serve as an estimate for $\sigma_R$.
It should be pointed out that the mass-changing cross section does not account for inelastic scatter reactions (see also Section 2.3.3). For most colliding systems this component is negligible but for $^4$He ions a contribution of $10 - 15\%$ (depending on the energy and the target nucleus) to the total reaction cross section has been predicted by optical model calculations [56]. Therefore the inelastic scatter component should be considered separately for radiation transport codes that take into account excitation or fragmentation of target nuclei (particularly Monte Carlo transport codes) and subtracted from the modeled total reaction cross section $\sigma_R$ to compare it to the experimental mass-changing cross sections $\sigma_{\Delta A}$. For deterministic 1D transport codes like YIELD in TRiP98 [35] which consider only projectile fragmentation it is sufficient to model only $\sigma_{\Delta A}$ as an approximation of $\sigma_R$.
If not all reactions but only a particular reaction channel is investigated the reaction can be

written in the form A(a,b)B. A and a describe the target and projectile in the initial state while B and b describe the target residual and ejectiles in the final state. The example reaction channels in Figure 2.8 can be written as $^{12}$C(p, pn)$^{11}$C, $^{12}$C($^{4}$He,$^{4}$ He $^{3}$He n)$^{8}$Be and $^{12}$C($^{12}$C, 3 $\times^{4}$ He $^{2}$H)$^{10}$B. If A, a, B and b are all known like in the illustrated examples the cross sections for these channels are called *exclusive* cross sections. Typically only part of the final state is measured in nuclear physics experiments, either the projectile-like or the target-like part, because this reduces the complexity of the experimental setup considerably. The cross sections obtained in such experiments are called *inclusive* cross sections and the unidentified parts can e.g. be notated with X.

### 2.8.2 Parametrization of the Total Reaction Cross Section

The total reaction cross section $\sigma_R$ is an essential quantity for heavy ion transport calculations. In most heavy ion transport codes $\sigma_R$ is described as a function of the charge and mass of the projectile, the charge and mass of the target and the energy of the colliding system by semi-empirical parametric models which are fine-tuned to experimental data. The cross section predictions obtained from these parametrizations are most realistic for colliding systems which are well characterized by experiments. For unexplored systems their predictions might still be reasonable due to the underlying systematics, but for projectile-target combinations of special interest it is preferable to check the models against measured cross section data.

#### 2.8.2.1 Geometrical Model by Bradt and Peters

Many parametrizations of $\sigma_R$ are based on the geometrical model by Bradt and Peters [125]. Its basic formula is shown in Equation 2.8:

$$\sigma_R = \pi r_0^2 (A_P^{1/3} + A_T^{1/3} - \delta)^2 \tag{2.8}$$

where $r_0 \approx 1.1$ fm is the proportionality constant in the nuclear radius formula ($r = r_0 \cdot A^{1/3}$), $A_P$ and $A_T$ are the mass numbers of the projectile and target nuclei and $\delta$ is the so-called transparency parameter. If $\delta$ is set to zero, then the reaction cross section $\sigma_R$ corresponds to that of two colliding hard spheres which is a good approximation for heavy ion collisions at high energies ($> 1$ GeV/u). If $\delta$ is varied as a function of energy, the fact that $\sigma_R$ shows an energy dependence at energies below 1 GeV/u can be reproduced. The energy dependence of $\sigma_R$ for nucleus-nucleus reactions at intermediate energies originates from the free nucleon-nucleon total cross sections $\sigma_T^{pp}$ and $\sigma_T^{np}$ which both show a minimum at a few 100 MeV [126]. These *transparency effects* are associated with the behavior of the nucleon scattering phase shifts [124]. The interaction properties of the nucleons are reflected in the macroscopic behavior of nuclei because a nucleus-nucleus reaction can be understood as a superposition of multiple nucleon-nucleon interactions.

#### 2.8.2.2 Parametrization by Tripathi

The widely used parametrization by Tripathi et al. [127] is inspired by the simple geometrical model by Bradt and Peters. They extended the model by a Coulomb term to take the electrical repulsion of the projectile and target nuclei, preventing that they can come close enough for a nuclear reaction at low energies (the so-called Coulomb barrier), into account.
In the Tripathi parametrization $\sigma_R$ is calculated according to Equation 2.9.

$$\sigma_R = \pi r_0^2 (A_P^{1/3} + A_T^{1/3} + \delta_E)^2 \left(1 - \frac{B}{E_{cm}}\right) \tag{2.9}$$

$B$ is the energy dependent Coulomb barrier and is calculated according to Equation 2.10.

$$B = \frac{1.44 Z_P Z_T}{r_P + r_T + 1.2 \dfrac{A_P^{1/3} + A_T^{1/3}}{E_{cm}^{1/3}}} \tag{2.10}$$

where $r_P$, $r_T$, $Z_P$ and $Z_T$ are the radii and atomic numbers of the projectile and target nuclei.

The energy dependence of $\sigma_R$ at intermediate energies is taken into account by calculating $\delta_E$ according to Equation 2.11.

$$\delta_E = 1.85S + 0.16 \frac{S}{E_{cm}^{1/3}} - C_E + 0.91 \frac{(A_T - 2Z_T)Z_P}{A_T A_P} \tag{2.11}$$

$S$ is called the mass asymmetry term and is related to the volume overlap of the colliding system and is given by Equation 2.12.

$$S = \frac{A_P^{1/3} \cdot A_T^{1/3}}{A_P^{1/3} + A_T^{1/3}} \tag{2.12}$$

The $C_E$ term mimics the energy dependence of $\sigma_R$ at intermediate energies and is calculated according to Equation 2.13. It is a purely empirical term which represents a fit to the experimental data available at the time when the Tripathi parametrization was designed (1996). $E$ is the kinetic energy in MeV/u.

$$C_E = D \cdot (1 - e^{-E/40}) - 0.292 \cdot e^{-E/792} \cdot cos(0.229 \cdot E^{0.453}) \tag{2.13}$$

$C_E$ contains also the term $D$ which scales the cross section according to the nuclear density of the projectile $\rho_P$ and target $\rho_T$ with respect to the $^{12}$C +$^{12}$ C system and is calculated with Equation 2.14.

$$D = 1.75 \cdot \frac{\rho_P + \rho_T}{\rho_C + \rho_C} \tag{2.14}$$

The nuclear density $\rho$ of a nucleus with mass A is calculated from the nuclear radius $r$ with the hard sphere model by Equation 2.15

$$\rho_A = \frac{A}{\frac{4}{3}\pi r^3} \tag{2.15}$$

The terms for $C_E$ and $D$ given above reproduce the experimental $\sigma_R$ values with good accuracy over a large span of colliding systems but differences between model and experiment were observed for light systems where protons are involved as well as for $^4$He and lithium projectiles. Thus, for light systems where protons are involved an extension of the parametrization has been designed, later [128]. For lithium projectiles it was suggested to divide the value of $D$ according to Equation 2.14 by a factor of three and for $^4$He ions a modified formula for $D$ was proposed (Equation 2.16) which led to a good agreement with the experimental data available in 1996.

$$D_{^4He} = 2.77 - 8.0 \cdot 10^{-3} \cdot A_T + 1.8 \cdot 10^{-5} \cdot A_T^2 - \frac{0.8}{1 + e^{(\frac{250-E}{75})}} \tag{2.16}$$

The Tripathi parametrization is a semi-empirical model - the general scaling laws are derived from geometrical properties of the projectile and target nuclei while the terms $C_E$ and $D$ are based on fine-tuning to experimental data. The Tripathi formula is implemented in many popular heavy ion transport codes, either in its original form (e.g. in Geant4 [8], PHITS [104] or TRiP98 [4]) or in an empirically modified form (e.g. in FLUKA [129]).
Other comparable $\sigma_R$ parametrizations for heavy ions are e.g. those by Kox [123] and Shen [130].

## 2.9 Synergies with Space Radiation Research

Another research field besides particle radiotherapy that might benefit from the experimental cross sections presented in this work, in particular the data for $^4$He projectiles, is space radiation protection [57, 131]. In astronomical objects like supernovae, protons and heavy ions are accelerated to energies that are high enough to penetrate any shielding. Nuclear fragmentation of these galactic cosmic rays, e.g. within the structures of a spacecraft, has to be taken into account because such reactions change the radiation field that the astronauts and electronic devices inside a spacecraft are exposed to with respect to the primary radiation field in free space. $^4$He ions make up $\sim 10\%$ of the primary galactic cosmic radiation and their energy spectrum peaks at intermediate energies, strongly overlapping with the therapeutic energy range investigated in this work. Therefore accurate $^4$He ion transport models are not only required for radiotherapy but also in the field of space radiation protection [56, 132]. Actually the Tripathi parametrization of $\sigma_R$ described in Section 2.8.2.2 has originally been designed for space radiation studies and in some radiation transport codes it is called the NASA model.
Monte Carlo [133, 134] or deterministic [135] heavy ion transport codes are used for different purposes in the field of space exploration like mission planning, risk assessment or

radiation shielding design. However, there are still large gaps in the experimental cross section databases for the validation of nuclear reaction models and transport codes in the space radiation energy range [136, 137]. The $^4$He experimental dataset presented in this thesis contributes to fill these gaps and an expansion of the present experiments towards higher energies ($> 220$ MeV/u) could be of interest for space radiation research.

## 2.10 Scintillation Detectors

A common detector type for nuclear physics experiments are scintillation detectors. A scintillation detector (short form: scintillator) consists of a material which emits light as a result of energy deposition by ionizing radiation and a device which can amplify the light signal, e.g. a photomultiplier tube. The light yield is (in a good approximation) proportional to the energy deposited by an ionizing particle in the scintillator.

### 2.10.1 Plastic Scintillators

One class of scintillation materials are *organic* scintillators which consist of aromatic molecules that show a well-defined fluorescence due to their $\pi$-electron structure [138]. The electronic transitions which cause the light emission as a follow of energy deposition by ionizing radiation are typically very fast in such materials (typically in the order of ns). For being suited as an organic scintillator the material needs to be transparent to its own emission wavelength. Furthermore the scintillation efficiency (light output per deposited energy) of a material is an important characteristic for its application as a radiation detector.
If an organic scintillator is dissolved in a material that can be polymerized (e.g. styrene) the resulting material is called a plastic scintillator. By adding also a *waveshifter* molecule which converts the scintillation light into photons with a longer wavelength, the light output spectrum can be adapted to the spectral sensitivity of the photodetector used (e.g. a photomultiplier) - however this typically reduces the timing performance of the material. Plastic scintillators are the most common form of organic scintillators because they can be manufactured in any shapes and are relatively inexpensive. They are well suited for fast timing applications (e.g. as a trigger or for time-of-flight measurements) due to their short scintillation pulses and fast signal rise time. A typical multi-purpose plastic scintillation material is BC-400, which was used to build the plastic scintillation detectors used for the experiments described in this work.

### 2.10.2 $BaF_2$ Scintillators

Another class of scintillation materials are *inorganic* scintillators [138]. In these materials the scintillation effects are not caused by the electronic structure of a single molecule but a result of the crystal lattice of the material. Often an activator impurity is added to the materials to increase their scintillation efficiency. Many inorganic scintillation materials have a very high effective atomic number and a high density which makes them useful to build compact detectors with a high absorption or stopping power.

For the experiments described in this work $BaF_2$ detectors were used for charged particle and gamma photon detection. $BaF_2$ has a very fast rise time, a high density of 4.893 g/cm$^3$ and a high effective atomic number of 52.2. A disadvantage of $BaF_2$ is that its scintillation light lies in the UV range and can therefore not be detected with standard photomultipliers but requires special models equipped with a quartz window. The large $BaF_2$ detector used for the $^4$He experiments described in this work was originally built as a prototype for the TAPS spectrometer [139]. Figure 2.13 shows photos of the TAPS $BaF_2$ crystal taken during refurbishment.

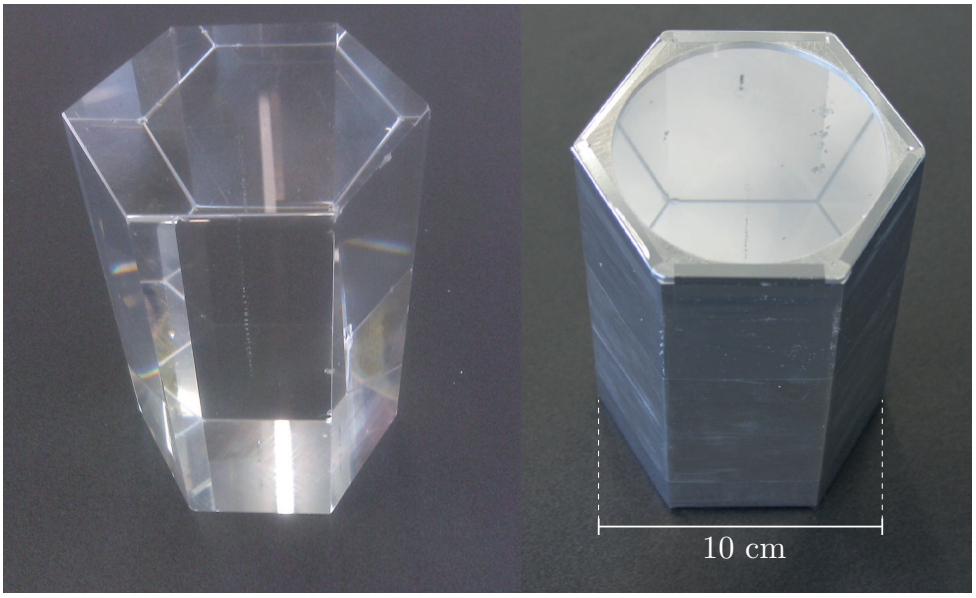


**Figure 2.13:** TAPS prototype $BaF_2$ crystal unwrapped (left) and wrapped with reflective foil (right). The front face was left open because it was later used to attach the photomultiplier tube.

$BaF_2$ shows a characteristic scintillation pulse, consisting of two time components: a fast component decaying with $\sim 0.6$ ns and a slow component decaying with $\sim 600$ ns [140]. These two light components originate from different luminescence mechanisms and their relative contribution to the overall light signal depends on the type of ionizing radiation or, more precisely, on the microscopic energy deposition pattern in the $BaF_2$ crystal. For example, a $BaF_2$ signal caused by a high energy photon shows practically no tail from the slow component because only the fast component is excited and $BaF_2$ signals caused by ions of different atomic number show different ratios between the fast and the slow component, practically independent of the deposited energy [141, 142]. Owing to this effect, a $BaF_2$ pulse shape analysis allows the separation between ions of different atomic number such as He ions and their H fragments as done for the present experiments.

### 2.10.3 Particle Identification with Scintillator Telescopes

For measurement of nuclear fragmentation cross sections, the primary particles transmitted through a target have to be separated from nuclear fragments. E.g. in the projectile

fragmentation experiments described in this work the relative number of transmitted primary particles as a function of target thickness had to be measured.
The different projectile fragments from nucleus-nucleus reactions are produced at similar velocities (see Section 2.3.3) and therefore a measurement of their energy loss $\Delta$E in a thin scintillator (a measure of $dE/dx$) gives already a rather good identification of the atomic number $Z$. However in such pure $\Delta$E spectra the Landau tails (see Figure 2.6) of the energy loss distributions of lower $Z$ particles can overlap with the distribution of the species with higher $Z$. One technique to reduce this overlap is to perform two or more redundant energy loss measurements, e.g. with a stack of scintillators or semiconductor detectors (as done e.g. by Zeitlin et al. [143]), called $\Delta\mathrm{E} - \Delta\mathrm{E}$ telescope. Another identification method is to measure not only the energy loss but also the energy of the particles to be identified. The kinetic energy E of a non-relativistic particle (relativistic effects are still moderate at the energies used in this work) with the mass $A$ is connected with its velocity $v$ by

$$E = \frac{1}{2}Av^2 \tag{2.17}$$

If this term is converted to $v^2$ and put into Equation 2.1 one can observe the relation

$$dE/dx \sim \frac{AZ^2}{E} \tag{2.18}$$

This means that the simultaneous detection of $\Delta$E and E can be used to separate particles with different $AZ^2$ products [144], and thus provides an isotopic separation. In an experiment this can e.g. be achieved by combining a thin ($\Delta$E) and a thick (E) scintillator to a so-called $\Delta\mathrm{E} - \mathrm{E}$ telescope. For light ions ($Z < 4$) the $AZ^2$ product is a unique identifier while for heavier ions there are overlaps between different species. A requirement for the $\Delta\mathrm{E} - \mathrm{E}$ technique is a good E measurement, however, this is not straightforward with a thick scintillator. A considerable fraction of the primary ions transmitted through the target which should be detected undergo nuclear reactions within the thick E detector. Some of the long-range fragments produced in these reactions, especially the neutrons, may escape from the detector and carry a part of the total energy away.
There are also potential issues for the $\Delta$E measurement. For measuring total cross sections detectors with large acceptance are required. However, if the telescope is placed close to the target there is a high probability that multiple fragments hit the telescope simultaneously and in the $\Delta$E spectra their energy losses sum up to values that can either be intermediate or overlap with the single ion peaks.
A general strategy for particle identification systems is to collect as much redundant information about the particles as possible to eliminate perturbations due to detector effects. Even if not applied in the experiments described in this thesis, further improvement of particle identification would be possible by introducing flight gaps and measuring time-of-flight spectra and by using magnetic fields to separate the primary particles and fragments by their momentum. The use of pixelated $\Delta$E detectors and application of particle tracking methods would be appropriate to reduce the problems caused by fragment multiplicities. However, such extensions of the experimental setup described in this thesis would greatly increase the experimental effort.

# 3 Materials and Methods

The following chapter gives an overview about the experimental setups used in the present work and the methods applied for data processing and analysis.

## 3.1 Data Acquisition

A Tektronix DSA 72004C oscilloscope was used for acquisition of the scintillator signals in event-by-event mode. The signals were recorded as waveforms by means of fast sampling. The hardware sampling rate of the oscilloscope is 16 GS/s with a resolution of 8 Bit. The effective sampling rate in the experiments was between 2.0 and 3.1 GS/s with an effective resolution close to 10 Bit. The oscilloscope can store data in its RAM with low deadtime between consecutive events, but every few $1000 - 10000$ events (the actual number can be set but depends also on the sample rate and digital resolution) it needs to save the stored data on a hard drive. During these few seconds, the oscilloscope does not accept any triggers which causes short gaps where no events can be recorded.

## 3.2 Data Processing

For data processing and analysis, the ROOT data analysis framework ROOT [145] was used and extended by self-developed routines.
The recorded waveforms were post-processed and some changes and corrections were applied (inverting from negative to positive signal values, baseline correction, flagging of detected double hits). To reduce the large amount of data to analyze, characteristic quantities (peak value, integral, and the ratio of integral-to-peak) were derived from the corrected waveforms and stored separately while the event-wise correlation of the individual detector channels was maintained.

## 3.3 $BaF_2$ Pulse Shape Analysis

The scintillator signals were recorded as waveforms $f(t)$. This technique allows an offline-characterization of the shape of a scintillator pulse from the waveform. The pulse shape $PS$ of the $BaF_2$ signal was calculated for every event $i$ according to Equation 3.1:

$$PS_i = \frac{\Sigma f_i(t)}{f_{i,max}} \tag{3.1}$$

where $\Sigma f_i(t)$ and $f_{i,max}$ are the integral of the signal and the peak value within the recorded time window of event $i$ as illustrated in Figure 3.1. It shows normalized $BaF_2$ signals recorded for three different ions with the same velocity (200 MeV/u protons, $^4$He

and $^{12}$C). This example demonstrates the particle identification capability of a $BaF_2$ pulse shape analysis but also that the difference between protons and $^4$He ions is hard to resolve.

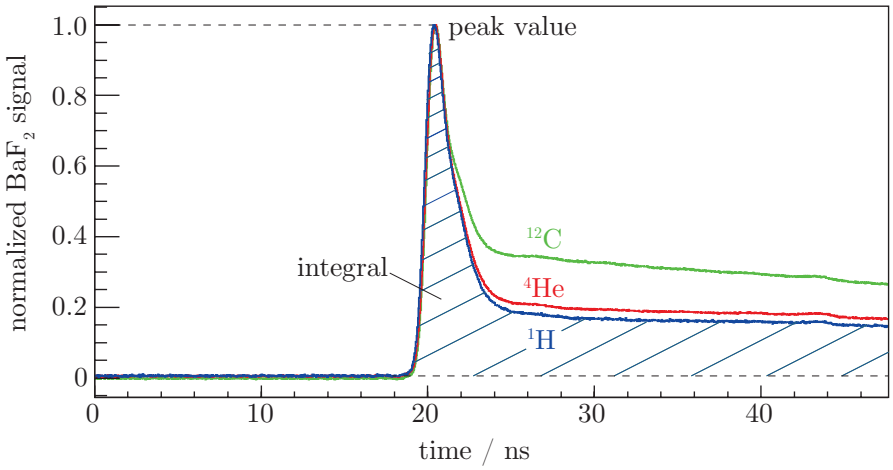


**Figure 3.1:** Measured $BaF_2$ signals normalized to their peak value recorded for monoenergetic protons ($^1$H ions), $^4$He and $^{12}$C at 200 MeV/u. The signals were averaged over 100 events with full energy deposition to reduce the noise. Due to the normalization to the peak value the area below the curves represents the pulse shape PS.

As can be seen in Figure 3.1, the slow scintillation component of $BaF_2$ has a very long decay time and was therefore not fully recorded. However, in this case, no correction for the missing part of the tail is required because the $BaF_2$ pulses did practically not have a time jitter because the rise time of the trigger pulse is much shorter than the integration window.

## 3.4 Experimental Setup I: Projectile Fragmentation

The $^4$He fragmentation experiments described in the following were conducted at HIT, Heidelberg, in two separate measurement campaigns: In 2017 $^4$He charge- and mass-changing cross sections on C targets were measured and in 2018 the experiment was extended to Si, O and H targets. In addition to those elemental cross section measurements, also direct measurements on water targets were performed during the second experiment. The results of the two measurement campaigns are published in two separate articles [146, 147] where descriptions of the method similar to those in the following section can be found.
Figure 3.2 shows a schematic of the experimental setup which is based on the attenuation method using a $\Delta E - E$ scintillator telescope as well as a photo taken during the experiment in 2018. A pencil beam of $^4$He ions impinged on a start scintillator (1 mm thick BC-400-like) which triggered the data acquisition. The ions penetrated the target and were then stopped within a $\Delta E - E$ scintillator telescope (5 mm thick BC-400-like and 14 cm long $BaF_2$, both hexagonal with inner diameters of 10 cm and 8.5 cm, respectively).

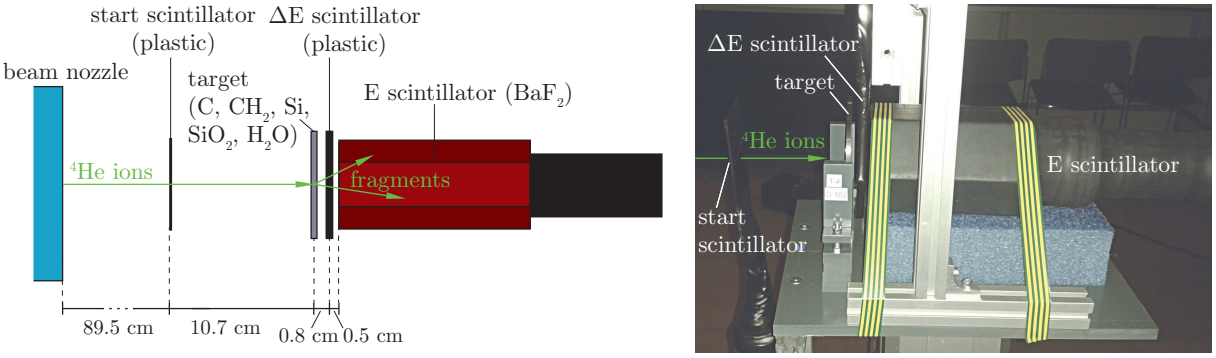


**Figure 3.2:** Schematic (left) and photo (right) of the experimental setup used at HIT to measure charge- and mass-changing cross sections for $^4$He ions impinging on different targets.

The number of transmitted $^4$He ions and $^3$He fragments generated within the target could be determined by correlation of the signals from the ΔE scintillator with the signals from the $BaF_2$ scintillator. The larger angular coverage of the ΔE scintillator compared to the $BaF_2$ scintillator was exploited to ensure that only a negligible fraction of primary ions could be scattered out of the telescope's acceptance (65° to the beam axis in the 2017 experiment and 81° in the 2018 experiment). This is important because full geometrical acceptance for the primary ions is required to measure total inelastic cross sections as presented here. The measurements were performed at five different primary energies (80, 90, 130, 180 and 220 MeV/u). Between $2 \times 10^5$ and $8 \times 10^5$ events were recorded for each energy and target thickness.
Figure 3.3 shows the waveforms of the three detector signals recorded by the data acquisition system for an example $^4$He event.

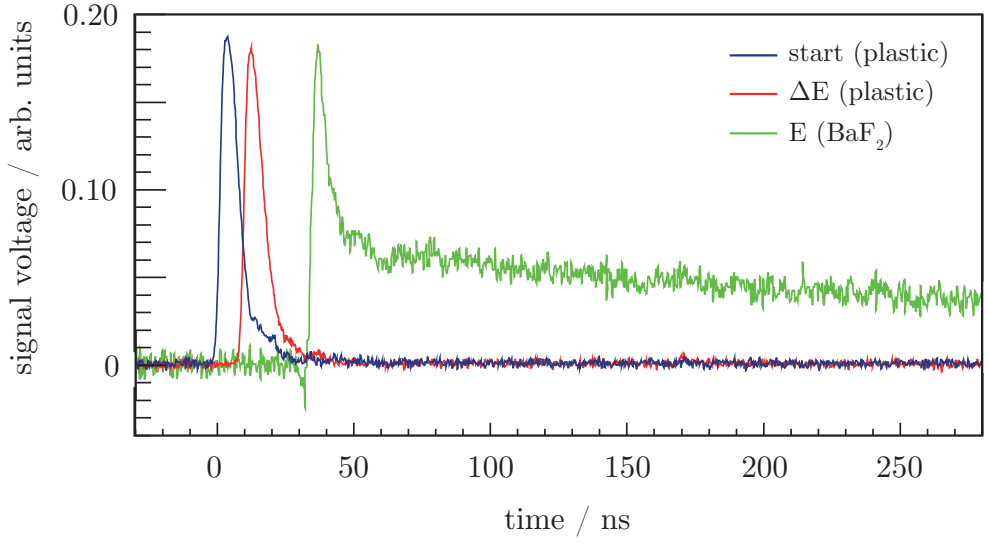


**Figure 3.3:** Signal waveforms of the three detector channels (start, ΔE and E) for an example $^4$He event.

The start and ΔE plastic scintillator pulses look similar because they consist of the same BC-400-like material and the $BaF_2$ pulse shows the two characteristic scintillation components that can be analyzed for particle identification (compare with Figure 3.1).

### 3.4.1 Targets

In Table 3.1 the different targets used for the $^4$He fragmentation cross section measurements are listed. For each $^4$He energy used also a no-target measurement was performed to correct by the reactions occurring within the beam nozzle, the start scintillator and the air gap. For most energy-material combinations at least two targets with different thicknesses were irradiated to have redundant information and to be able to check for robustness of the data analysis method.

**Table 3.1:** List of targets used for $^4$He cross section measurements.

| Target material | density / g/cm$^3$ | thickness / cm |
|---|---|---|
| C | 1.83 | 0.5, 0.7, 1.0, 1.2 |
| $CH_2$ | 0.947 | 0.5, 1.0, 2.0 |
| Si | 2.33 | 0.4, 0.8, 1.6 |
| $SiO_2$ | 2.204 | 0.4, 0.8, 1.6 |
| $H_2O$ | 1.0 | 2.22, 3.25 + flask |

Measurements were performed with elemental (C and Si) and compound targets ($CH_2$ and $SiO_2$). The latter were used to obtain elemental cross sections on H and O targets (the constituents of water). By subtracting the cross sections measured on the elemental targets from those measured on the compound targets the cross section of the other element can be calculated according to Equation 3.2 and Equation 3.3:

$$\sigma^{\mathrm{H}} = \frac{\sigma^{\mathrm{CH_2}} - \sigma^{\mathrm{C}}}{2} \tag{3.2}$$

$$\sigma^{\mathrm{O}} = \frac{\sigma^{\mathrm{SiO_2}} - \sigma^{\mathrm{Si}}}{2} \tag{3.3}$$

For redundancy and to check for consistency with the H and O also a measurement using $H_2O$ targets at a primary energy of 220 MeV/u was performed. For this purpose cell culture flasks (Corning 3073 and T-150) with two different thicknesses (2.22 cm and 3.25 cm + 2 polystyrene walls of 0.18 cm thickness) were filled with water. To account for the reactions occurring within the walls of the flasks, an additional measurement for each of the empty flasks was performed. A photo of the $H_2O$ target measurement is shown in Figure 3.4

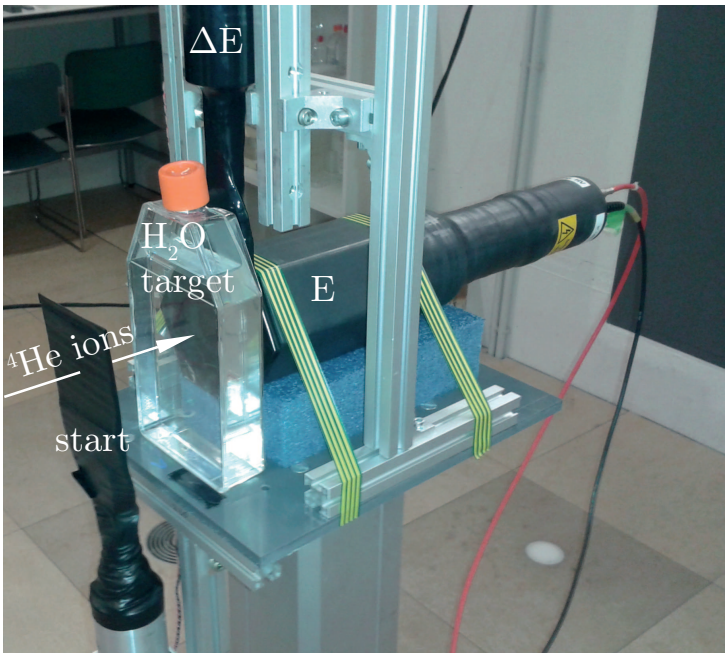


**Figure 3.4:** Photo of the experimental setup used at HIT for measuring $^4$He fragmentation in a $H_2O$ target.

### 3.4.2 Alignment and Beamspot Characterization with CMOS Sensor

At HIT the therapy control system adjusts the beamspot position automatically by a dynamic feedback loop from the position-sensitive MWPCs within the beam nozzle to the scanner magnets. However, at low beam intensities as required for fragmentation experiments the MWPCs do not respond and thus no correction of the beamspot position can be applied by the system. To align the experimental setup as precisely as possible the position, size and shape of the beamspot at low intensity were determined in advance with a MIMOSA28 CMOS pixel sensor with high spatial resolution [148] before the experiment in 2018. Figure 3.5 shows the measured beamspot profiles for the three $^4$He energies used.

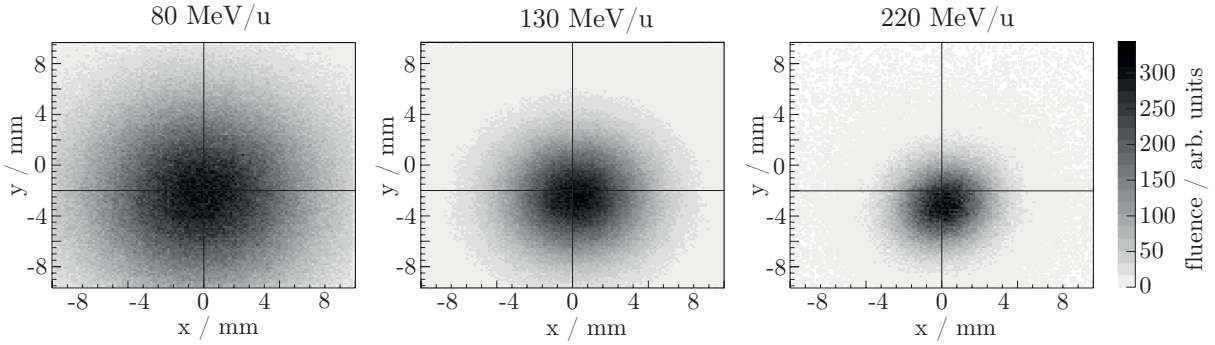


**Figure 3.5:** Beamspots at low intensity measured with the MIMOSA28 CMOS sensor at the isocenter for three $^4$He energies. The coordinate system corresponds to the positioning lasers in the HIT experimental room and the lines mark the center of the aligned scintillator telescope.

The beamspot gets broader towards lower energies due to the increased lateral scattering within the beam nozzle ($\sim$ 2 mm water equivalent thickness). A vertical shift relative to the isocenter (marked by positioning lasers in the experimental room) can be observed for all three energies. Based on these CMOS measurements the scintillator telescope was aligned with a vertical shift of 2 mm relative to the positioning lasers. For the highest energy (220 MeV/u) there was still a shift of $\sim$ 1 mm left in the final alignment. However, for comparison, the inner diameter of the $BaF_2$ scintillator (8.5 cm) is large against this shift and against the size of the beamspots. Thus the scintillator telescope had practically full acceptance for the primary $^4$He ions for all energies.

### 3.4.3 Data Analysis

For the analysis of the data recorded during the $^4$He experiments at HIT, the ROOT data analysis framework was used and extended by self-developed routines.

#### 3.4.3.1 Selection of Valid Triggers

At HIT the beam is extracted from the synchrotron by the RF-knockout technique with a spill length of up to 10 s. The intensity is controlled by a feedback loop from the monitor IC to the RF-knockout cavity, called dynamic intensity control (DIC), equivalent to the beam position control using the MWPCs described in Section 3.4.2. Like the position control, also the DIC does not work at low intensities and therefore the particle rate can fluctuate strongly during single particle experiments at HIT. Figure 3.6 shows the accepted trigger rate of the data acquisition system as a function of time for one example dataset. The slow synchrotron extraction was adjusted for a mean intensity of typically 1000 ions/s while the actual intensity varied between $\sim$ 500 and 3000 ions/s. It can be observed that the intensity within each spill was rather stable but fluctuated strongly from spill to spill.

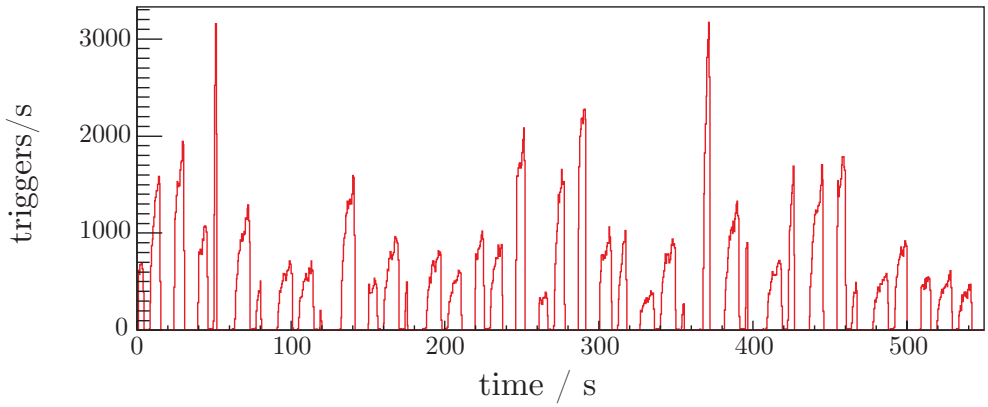


**Figure 3.6:** Accepted trigger rate of the data acquisition system as a function of time during a $^4$He ion experiment at HIT. Strong intensity variations from spill to spill can be observed.

To exclude beam contaminants and double hits, two selection criteria were defined for the start detector: Only events where the peak (to exclude double hits occurring almost simultaneously) and the integral (to exclude double hits occurring one after another but both within the detection window) calculated from the waveforms of the start scintillator lay within ±2.5 standard deviations from the corresponding average value were taken as valid events. This selection is shown for one example in Figure 3.7 where also the two types of double hits are indicated.

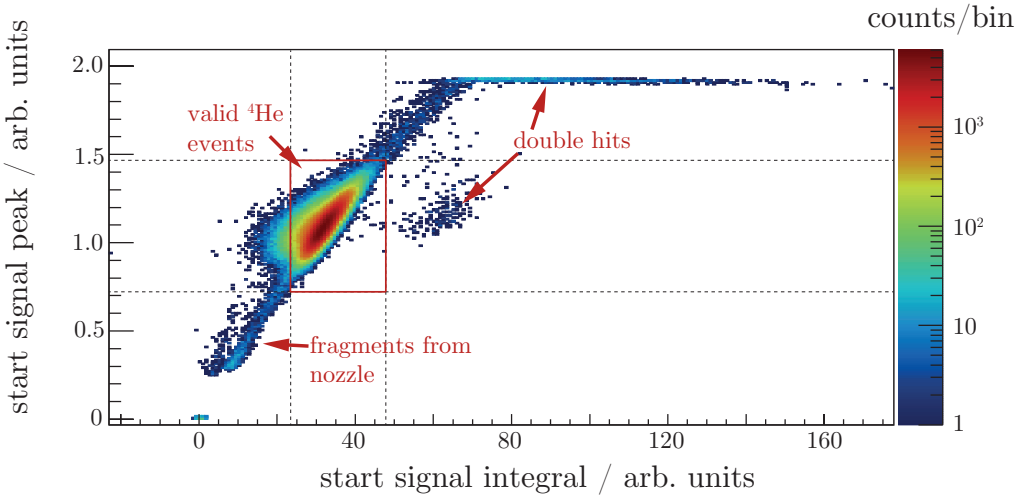


**Figure 3.7:** Identification of primary $^4$He events with the start scintillator. The peak value and the integral of the waveforms are both analyzed event-wise which allows an exclusion of false triggers and double hits. The peak value went into saturation for the simultaneous double hits. The valid $^4$He events are surrounded in red.

There were still some false-trigger events left which met the above described criteria, e.g. due to activation of the start scintillator or by cosmic radiation. Such events, where neither the ΔE scintillator nor the $BaF_2$ scintillator have responded could be identified by the $BaF_2$ integral and the ΔE integral both being $\sim 0$ and were also discarded. The number of such noise events scaled with the measurement time and did not exceed a few permille of the overall event number for any measurement.

#### 3.4.3.2 Identification of He ions

The He ions leaving the target were identified by a 2D-analysis of the integral of the ΔE scintillator signal compared to the pulse shape of the $BaF_2$ scintillator signals (ΔE-pulse-shape). For this purpose, an analysis code was developed to automatize the identification process as much as possible.
Figure 3.8 shows two examples of ΔE-pulse-shape spectra in comparison to the ΔE-E spectra recorded for the same measurements of 130 MeV/u $^4$He ions either without target or with a 16 mm Si target.
As can be noticed in the spectra measured without target, there were already fragmentation reactions occurring within the beam nozzle, the air gap from the nozzle to the telescope and the start scintillator. Therefore, the number of $^4$He ions present at the no

target runs were identified just like for the measurements with target and taken as the number at 0 cm target thickness to normalize to for the cross section determination (see Section 3.4.3.4).

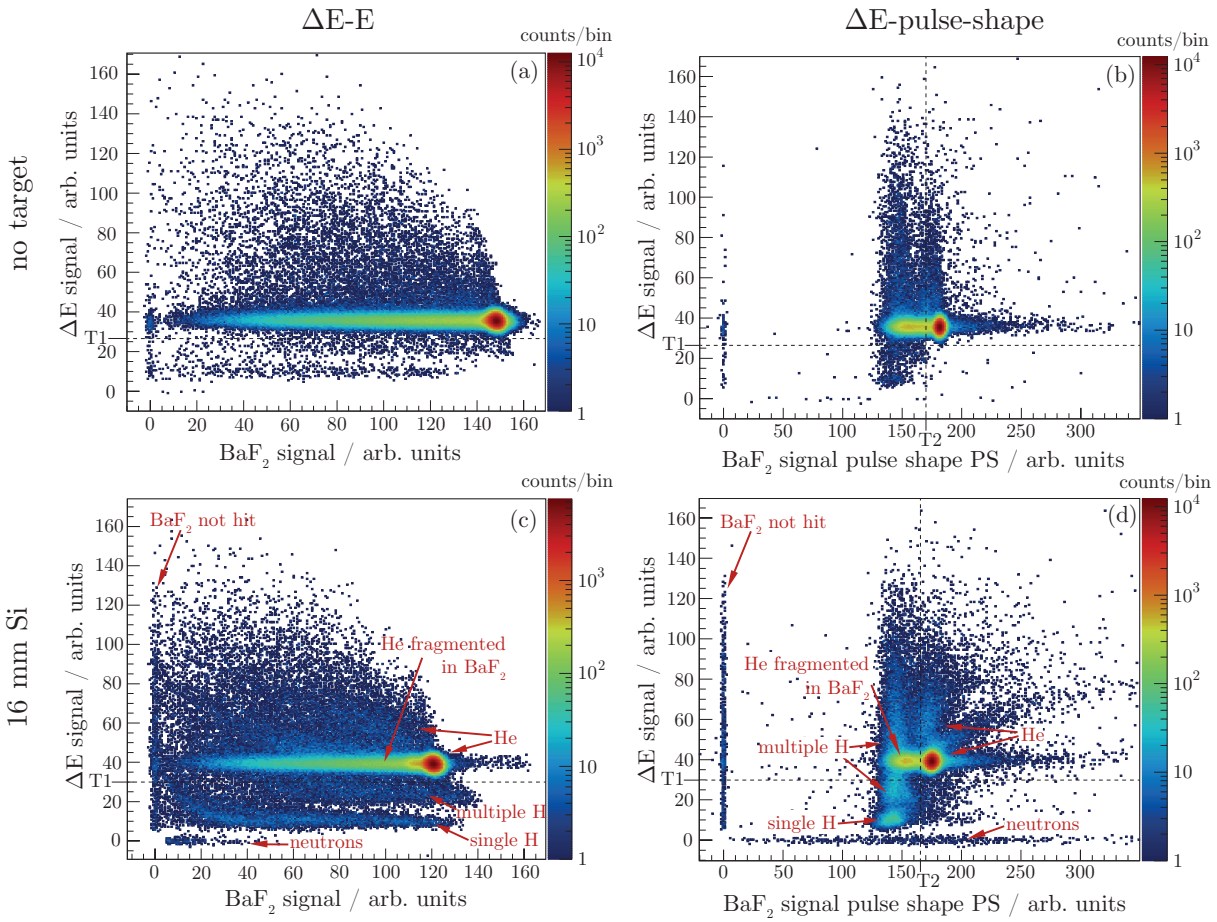


**Figure 3.8:** Examples of ΔE-E spectra ((a) and (c)) and ΔE-pulse-shape spectra ((b) and (d)) for 130 MeV/u $^4$He ions with no target ((a) and (b)) and after traversing 16 mm of Si ((c) and (d)). Double hits and noise events were excluded by cuts on the start scintillator signal. The thresholds T1 and T2 have been set by hand to separate the He events in the upper right corner of the ΔE-pulse-shape plots from their H fragments. The origin of the event clusters visible in the spectra for 16 mm Si is indicated by the arrows. A detailed description is given in the text.

The cluster around the main peak visible in both, the ΔE-E and the ΔE-pulse-shape plots, was generated by the $^4$He ions transmitted through the target and the $^3$He fragments which can not be well separated by eye from the primary ions. The shift of the main peak in the E signal from the no target measurement to the 16 mm Si target measurement is due to the energy loss within the target. As mentioned in Section 2.10.2, the pulse shape is not affected by such changes in energy.
Single H fragments entering the telescope created a cluster at 25% of the ΔE of the primary $^4$He ions as the ΔE signal scales with $Z^2$ for ions with the same velocity (see Section 2.3.1).
The large geometrical acceptance of the detector telescope used and the production of

at least two H fragments per charge-changing reaction lead to several multiplicity states ($^1$H + $^1$H, $^1$H + $^2$H, $^1$H + $^3$H, $^2$H + $^2$H) which added up to the event cluster arising at a factor of two higher $\Delta$E values and beyond but with $BaF_2$ pulse shapes as observed for single H fragments. Multiplicities involving prompt gamma photons and pions are very rare and therefore neglected in the present analysis. Multiplicities involving neutrons are more frequent, in particular together with $^3$He fragments. The efficiency of the $\Delta$E scintillator to fast neutrons is $< 1\%$ but still the $^3$He + n events create visible peaks in the spectra for some target materials (see Section 3.4.3.3). For the $BaF_2$ scintillator the probability to respond to neutrons is higher, since its neutron efficiency is $\sim 10 - 20\%$ [149] but its pulse shape is only slightly affected by the small energy depositions via (n,p) reactions (typically a few 10 MeV). The few events with a larger neutron contribution show $BaF_2$ pulse shapes shifted to lower values and are considered in the *He fragmented in $BaF_2$* correction (see below).

As can be seen in both, the $\Delta$E-pulse-shape and the $\Delta$E-E plot, the main He peak is smeared, even in the spectra measured with no target. This smearing is mainly due to nuclear reactions of the He ions within the thick $BaF_2$ scintillator ($\sim 10 - 20\%$ of the events). This fragmentation inside the E detector resulted in a) some energy being deposited by H fragments instead of He ions and b) some energy to be carried out of the detector volume by long range fragments like deuterons, tritons or neutrons. These effects explain why the events where He ions fragmented inside the $BaF_2$ scintillator showed a) pulse shapes intermediate between H and He events and b) a reduced energy deposition compared to the main He peak. These fragmented He events overlap partially with the multiple H cluster in both, the $\Delta$E-E and the $\Delta$E-pulse-shape spectra, which makes a clear identification of such events impossible with the present detector setup.

It can clearly be seen that the He ions are better separated in the $\Delta$E-pulse-shape than in the $\Delta$E-E plot, which has been used for particle identification in previous fragmentation experiments [71, 72]. This better particle identification capability was the justification for the higher experimental effort to additionally obtain the $BaF_2$ pulse shape information for the work presented here.

For the separation of the He ions from their fragments by the developed analysis code, two thresholds (T1 and T2, one for $\Delta$E and one for the pulse shape) needed to be set by hand. The events where both thresholds were exceeded (upper right in the $\Delta$E-pulse-shape plots) are considered to be solely He ions ($^3$He and $^4$He). The $\Delta$E spectrum of these clearly identified He events (events with a $\Delta$E higher than threshold T1 and with a pulse shape higher than threshold T2) was matched with the peak in the $\Delta$E spectrum of the overlap region (events with a pulse shape below threshold T2) to estimate the number of overlapping He events. This is reasonable because the fragmentation within the $BaF_2$ scintillator, which caused the overlap, can be considered as being fully independent of the energy deposition within the $\Delta$E scintillator.

Finally, adding the estimate of the He events in the overlap region to the number of clearly identified He events gave the overall number of He ions leaving the target as required for determination of the charge-changing cross section. This identification routine had to be applied for every energy and every target thickness.

As shown in Figure 3.2 the $\Delta$E scintillator had a slightly larger radius than the $BaF_2$ scintillator. The number of ions detected only by the $\Delta$E scintillator but not by the $BaF_2$ scintillator (E and PS $\sim 0$ in Figure 3.8) was $< 0.2\%$ of the overall event number for all measurements. This proves that only a negligible fraction of primary ions was scattered

past the telescope. Therefore, the geometrical acceptance of the detector telescope was sufficient to calculate inelastic cross sections from the measured number of He ions.

#### 3.4.3.3 Separation of the Identified He Ions into $^3$He and $^4$He

For determination of the mass-changing cross section the fragmentation channel of $^4$He into $^3$He must also be considered. The ratio of the $^3$He fragments to the $^4$He ions was obtained by fitting the ΔE spectrum of the identified He events with the sum of a Gauss function (representing the $^4$He ions) and a Landau function (representing the $^3$He ions). Some energy-target combinations required a second Landau function because a significant fraction of $^3$He events show a neutron coincidence in the ΔE scintillator creating the small peak right to the main peak in the Landau fraction.

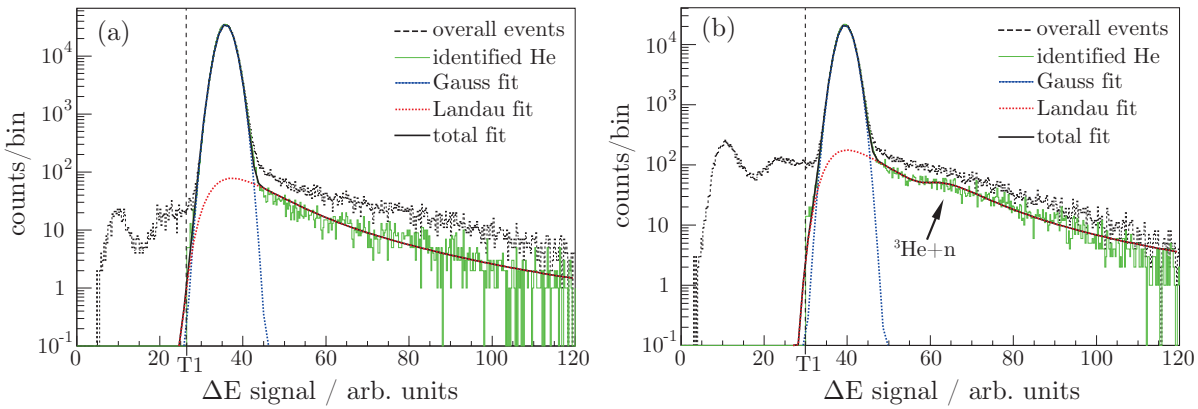


**Figure 3.9:** Examples of ΔE spectra for 130 MeV/u $^4$He ions with no target (a) and after traversing 16 mm of Si (b). Double hits and noise events were excluded by cuts on the start scintillator signal.

In Figure 3.9 a typical ΔE spectrum compared with the separated He events and the Gauss and Landau fit functions is shown. The fitting approach is reasonable because the energy spectrum of the primary $^4$He ions is still relatively sharp after traversing the thin targets while the $^3$He fragments are produced with a broader energy distribution (and therefore also a broader ΔE distribution) due to the kinematics of the involved nuclear reactions. The $^3$He to $^4$He ratio could be calculated from the ratio of the integrals of the two fit functions (Gauss and single or double Landau).
In fact the $^4$He fraction also contributed slightly to the tails in the ΔE spectra of the He ions because the energy deposition of heavy charged particles follows a Landau distribution in thin absorbers (see Figure 2.6). This contribution could be estimated from the Landau fits obtained for the no-target measurements, where the beam should have had only a minor $^3$He contamination, and subtracted from the integrals of the $^3$He fits obtained for the target-in measurements.

#### 3.4.3.4 Cross Section Calculation

The mean interaction length $\lambda$ was obtained for every energy by fitting the measured values for the number of remaining ions $N$ as a function of target thickness $z$ relative to the number of ions at 0 cm target thickness $N_0$ with the fit function according to Equation 3.4.

$$\frac{N}{N_0}(x) = A_0 \cdot e^{-z/\lambda} \tag{3.4}$$

The amplitude parameter $A_0$ was used to finetune the fit and fluctuated only slightly around 1 (less than 1‰). Finally, the fit parameter $\lambda$ was converted into the nuclear cross section $\sigma$ according to Equation 3.5.

$$\sigma = \frac{1}{\lambda \cdot n/V} \tag{3.5}$$

where $n/V$ is the nuclei density (number of nuclei or molecules $n$ per target volume $V$) of the target material.
For each energy, the charge-changing cross section $\sigma_{\Delta Z}$ was calculated from the fit parameter $\lambda_{He}$ for the relative number of remaining He ions ($^4$He plus $^3$He) behind the target and accordingly the mass-changing cross section $\sigma_{\Delta A}$ from the $\lambda_{^4He}$ for the remaining $^4$He ions behind the target. The $^3$He production cross section $\sigma_{^3He}$ can be calculated by subtracting $\sigma_{\Delta Z}$ from $\sigma_{\Delta A}$.

#### 3.4.3.5 Uncertainty Estimation

In cross section measurements as presented in this work, there are several experimental uncertainties to consider. On one hand, the limited beam time leads to a limited number of events $N$ that can be recorded which causes a statistical uncertainty $\Delta N_{stat} = \sqrt{N}$. On the other hand, the different ion species might not be perfectly identifiable because of overlapping clusters in the measured spectra. This causes a systematic uncertainty $\Delta N_{syst}$ which is not as straightforward to estimate as $\Delta N_{stat}$. Detailed remarks about this issue were given by Zeitlin et al. [143, 150] which were used as orientation for the uncertainty estimation performed here.
The robustness of the analysis code was checked by slightly varying the threshold values set by hand (T1 and T2, see Figure 3.8) which resulted in negligible deviations of the number of identified ions. As recommended by Zeitlin et al. [143], targets with different thicknesses were irradiated for each energy. When the number of the identified remaining primary ions decreases exponentially with the target thickness this can be taken as an additional confirmation that the analysis code works robust.
Instead of identifying the primary ions as usual by drawing cut contours into 2D-plots by hand, in this work the identification process was as much automatized as possible. The major fraction of the primary He ions could be clearly identified while about $10 - 20\%$ were overlapping with fragments in the measured 2D-plots (see Figure 3.8). The fraction of He ions lying in this overlap region $N_{overlap}$ was estimated by extrapolating the $\Delta$E

spectrum of the clear He events to the unclear events. Although this procedure is well justified from a physics point, the number of overlapping He ions obtained this way was accounted for with an additional uncertainty estimated by $\Delta N_{overlap} = \sqrt{N_{overlap}}$ which enhanced the uncertainty $\Delta N$ for the overall number of He events $N$ slightly.
The uncertainty of the charge-changing cross section $\sigma_{\Delta Z}$ was then estimated by variation of the number of He ions identified behind the thickest target in the limits of the uncertainty intervals $\Delta N$ and recalculation of the cross sections from these varied attenuation values. The identified He ions were separated into $^3$He and $^4$He by a fit method which also involved some uncertainty. Thus for the calculated mass-changing cross section $\sigma_{\Delta A}$ an additional uncertainty of 10% for the subtracted $^3$He fraction was estimated. The uncertainty of the $^3$He production cross section $\Delta\sigma_{^3He}$ was obtained by adding up $\Delta\sigma_{\Delta Z}$ and $\Delta\sigma_{\Delta A}$. The uncertainty intervals calculated for the cross section values in this way are believed to be a conservative estimate of the present experimental accuracy.
The energy of the primary $^4$He ions was reduced due to the energy loss in the targets which had the effect that the energy where the observed reactions took place was not sharply defined anymore. This energy range was kept small by using thin targets, but might still be non-negligible. It is accounted for by giving each cross section value for the mean energy assumed at the center of the thickest target with an uncertainty interval covering the energies before and behind that point. The energy loss within the nozzle, the air gap, the start detector and the targets was calculated with the FLUKA code.
The graphite targets have been produced at the GSI target laboratory from first choice graphite (SGL Carbon R 6550) with high precision (variation of the thickness over the target area $< 1\%$). The $CH_2$, Si and $SiO_2$ targets were ordered from external suppliers but had a similar precision. Therefore, the uncertainties associated with the dimensions and the density of the target material were considered to be small against the other sources of uncertainty and were neglected in this work.

## 3.5 Experimental Setup II: Target Fragmentation

The PET isotope production experiments described in the following were conducted at MIT, Marburg. Cross sections for the production of $^{10}$C, $^{11}$C and $^{15}$O target fragments by protons and $^{12}$C ions on C and O targets were measured with a detector system monitoring the induced $\beta^+$ activity after irradiation with a short proton or ion pulse. The description of the method and the results of these experiments are published in [151].

### 3.5.1 The Measurement Concept

The method for the measurement of PET isotope production presented in this thesis is conducted in the several steps described in the following: the experimental setup, consisting of three scintillators and a coincidence unit is positioned at the beamline and aligned according to the laser positioning system. The next step is a calibration measurement using a $^{22}$Na point source with known activity positioned at the center of the detection system guided by the positioning lasers. To be able to calculate the detection efficiency properly, the beamspot has to be characterized before the actual activation measurement can be performed. For this purpose, a Gafchromic EBT3 film is positioned in the target

holder and the laser positions are marked on the film before it is irradiated by a short pulse of protons or ions with the same beam settings used for the activation measurement, afterwards. Finally, the irradiated film is exchanged with the target, the data acquisition system is turned on and the target is irradiated. The induced $\beta^+$ activity can then be monitored as long as necessary (typically $15 - 30$ min depending on the isotopes of interest) and subsequently the next measurement is performed.

### 3.5.2 Experimental Setup

A schematic of the experimental setup is shown in Figure 3.10. Three $BaF_2$ scintillators (crystal dimensions: $3.5 \times 3.5 \times 7$ cm$^3$) with a thin wrapping coupled to a Hamamatsu R1668 photomultiplier are arranged around a thin graphite or BeO target tilted by 45° with respect to the beam axis. The $BaF_2$ scintillators are positioned at a distance of 5 cm from the target center. Two of them (#1 and #2) are arranged at 180° to measure the coincidence rate of the 511 keV annihilation photons following the $\beta^+$ decays and a third one (#3) is arranged at 90° to measure the random coincidence rate. The targets and films are positioned in a 3D-printed holder with a modular setup and can easily be exchanged without affecting the detector setup.

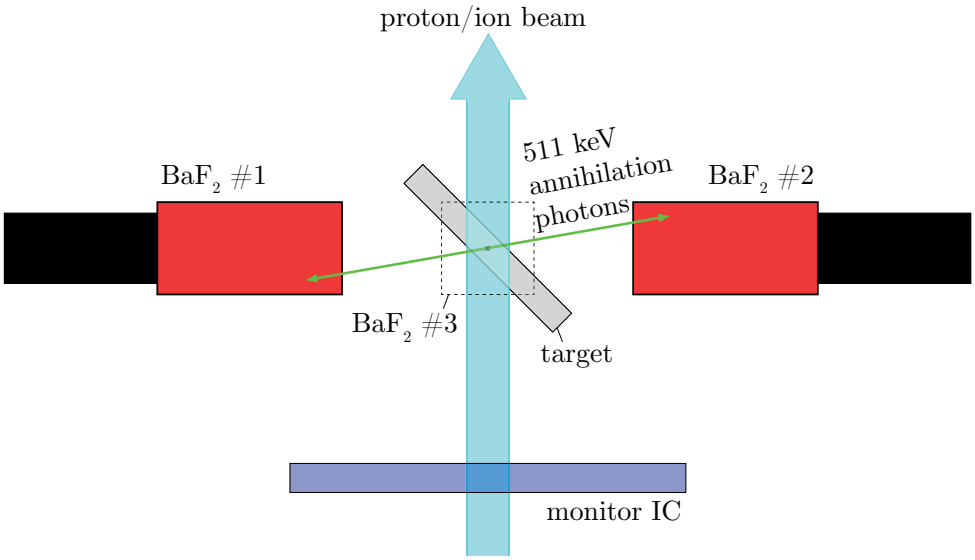


**Figure 3.10:** Schematic of the experimental setup for measuring production cross sections for $^{10}$C, $^{11}$C and $^{15}$O target fragments generated by high energy protons and $^{12}$C ions on graphite and BeO targets. The induced activity is monitored by a set of three $BaF_2$ scintillators (two visible in the schematic and the third in the plane perpendicular to #1 and #2) and the number of incident protons/ions is measured by the monitor ionization chamber (IC) within the beam nozzle.

### 3.5.3 Beam Application

The irradiations were performed as treatment plans with a single beam spot. The raster scanning control system monitored the irradiation and the number of incident particles

measured by the monitor ionization chamber within the nozzle was documented in the machine records. All irradiations were done using the beam line settings for the smallest focus (FWHM at the isocenter: $8.1 - 30.5$ mm for protons and $3.4 - 9.3$ mm for $^{12}$C ions) and at the highest intensity that can be extracted from the synchrotron ($1.5 \cdot 10^9$ protons/s and $6.5 \cdot 10^7$ $^{12}$C ions/s). The beam pulses had a duration of $\sim$ 1.3 s for protons and $\sim 1.0 - 2.5$ s for $^{12}$C ions. These short pulse durations were chosen to ensure that the time of isotope production was well defined and small against the decay times of the produced isotopes. The number of particles per measurement were $1.9 \cdot 10^9$ for protons and between $6.5 \cdot 10^7$ and $1.9 \cdot 10^8$ for $^{12}$C ions.

### 3.5.4 Coincidence Trigger and Data Acquisition

The scintillator signals were split by an active splitter specially designed for the fast rise time of $BaF_2$ pulses - one branch of the split signals was used to generate the trigger and the other was connected to the Tektronix DSA 72004C oscilloscope for data acquisition.

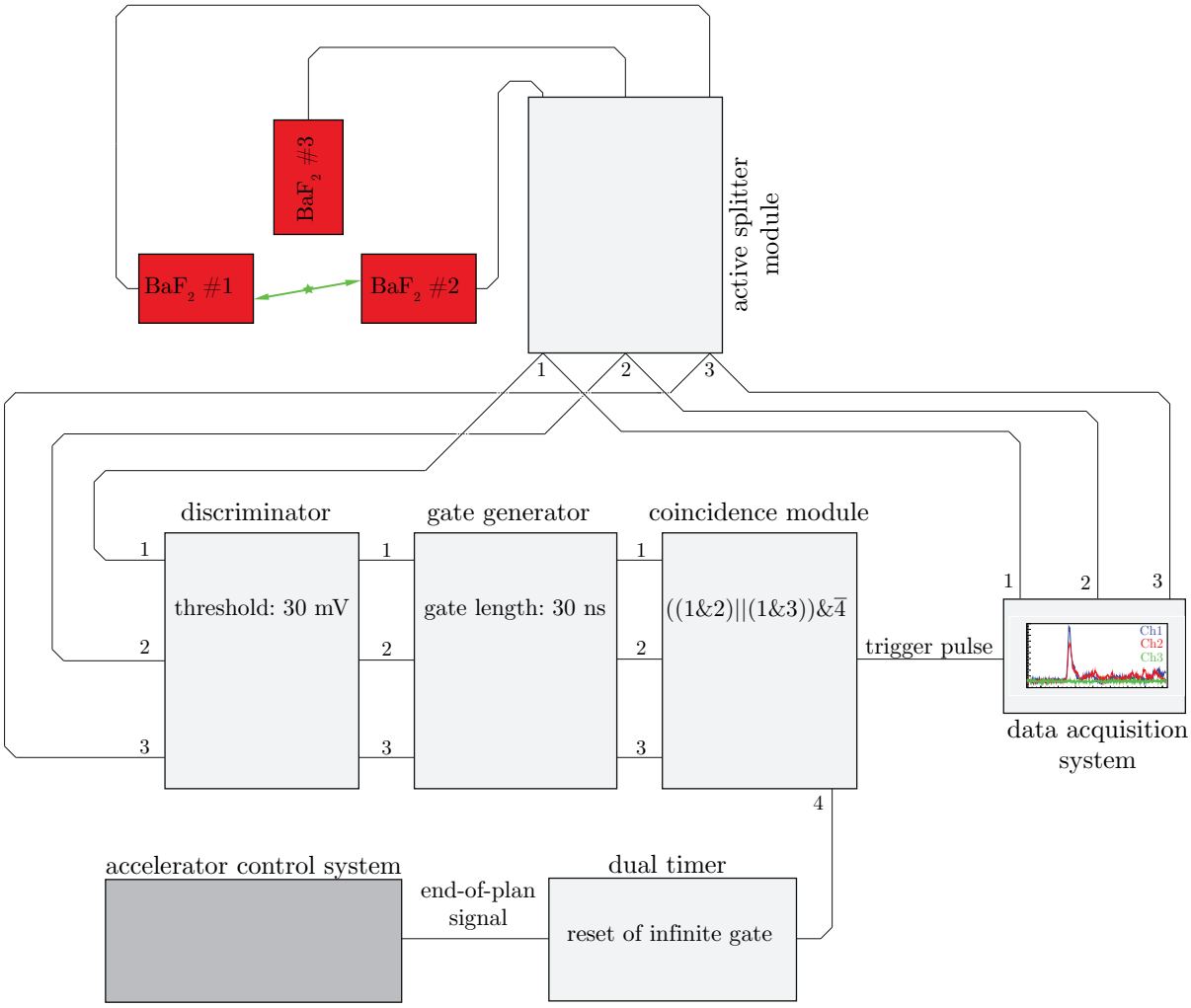


**Figure 3.11:** Flow chart of the trigger logic set up for the activation experiments performed at MIT.

The trigger unit was built from a set of NIM modules (discriminator, gate generator, coincidence module, dual timer) and generated a trigger signal for coincident signals either from detector #1 and #2 (180°) or from detector #1 and #3 (90°). The coincidence window was adjusted to 30 ns, which provided a good noise suppression for the 180° scintillator pair. However, there was still the possibility to measure random coincidences caused by two independent $\beta^+$ decays that occur both within the coincidence window. This random coincidence rate was monitored by the 90° scintillator pair. A flow chart of the coincidence trigger logic is shown in Figure 3.11. Before the experiment, the dual timer is set to give out an infinite gate. This gate is reset by the end-of-plan signal from the accelerator control system and afterwards trigger pulses are generated for coincident signals from either detector #1 and #2 or detector #1 and #3.

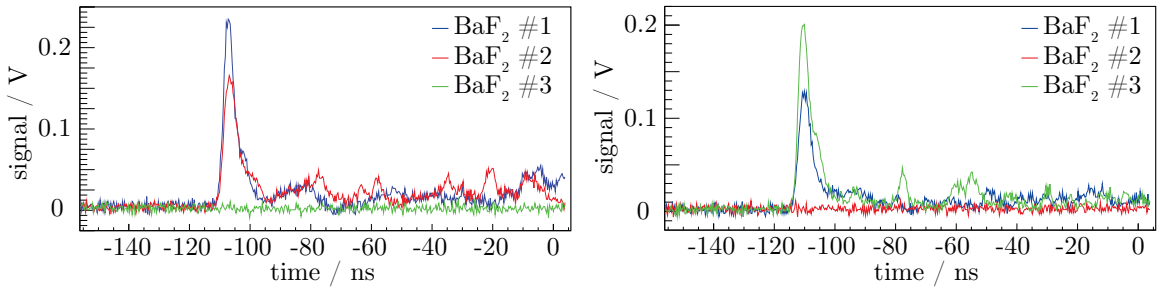


**Figure 3.12:** Waveforms for the three scintillator channels for two example events. The left plot shows a 180° coincidence (#1 and #2) and the right plot shows a 90° coincidence (#1 and #3).

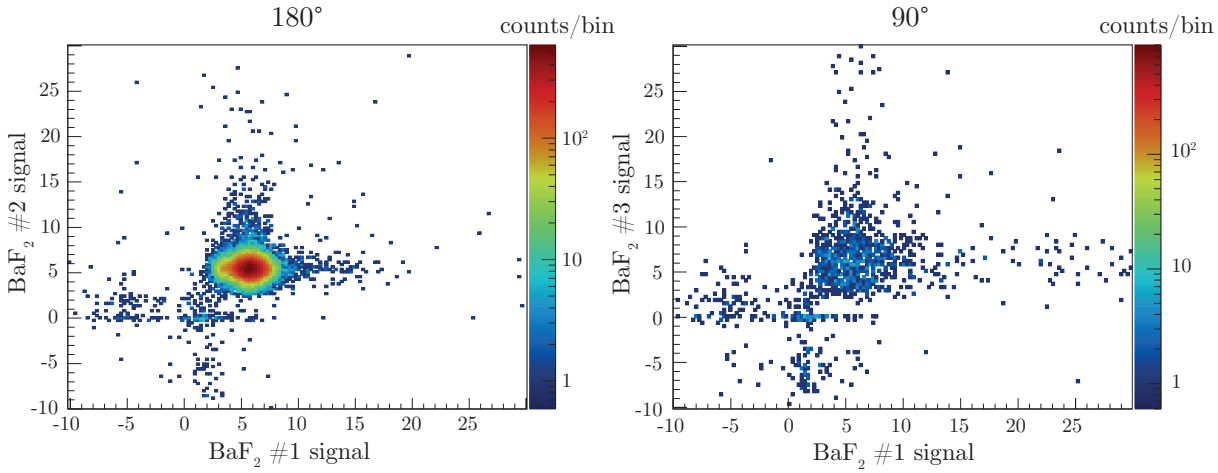


**Figure 3.13:** Energy spectra of the events detected by the 180° detector pair (#1 and #2) and by the 90° detector pair (#1 and #3) for a measurement of the activity induced by 220 MeV protons in a graphite target.

Figure 3.12 shows the waveforms of the three scintillator channels for two examples (a 180° coincidence and a 90° coincidence). Figure 3.13 shows the energy spectra of the events detected by the 180° detector pair (#1 and #2) and by the 90° detector pair (#1 and #3). In an offline analysis the 511 keV peaks were separated by applying a cut on

these energy spectra. Subtracting the 90° coincidence rate as a function of time from the 180° rate gives the *true* 180° coincidence rate as shown in Figure 3.14. This example shows that the random coincidence rate strongly depends on the present activity. In the time shortly after the irradiation, when the activity is at its maximum, random coincidences contribute more than 30% to the total coincidences measured at 180°. However, as the activity decreases, after $\sim$ 2 min the contribution of random coincidences to the total coincidence rate subsides significantly.

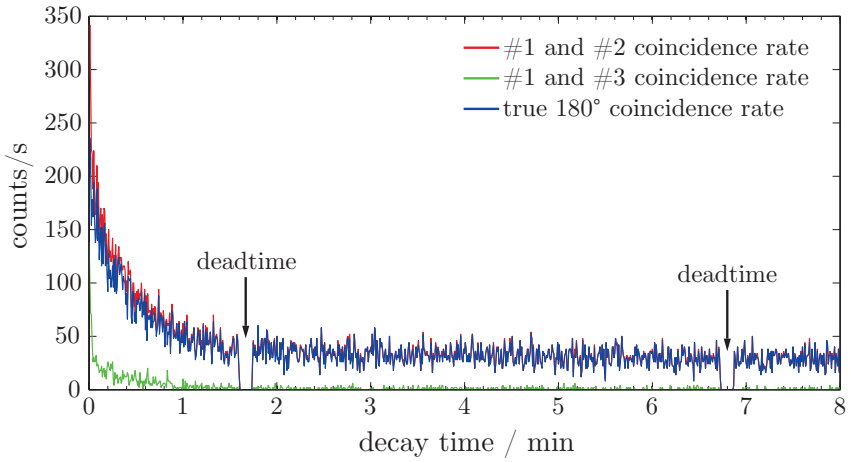


**Figure 3.14:** Decay curve of the $\beta^+$ activity induced by a pulse of 220 MeV protons in a graphite target. Two different isotopes ($^{10}$C and $^{11}$C) contribute to the total activity. In the first two minutes after proton irradiation the $\beta^+$ activity decreases fast because it is dominated by the $^{10}$C decays (half life: 19.29 s) and afterwards only the decays of the remaining $^{11}$C (half life: 20.334 min) are detected. The arrows mark the deadtimes of the data acquisition system due to the data storage on the hard drive of the oscilloscope. The red and green lines show the coincidence rates measured by scintillator #1 and #2 or #1 and #3, respectively. The blue line shows the true 180° coincidence rate obtained by subtracting the green curve from the red curve.

The signals of the three scintillators were recorded as waveforms (sample rate 3.1 GS/s) by an oscilloscope triggered by the coincidence unit. The oscilloscope can store data in its RAM with low deadtime between consecutive events, but it needs to save the stored data on a hard drive every few 1000 events (see Section 3.1). This causes short gaps in the measured decay curves every few minutes.
In order to suppress the measurement of prompt gamma photons which are produced during the irradiation, the end-of-plan signal from the accelerator control system was used to start the data acquisition immediately after the end of the spill (the trigger pulse is created 120 ms after the end of beam extraction). Furthermore, the end-of-plan signal was used to precisely determine the time point when the beam pulse ended.

### 3.5.5 Targets

Two different target materials were irradiated in the activation experiments. To obtain the production cross sections for the isotopes $^{10}$C and $^{11}$C on carbon, graphite targets (SGL

Carbon R 6550, density: 1.83 g/cm$^3$) with thicknesses of 5 mm and 10 mm (depending on the beam energy) and lateral dimensions of $80 \times 80$ mm$^2$ were irradiated with protons and $^{12}$C ions. To obtain the production cross sections for $^{15}$O on oxygen, BeO targets (Materion Thermalox 995, density: 2.85 g/cm$^3$) with a thickness of 3.9 mm and lateral dimensions of $114 \times 114$ mm$^2$ were used. For the measurements presented in this work (production of positron emitters) BeO acts as a pure oxygen target because the Be does not fragment into $\beta^+$-isotopes (as discussed by Tobias et al. [152]) and therefore does not contribute to the measured activity. To enhance the efficiency of the detection system, the targets were tilted by 45° with respect to the beam axis (see Figure 3.10). The local roughness at the center of the targets (uncertainty of the thickness) was $< 1\%$.

### 3.5.6 Beamspot Characterization

The calculation of the detection efficiency (as described in the Section 3.5.7) relies on the knowledge of the spatial distribution of the induced $\beta^+$-radioactivity within the target relative to the detectors.

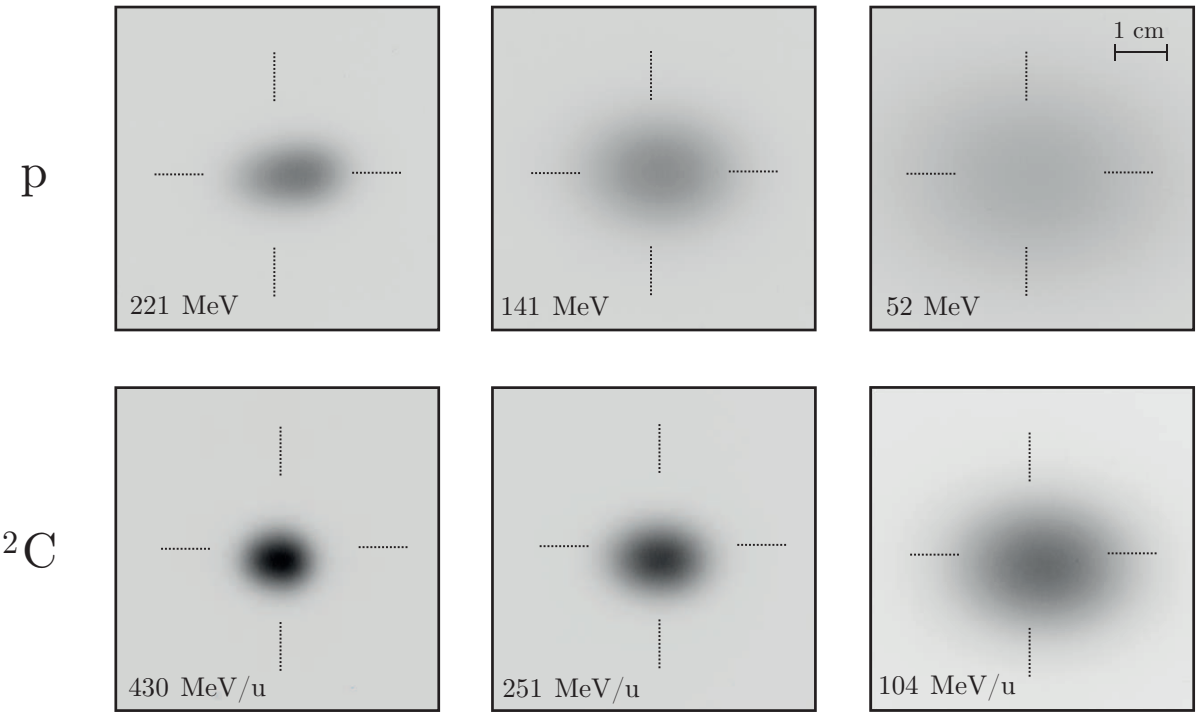


**Figure 3.15:** Proton and $^{12}$C ion beamspots at different energies at the target position (108 cm from the nozzle for $^{12}$C ions and 50 cm for protons) measured with EBT3 films tilted by 45° like the targets. The dotted lines correspond to the positioning lasers in the treatment room which were used to align the experimental setup.

To estimate the activity distribution within the target for each individual species-energy-target combination, fluence measurements using EBT3 films located exactly at the target position (also with the 45° tilt) were performed in advance before all target irradiations. From these films measured vertical and horizontal fluence profiles were obtained and fitted with single Gaussian functions to be used for the calculation of the efficiency. Also shifts of the beamspots relative to the scintillator setup could be detected and taken

into account for the efficiency calculation. The parameters characterizing a beamspot are called $\text{FWHM}_{\text{horizontal}}$, $\text{FWHM}_{\text{vertical}}$, $\text{shift}_{\text{horizontal}}$ and $\text{shift}_{\text{vertical}}$.
To convert the gray values of the EBT3 films into fluence values, a calibration function was determined for both protons and carbon ions. $^{12}$C ion measurements were restricted to the isocenter (distance from isocenter to nozzle: $\sim$ 108 cm) where the beamspot sizes are daily checked and documented in the QA protocols. For the proton irradiations the setup was moved to a distance of 50 cm from the nozzle. This closer distance was of advantage especially for the low proton energies because proton beams scatter much stronger within the nozzle than $^{12}$C ion beams, which leads to relatively large proton beamspots at the isocenter (see Figure 2.7).
Figure 3.15 shows examples of films irradiated with protons and $^{12}$C ions. As expected the $^{12}$C ion beamspots are sharper compared to the proton beamspots. The beam spot sizes get larger for lower energies due to the increased lateral scattering within the nozzle. Slight shifts of the beamspots relative to the positioning lasers can be observed depending on the energy. The film response to the $^{12}$C ions is stronger than to protons due to their higher LET. The beamspots appear stretched in horizontal direction because the films were irradiated with the 45° tilt like the targets.

### 3.5.7 Efficiency Calculation

For the calculation of the production cross sections for the different isotopes, their absolute activities produced by the proton or ion pulses within the targets had to be determined. For such an absolute measurement the efficiency of the detection system (count rate per activity) must be known. Because the beamspot sizes and therefore the spatial distribution of the induced radioactivity varied considerably among the different beams used (see Figure 3.15), the efficiency had to be determined for each measurement separately.
To calculate the detection efficiency for each individual measurement, a numerical algorithm was developed which takes all relevant effects into account: the detection efficiency depends (a) on the spatial distribution of the $\beta^+$-activity relative to the detector setup (for activities located at the center the efficiency is maximum and drops at the sides), (b) on the amount of material between the activity and the detectors (causing attenuation of the 511 keV annihilation photons) and (c) on the distance between the activity and the target edge (positrons may escape from the target and annihilate outside the detection zone).
The efficiency algorithm requires the following input parameters: the first parameter is the maximum efficiency of the detection system determined with a $^{22}$Na point source with known activity positioned at the center of the detection zone. This calibration was repeated each time the experiment was re-built to take account of e.g. small variations in the electronic thresholds of the coincidence unit or a slight geometrical misalignment of the detectors. Secondly, the beamspot parameters ($\text{FWHM}_{\text{horizontal}}$, $\text{FWHM}_{\text{vertical}}$, $\text{shift}_{\text{horizontal}}$, $\text{shift}_{\text{vertical}}$) obtained from the film measurement have to be taken into consideration to model the activity distribution in the target. Lastly, the target thickness and material have to be specified to enable an accurate estimation of the photon (self-) absorption and the fraction of positrons that escape the target without annihilation.
Based on the beamspot parameters, the algorithm models the spatial distribution of the $\beta^+$-radioactivity within the target divided into voxels ($80 \times 80$ voxels lateral and 100 voxels in depth) considering that the induced activity is proportional to the fluence. In

the next step, the activity in each voxel is weighted by the efficiency of the corresponding voxel position divided by the total activity. To be able to calculate the efficiency for every position, a high resolution efficiency map was recorded in advance by moving a $^{22}$Na point source in 1 mm steps through the detection zone using a mechanical positioning device (shown in Figure 3.16).

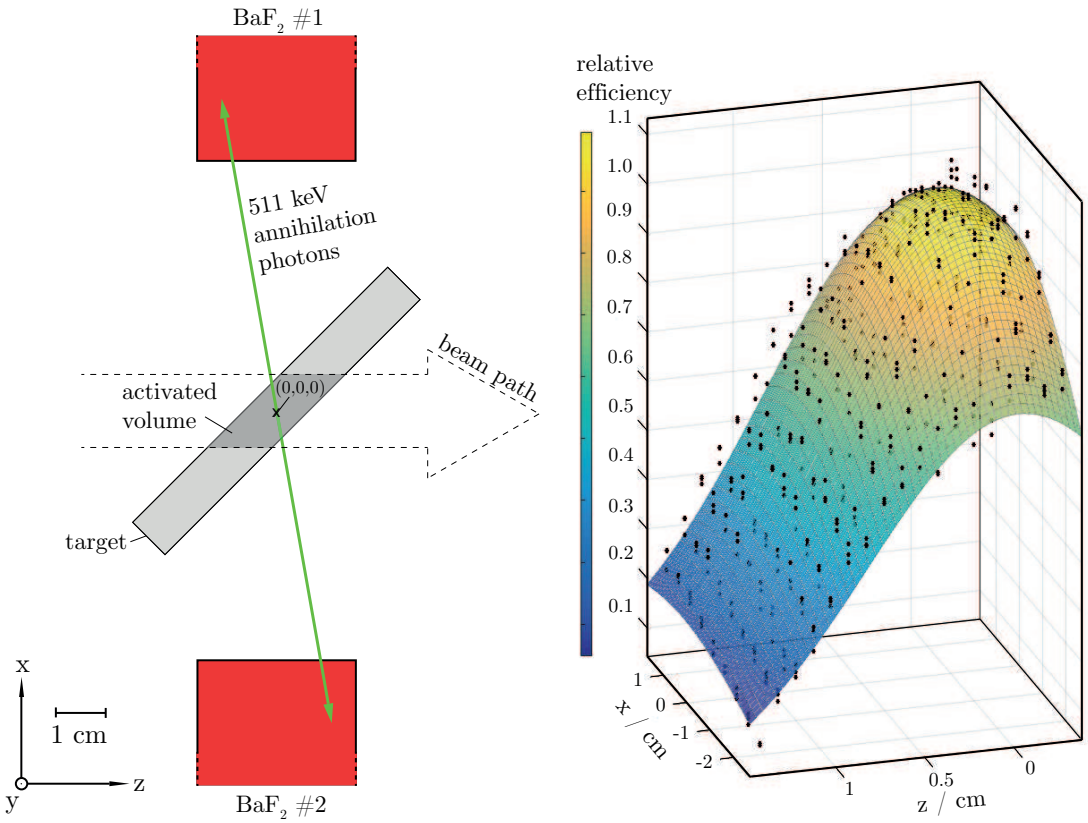


**Figure 3.16:** Schematic illustration of the influence of the spatial distribution of the produced activity on the detection efficiency (left panel). This dependency was characterized using a $^{22}$Na point source moved through the detection zone in x- and z-direction (right panel). The dots mark the measured points and the surface represents a Gaussian fit in x- and z-direction to be used by the efficiency algorithm. Due to symmetry reasons, the drop of the efficiency in y-direction can be considered equal to the one in z-direction.

This efficiency map is normalized to unity at the detection zone center and can be converted into absolute values by applying the calibration factor measured with the $^{22}$Na source right before the measurements (see above). The reduction of the efficiency due to the absorption of one of the 511 keV photons within the target or the detector wrapping and due to positrons escaping from the target is taken into account for each individual voxel by using the photon attenuation coefficients from the NIST XCOM database [153] and by applying a positron loss model based on FLUKA simulations considering published $^{11}$C and $^{15}$O positron spectra given by Eckerman et al. [154] and a $^{10}$C positron spectrum calculated according to a model given by Levin and Hoffman [155]. Finally, the resulting detection efficiency, which relates the measured coincidence rate with the activity for the particular measurement (true 180° coincidences per second per Becquerel) is obtained by

averaging the activity-weighted efficiency over all voxels.
Due to the target thicknesses of 3.8 mm for BeO or 5 and 10 mm for graphite, the efficiency reduction due to positron loss was only in the order of $4-8\%$ since they could only escape from the last $1-2$ mm of the graphite targets (depending on the isotope) and from the last mm of the BeO targets. The calculated efficiencies varied between 0.30% and 0.65% for the proton measurements and between 0.41% and 0.73% for the carbon ion measurements. The generally very low efficiencies are due to the small solid angle covered by the scintillators while the differences between the measurements at different energies are mainly due to the varying beamspot sizes. The beamspot sizes are also the reason for the higher efficiencies for the $^{12}$C ion measurements compared to the proton measurements because of their sharper beamspots (see Figure 3.15).

### 3.5.8 Data Analysis

#### 3.5.8.1 Cross Section Calculation

The measured 180° coincidence count rate as a function of time $A(t)$ can be fitted by a composite exponential decay function [156] (one exponential function for each produced isotope) according to Equation 3.6

$$A(t) = A_0^{X_1} \cdot 0.5^{\frac{t}{T_{1/2}^{X_1}}} + A_0^{X_2} \cdot 0.5^{\frac{t}{T_{1/2}^{X_2}}} + ... \tag{3.6}$$

where $A_0^{X_i}$ are the initial count rates and $T_{1/2}^{X_i}$ are the half lives of the isotopes $X_i$.
Using the initial count rates obtained from fitting the measured decay curve, the production cross sections $\sigma_{X_i}$ can be calculated according to Equation 3.7

$$\sigma^{X_i} = \frac{\frac{A_0^{X_i}}{\epsilon}}{z \cdot \frac{n}{V} \cdot N \cdot \lambda^{X_i}} \tag{3.7}$$

where $\epsilon$ is the detection efficiency, $z$ is the target thickness in beam direction, $n/V$ is the number of target nuclei per volume, $N$ is the number of particles in the beam pulse and $\lambda^{X_i}$ is the decay constant of isotope $X_i$.
A fitting function according to Equation 3.6 assumes that the irradiation time $\Delta t$ is much shorter than the half lives $T_{1/2}$ of the isotopes produced because the competition between build-up and radioactive decay during the irradiation is not taken into account. For isotopes where the duration of the irradiation is non-negligible compared with the half life - in this work this was only the case for $^{10}$C - the term for a single isotope can be split into multiple terms having different zero time points. For the fitting model in this work the time point of the $^{10}$C production was split into three according to Equation 3.8.

$$A^{^{10}C}(t) = \frac{A_0^{^{10}C}}{3} \cdot 0.5^{\frac{t-\Delta t/3}{T_{1/2}^{^{10}C}}} + \frac{A_0^{^{10}C}}{3} \cdot 0.5^{\frac{t}{T_{1/2}^{^{10}C}}} + \frac{A_0^{^{10}C}}{3} \cdot 0.5^{\frac{t+\Delta t/3}{T_{1/2}^{^{10}C}}} \tag{3.8}$$

With this approach, the temporal course of the activity production can be taken into account in good approximation.

#### 3.5.8.2 Uncertainty Estimation

The energy loss within the targets smeared the energy where the observed reactions took place (see also Section 3.4.3.5). This energy interval was kept small by using thin targets but is non-negligible, especially for the low energy measurement points. It is accounted for by giving each cross section value for the mean energy at the target center with an uncertainty interval covering the energies before and after. These energy uncertainty intervals were calculated by radiation transport calculations through the different targets using the FLUKA code.
Besides the energy uncertainty, there are also different effects to consider that influence the uncertainty of the cross section value: the activity of the $^{22}$Na source used for calibration of the detection system has a manufacturing uncertainty of 3%. The number of primary ions impinging on the target was determined by the monitor ionization chamber in the nozzle. Its calibration by means of an absorbed dose to water measurement under dosimetric reference conditions has an uncertainty which was assumed to be 4% (where 2% results from the uncertainty of the beam quality correction factor $k_Q$ used for absorbed dose to water determination and another 2% from the beam model which was used to convert the measured absorbed dose to water into fluence). The algorithm used to calculate the detection efficiency considers all relevant effects but uses some simplified models (e.g. the single Gaussian beam profile which does not consider the beam halo), therefore the calculated efficiency is not free of uncertainty either. This was estimated to be 3% based on variations of the input parameters within reasonable limits. Following the rules of error propagation, these individual uncertainties add up to an estimated total systematic cross section uncertainty of 10%. Lastly, the produced initial activities are estimated by fitting the measured decay curve with a composite exponential decay function, whose accuracy is mainly affected by the amount of produced activity and the resulting counting statistics. This uncertainty was estimated by the fitter individually for each measurement and added to the generalized systematic uncertainty of 10% given above. Uncertainties associated with the targets (homogeneity or misplacement) are small against the above mentioned sources of uncertainty and are therefore neglected.

## 3.6 Radiation Transport Calculations

The experimental cross section data were applied for calculation of depth dose profiles by $^4$He ions and $\beta^+$-activity profiles by protons. These data could then be compared to measured data from the literature.

### 3.6.1 Monte Carlo Codes Geant4 and FLUKA

In addition to the experiments also radiation transport calculations using the Monte Carlo codes Geant4 [8] (TOPAS toolkit [157]) and FLUKA [9, 10, 11] were performed. Both codes were originally developed for high-energy physics applications but have been becoming also very popular in the field of medical physics and particle therapy. The particle transport techniques of FLUKA and Geant4 are quite comparable. However, a conceptual difference is that FLUKA is a fully-integrated Monte Carlo code where the source code is

not available and in most cases the user can not choose between different physics models but only increase the complexity and accuracy of the embedded models in different steps, while Geant4 is a Monte Carlo simulation toolkit where the user can change the source code and has to choose between many different models for each interaction type. This makes Geant4 more flexible compared to FLUKA but on the other hand FLUKA is very robust, well-tested and its simulations are more reproducible. Especially the latter is an important requirement for clinical applications.
Both codes are capable of transporting various kinds of particles including photons, electrons, positrons, neutrons, protons and heavy ions. The energy loss of charged particles is treated in a condensed history approach, which means that the multiple electronic collisions are summarized in a continuous energy loss (see Section 2.3.1) and only delta electrons above a certain threshold defined by the user are explicitly produced and transported. Single Coulomb scattering events are condensed by a multiple scattering algorithm.
For nuclear reactions FLUKA uses a total reaction cross section parametrization which is an empirically modified version of the Tripathi formula [129]. This parametrization is fixed and can not be changed by the user (only from developer side). After a nuclear reaction has been induced with a certain probability according to the total reaction cross section model the reaction is simulated on a microscopic basis using appropriate nuclear event generators. After the reaction, the de-excitation and coalescence of the residual nuclei and nucleons are simulated by an evaporation and coalescence module to obtain the final state. The ejectiles in the final state are then transported further. In FLUKA, hadron-nucleus reactions are simulated with the PEANUT model [158]. Nucleus-nucleus reactions at energies above 125 MeV/u are treated by a modified version [129] of the original relativistic quantum molecular dynamics (RQMD) model [159] and for reactions at energies below 125 MeV/u an approach based on the Boltzmann master equation (BME) is used [160]. The energy at which the code switches between BME and RQMD lies within the therapeutic energy range. This means that both event generators have to be optimized for particle therapy applications of FLUKA and the transition between the two models should be as smooth as possible.
In Geant4 the user can choose between different models and event generators [161]. For the total reaction cross section parametrizations by Sihver [162], Kox and Shen [123, 130] and Tripathi [127, 128] are implemented. The available event generators for nucleus-nucleus reactions are the binary intranuclear cascade model (BIC), the Liège Intranuclear Cascade Model (INCL) and the Quantum Molecular Dynamics Model (QMD).

### 3.6.2 Treatment Planning System TRiP98

For calculation of $^{4}$He absorbed dose and RBE profiles the research treatment planning system TRiP98 was used. It was the first treatment planning system that was capable of optimizing biologically equivalent dose distributions, originally developed for the $^{12}$C ion therapy pilot project at GSI. TRiP98 calculates dose distributions based on a pencil beam algorithm as described in more detail in Section 2.5.1. The basic concept of physical dose calculation can be found in the publication by Krämer et al. [35] while the radiobiological methods to optimize RBE-weighted dose distributions on basis of the LEM (Section 2.4.1) are described in a separate article by Krämer and Scholz [36].

### 3.6.3 Depth Dose Profiles by $^4$He Ions in Water

Depth dose profiles of $^4$He ions in water were studied using the Monte Carlo codes TOPAS/Geant4 and FLUKA as well as the treatment planning system TRiP98. The calculated depth dose profiles could be compared with dose measurements performed recently at HIT [4, 113] and old data from Berkeley [163].
For the TOPAS/Geant4 and TRiP98 calculations in this thesis, the parametrization of the reaction cross section by Tripathi was used (in its original and modified form as shown in Section 4.1.3). In Geant4 the QMD event generator was used for simulating fragment production in nucleus-nucleus reactions since it is the recommended model for $^{12}$C ion therapy simulations [164]. By doing test simulations with the other available models (BIC, INCL) it turned out that the choice of the nuclear event generator has only negligible effects on the prediction of $^4$He depth dose profiles. In TRiP98 the fragment production cross sections described by Krämer et al. [4] were used.
The FLUKA simulations of $^4$He depth dose profiles were performed by the FLUKA developers using the development version 2017.0 (containing an old parametrization of the total reaction cross section) and 2018.0 (containing an optimized parametrization).
The measured depth dose profiles which were compared with the Monte Carlo predictions have been obtained by large area parallel-plate ionization chambers and adjustable water columns. For comparison with the data acquired at HIT the lateral integration radius was set to 4.08 cm in the simulations corresponding to the PTW Peakfinder ionization chamber which was used for the measurements [113]. The initial energy spread of the $^4$He ions was assumed to be Gaussian with $\sigma$ values between 0.2% for the highest energy and 1% for the lowest energy which are realistic values for the HIT synchrotron [97]. For comparison with the Berkeley data the lateral integration radius was set to 10 cm (where practically no particles can escape from the sides) because no details on the ionization chambers were given in the original publication and the initial energy spread was assumed to be 0.2%.

### 3.6.4 RBE Profiles by $^4$He Ions

In this work TRiP98 was used for calculation of RBE profiles for $^4$He ions using the original and the optimized Tripathi parametrization of the total reaction cross section $\sigma_R$ to study the impact of $^4$He fragmentation models on a clinically relevant radiobiological quantity. LEM IV tables for two different model tissues, one with an $\alpha/\beta$-ratio of 10 Gy representing tumor tissue and the other with a lower $\alpha/\beta$-ratio of 2 Gy that should mimic normal tissue (the same model tissues as described in Section 2.4.2 and also used by Grün et al. [91]).

### 3.6.5 PET Isotope Production by Protons in a Tissue Phantom

The measured production cross sections for the main PT-PET isotopes $^{11}$C and $^{15}$O by protons on C and O targets were validated against published $\beta^+$-activity profiles measured in a tissue equivalent gel phantom with a clinical PET scanner after proton irradiation [122]. For this purpose, look-up tables with the $^{12}$C(p, pn)$^{11}$C and $^{16}$O(p, pn)$^{15}$O excitation functions representing the measured cross sections presented in Section 4.2.2 were created

and convoluted with the proton spectrum to obtain the produced $\beta^+$-activity (the method and also how to model the temporal progress of the activity has been described in detail by Parodi et al. [75] and Bauer et al. [77]).
The proton spectrum as a function of depth was obtained from simulations with the Monte Carlo toolkit TOPAS/Geant4 [8, 157]. The proton source spectrum for the simulation was optimized to reproduce the depth dose profile published in the article of Espana et al. [122]. The elemental composition of the phantom material was given as 9.6% H, 14.6% C, 1.46% N and 73.8% O and the density was given as 1.13 g/cm$^3$. Due to the high C and O content in the tissue equivalent gel, it is well suited to validate the production cross sections on both target materials. To take account of the PET scanner resolution the calculated activity profiles were convoluted with a Gaussian kernel with 7 mm FWHM, also given by Espana et al. [122]. The image acquisition protocols used in the experiment should mimic two different particle therapy PET methods: the 5 min protocol (5 min image acquisition started directly after the irradiation) corresponds to an in-room PET measurement, while the 30 min protocol (30 min image acquisition after a 15 min break) mimicks an offline PET measurement.
The reaction channels that had to be considered in the radiation transport calculation were $^{12}\mathrm{C}(\mathrm{p},\mathrm{pn})^{11}\mathrm{C}$ and $^{16}\mathrm{O}(\mathrm{p},\mathrm{pn})^{15}\mathrm{O}$ which were characterized in the present work, but also $^{16}\mathrm{O}(\mathrm{p},\mathrm{X})^{11}\mathrm{C}$ and $^{16}\mathrm{O}(\mathrm{p},\mathrm{X})^{13}\mathrm{N}$ which were not measured in the present experiments. The cross section tables for the latter two channels were taken from Bauer et al. [77]. Contributions of $^{10}\mathrm{C}$ can be neglected for the acquisition protocols used by Espana et al. [122] because also for the 5 min measurement they could not avoid a break of $\sim$ 1 min between irradiation stop and start of the PET imaging which is long enough for the majority of the $^{10}\mathrm{C}$ to decay.

# 4 Results and Discussion

## 4.1 Projectile Fragmentation Experiments

### 4.1.1 He and $^4$He Attenuation Curves

As an ion beam penetrates through material the number of remaining primary ions decreases with increasing depth due to nuclear reactions. The relative number of primary ions as a function of depth $N/N_0(z)$, called attenuation curve, is a typical observable to characterize the nuclear fragmentation characteristics of a given ion-target combination and to benchmark transport codes [66, 68].

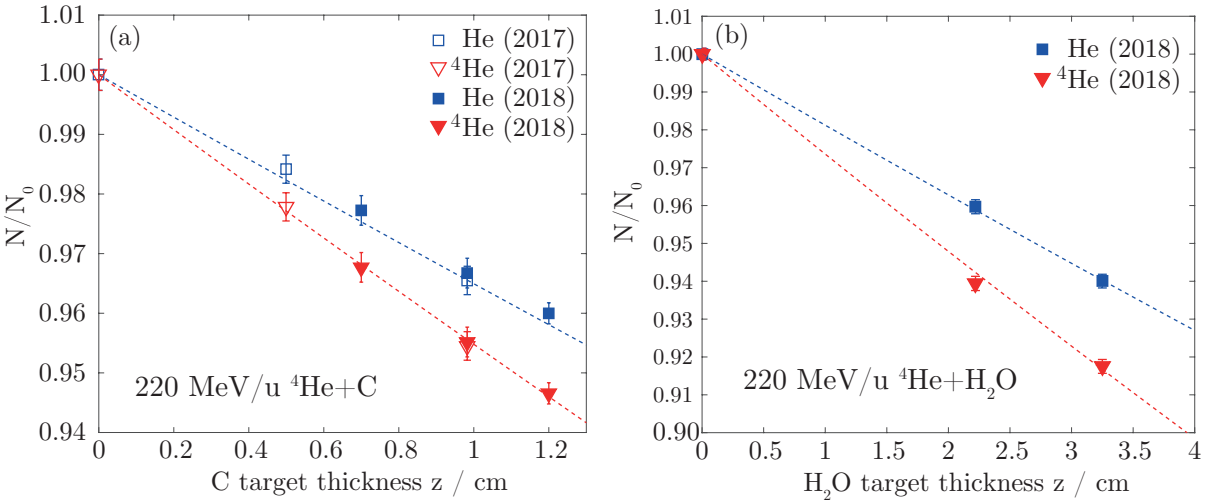


**Figure 4.1:** Attenuation curves measured for C (panel a) and $H_2O$ (panel b) targets for 220 MeV/u $^4$He ions. The dashed lines represent the corresponding fit functions according to Equation 3.4 to extract the charge- and mass-changing cross sections from the attenuation curves. In panel a the measured attenuation values for C targets from the 2017 experiment [146] and the 2018 experiment [147] are compared. The C curves are normalized to the no-target measurement, while the $H_2O$ curves are normalized to the measurements behind the empty flasks (see Section 3.4.1).

Two examples of $^4$He attenuation curves for C and $H_2O$ targets obtained by analysis of the recorded $\Delta$E-pulse-shape spectra behind different target thicknesses are shown in Figure 4.1. The number of transmitted He and $^4$He ions are normalized to the number obtained in the no-target measurement (attenuation in C) or in the measurement behind the empty flasks (attenuation in $H_2O$), respectively. The agreement of the attenuation data behind the C targets taken during the different experiments (2017 and 2018) proves the consistency of the two datasets. The charge- and mass-changing cross sections for each energy-target combination could be extracted from the measured attenuation curves

by exponential fits (Equation 2.7). The fit functions look almost linear because the thicknesses of the targets used were small against the mean free path of the ions.

### 4.1.2 Charge- and Mass-Changing Cross Sections for $^4$He Ions

The measured charge- and mass-changing cross sections for C, $CH_2$, Si, $SiO_2$ and $H_2O$ targets as well as the calculated cross sections for H and O targets are listed in Table 4.1. The (inclusive) $^3$He production cross section can be calculated by subtracting $\sigma_{\Delta Z}$ from $\sigma_{\Delta A}$ because fragmentation into $^3$He is the only mass-changing but non-charge-changing reaction channel that can occur for $^4$He projectiles.

**Table 4.1:** Measured mass- and charge-changing cross sections for $^4$He ions with different energies on different targets. The upper values were directly measured and the values for H and O were calculated from the upper values according to Equation 3.2 and Equation 3.3.

| target | method | kinetic energy / MeV/u | charge-changing cross section $\sigma_{\Delta Z}$ / mb | mass-changing cross section $\sigma_{\Delta A}$ / mb |
|---|---|---|---|---|
| C | measured | $74 \pm 4$ | $277 \pm 33$ | $602 \pm 66$ |
| C | measured | $83 \pm 6.5$ | $330 \pm 25$ | $548 \pm 47$ |
| C | measured | $125 \pm 5$ | $323 \pm 23$ | $497 \pm 40$ |
| C | measured | $176 \pm 4$ | $376 \pm 23$ | $500 \pm 35$ |
| C | measured | $216 \pm 4$ | $392 \pm 19$ | $520 \pm 32$ |
| $CH_2$ | measured | $71 \pm 8$ | $321 \pm 47$ | $875 \pm 103$ |
| $CH_2$ | measured | $119 \pm 10$ | $442 \pm 22$ | $731 \pm 51$ |
| $CH_2$ | measured | $215 \pm 5$ | $490 \pm 23$ | $729 \pm 47$ |
| Si | measured | $71 \pm 8$ | $304 \pm 44$ | $961 \pm 110$ |
| Si | measured | $119 \pm 10$ | $487 \pm 26$ | $816 \pm 59$ |
| Si | measured | $213 \pm 7$ | $620 \pm 26$ | $792 \pm 43$ |
| $SiO_2$ | measured | $71 \pm 8$ | $806 \pm 99$ | $2317 \pm 251$ |
| $SiO_2$ | measured | $119 \pm 10$ | $1240 \pm 58$ | $2042 \pm 139$ |
| $SiO_2$ | measured | $213 \pm 7$ | $1563 \pm 58$ | $1959 \pm 98$ |
| $H_2O$ | measured | $213 \pm 7$ | $568 \pm 35$ | $800 \pm 58$ |
| H | calculated | $71 \pm 8$ | $22^{+57}_{-22}$ | $137 \pm 69$ |
| H | calculated | $119 \pm 10$ | $60 \pm 31$ | $117 \pm 37$ |
| H | calculated | $215 \pm 5$ | $49 \pm 30$ | $104 \pm 35$ |
| O | calculated | $71 \pm 8$ | $251 \pm 108$ | $678 \pm 152$ |
| O | calculated | $119 \pm 10$ | $377 \pm 63$ | $613 \pm 88$ |
| O | calculated | $213 \pm 7$ | $472 \pm 64$ | $584 \pm 75$ |

In Figure 4.2 the charge- and mass-changing cross sections for the elemental targets C, O, Si and H as a function of kinetic energy obtained at the present experiment are shown together with the available data from the literature (C targets [165, 166, 167, 168, 169, 170, 171], O targets [165, 166, 171], Si targets [165, 166, 172], H targets [169, 173, 174, 175]).

The shown reference data include also a few charge-changing cross sections which are slightly lower than the corresponding mass-changing cross sections because the contribution of neutron-removal reactions is missing. For comparison the reaction cross section parametrizations by Tripathi et al. for $^4$He-nucleus [127] (panel a-c) and for $^4$He-$^1$H collisions [128] (panel d) are plotted. The target nuclei are called by their main isotope. This is done for simplicity, while in the analysis the natural isotopic composition of the targets was taken into account.

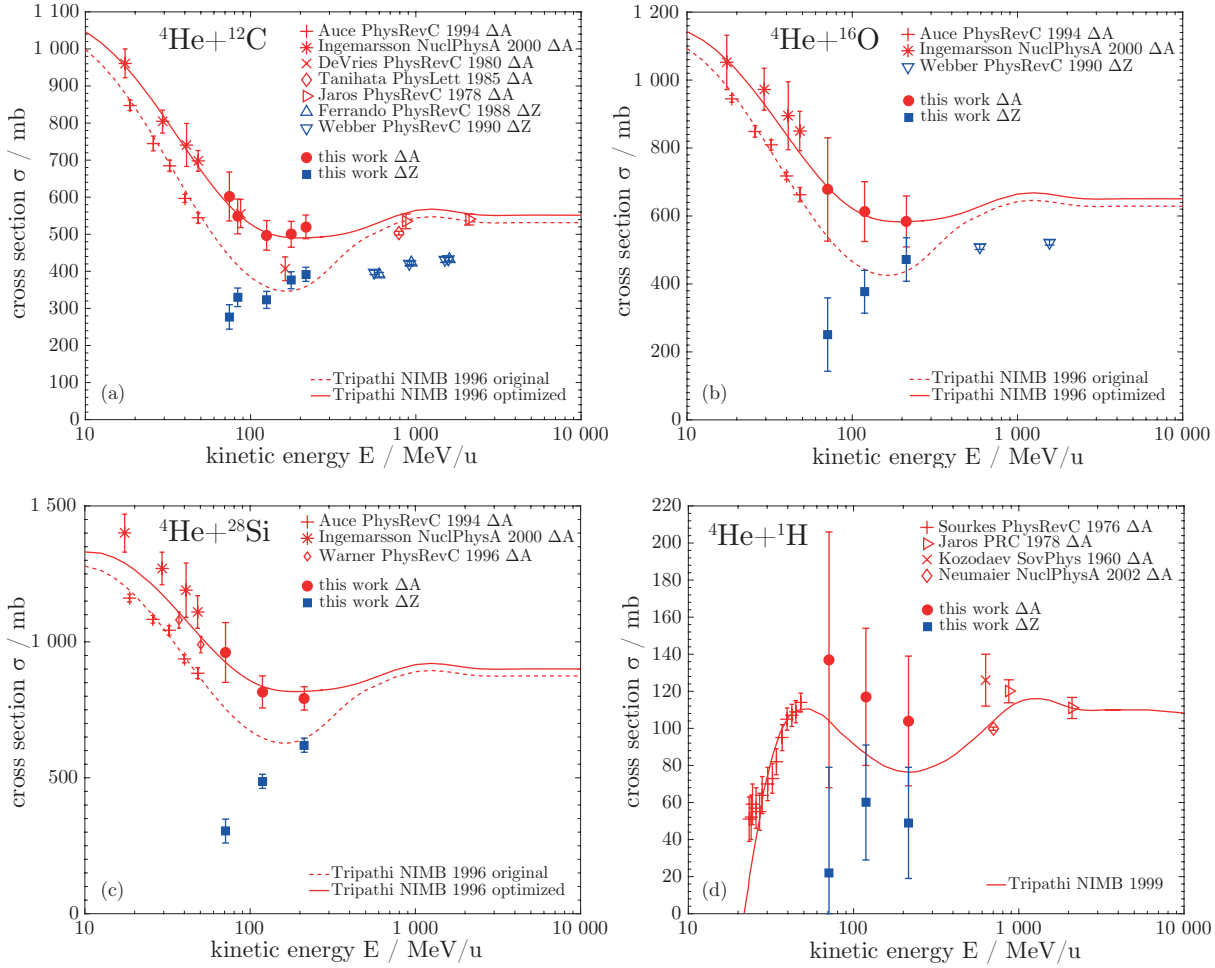


**Figure 4.2:** Measured charge- and mass-changing cross sections $\sigma_{\Delta Z}$ and $\sigma_{\Delta A}$ for $^4$He ions on different elemental targets (C, O, Si and H) compared with reference data from the literature ($\sigma_{\Delta A}$ and $\sigma_{\Delta Z}$) [165, 166, 167, 168, 169, 170, 171, 172, 173, 174, 175]. For the $^4$He-nucleus systems ($^4$He $+^{12}$ C, $^4$He $+^{16}$ O, $^4$He $+^{28}$ Si) the Tripathi parametrization for heavy-ion collisions [127] as well as a version optimized on basis of the new measured cross sections are shown. For the $^4$He $+^1$ H system the prediction of the Tripathi parametrization for light systems [128] is plotted.

The measured mass-changing cross sections obtained in the present experiments are in good agreement with the reference data from the literature. At the lower end of the investigated energy range (70 MeV/u) is a rather smooth transition from the present cross sections to the experimental data by Ingemarsson et al. [166] ($^4$He-nucleus systems, panel

a-c) and Sourkes et al. [173] ($^4$He-$^1$H system, panel d). The charge-changing cross sections at high energies reported by Ferrando et al. [170] and Webber et al. [171] (measured in inverse kinematics, by irradiating a $^4$He target with $^{12}$C and $^{16}$O beams) compare well with the $^4$He charge-changing cross sections obtained in the present experiment. It can be observed that towards lower energies the charge-changing cross sections drop down while the mass-changing cross sections increase which means that $^4$He fragmentation at low energies ($< 100$ MeV/u) is dominated by reactions that produce $^3$He.
The relative uncertainties of the H and O cross sections are considerably larger than those of the C and Si targets due to the propagation of the compound target cross section uncertainties into the errors of the calculated elemental cross sections. However, the reasonable accordance of the measured data with the literature data suggests that this approach provides a rather conservative estimate of the actual measurement uncertainty.
The total reaction cross section $\sigma_R$ for proton-nucleus and nucleus-nucleus systems follows the trend of the nucleon-nucleon total cross section as a function of energy due to the microscopic nature of these collisons [124, 167, 176]. The reaction cross section shows a maximum at a few 10 MeV/u and then drops down to a minimum lying at a few 100 MeV/u. As the pion production channels open, $\sigma_R$ rises again slightly before it finally stays constant towards higher energies. This general behavior of $\sigma_R$ is visible in the plotted experimental mass-changing cross sections for $^4$He ions and is well reflected by the parametrizations.
In Table 4.2 the charge- and mass-changing cross sections obtained for 213 MeV/u $^4$He ions on $H_2O$ targets by calculation (summation of the H and O cross sections obtained from measurements on C, $CH_2$, Si and $SiO_2$) and by a direct measurement (using the $H_2O$ filled flasks) are compared.

**Table 4.2:** $^4$He charge- and mass-changing cross sections measured on $H_2O$ targets compared with those calculated from the H and O cross sections obtained from the C, $CH_2$, Si and $SiO_2$ target measurements (see text). For further comparison, the mass-changing cross section estimated by Rovituso et al. [71] from a thick target measurement is shown.

| method | kinetic Energy / MeV/u | charge-changing cross section $\sigma_{\Delta Z}$ / mb | mass-changing cross section $\sigma_{\Delta A}$ / mb |
|---|---|---|---|
| measured (this work) | $213 \pm 7$ | $568 \pm 35$ | $800 \pm 58$ |
| calculated (this work) | $213 \pm 7$ | $569 \pm 70$ | $792 \pm 83$ |
| measured [71] | 200 | / | $636 \pm 76$ |

They are in good agreement with each other, which proves the self-consistency of the presented dataset. The *total fragmentation cross section* (equivalent to the definition of the mass-changing cross section found in Section 2.8.1) estimated by Rovituso et al. [71] from a thick target measurement is considerably lower than the values presented in this work. Most probable, this discrepancy can be explained by comparing the methods applied for particle identification. The standard $\Delta E - E$ attenuation method used by Rovituso et al. has large overlap areas in the spectra used for identification while in the present work an improved and more robust particle identification method is used, which exploits the pulse shape of the $BaF_2$ scintillator as an additional measure for the atomic number of the outgoing ions. Also cross section measurements with thin targets are superior over thick

target measurements concerning the required full acceptance. Furthermore the obtained elemental cross sections shown in Figure 4.2 are consistent with the literature data and clearly follow the expected trend.

### 4.1.3 Optimization of Tripathi Parametrization

A modified version of the Tripathi model based on the new cross section data is shown in Figure 4.2 for the $^4$He-nucleus reactions ($^4$He $+^{12}$ C, $^4$He $+^{16}$ O and $^4$He $+^{28}$ Si). In the original Tripathi model [127] the parameter $D_{^4He}$ which modifies the $^4$He-nucleus reaction cross section at low and intermediate energies is calculated according to Equation 2.16. Tripathi et al. optimized $D_{^4He}$ to match the $^4$He experimental data by Auce et al. [165] and Jaros et al. [169]. However, the data by Auce et al. were later measured again by Ingemarsson et al. [166], using an improved version of the experimental setup developed for the Auce experiment. These revised cross sections are slightly higher than the old values that Tripathi et al. used for their model optimization. Consequently the model should be updated to match the Ingemarsson data. The experimental cross sections obtained in the present experiments suggest that the Tripathi reaction cross section parametrization should also be increased to higher values in the energy range $70 - 220$ MeV/u. Therefore a modification of the parameter $D_{^4He}$ in the Tripathi parametrization according to Equation 4.1 is suggested (adjusted parameters marked in red).

$$D_{^4He}^{optimized} = 2.2 - 8.0 \cdot 10^{-3} \cdot A_T + 1.8 \cdot 10^{-5} \cdot A_T^2 - \frac{0.3}{1 + e^{(\frac{120-E}{50})}} \tag{4.1}$$

As shown in Figure 4.2 the optimized version of the Tripathi model (solid line in panel a-c) matches the experimental cross sections presented in this work and those by Ingemarsson et al. better than the original model while the prediction for high energies ($> 1$ GeV/u) is almost unaffected by the proposed parameter changes. Besides the agreement with the new experimental data, the optimized parametrization is also in good accordance with the theoretical $^4$He$+^{12}$C reaction cross section prediction from optical model calculations by DeVries and Peng [124] (a comparison is shown in [146]). Using the optimized Tripathi reaction cross section model instead of the original one can be expected to result in considerable improvements of $^4$He ion transport calculations related to radiotherapy applications (e.g. calculation of dose distributions in a patient) because C and O are the main constituents of biological soft tissues. The optimized model still under-estimates the Ingemarsson data points for the $^4$He $+^{28}$ Si system at low energy. However, it is in agreement with the data by Warner et al. [172]. The overall agreement of the modified version with the experimental data is better than for the original model and at intermediate energies (the important energy range for radiotherapy) the scaling towards heavier target nuclei (up to $^{28}$Si) still works well.
As an alternative to the optimized Tripathi model, also the reaction cross section model by Shen et al. [130] (improved by Sihver et al. [177]) may be used. Its predictions of $^4$He-nucleus reaction cross sections are also in reasonable agreement with the present experimental data and those by Ingemarsson for C and O targets. The Shen model is available as an option in some Monte Carlo codes, e.g. Geant4 [8] as used by Fuchs et al. [178] and Knäusl et al. [111] to study possible radiotherapy applications of $^4$He ions.

For the $^{4}$He-$^{1}$H reaction cross section model (solid line in Figure 4.2, panel d), also designed by Tripathi et al. [128], no parameter changes are proposed on basis of the present experiments because its prediction matches the obtained cross sections within the error bars. However, the measurement uncertainties are large for H targets due to the propagation of the C and $CH_2$ cross section errors into the error of the H cross section. With more complex measurement methods (e.g. by using a liquid hydrogen target instead of a combination of C and $CH_2$ targets) there is still room for improvements. However, it should be noted, that the major contributor to the reaction cross section of $H_2O$ (the reference medium in radiotherapy) is the O nucleus rather than the two H nuclei.

## 4.2 Target Fragmentation Experiments

### 4.2.1 Measured Decay Curves of Activated Targets

Figure 4.3 shows the measured decay curves for graphite and BeO targets irradiated with protons and $^{12}$C ions.

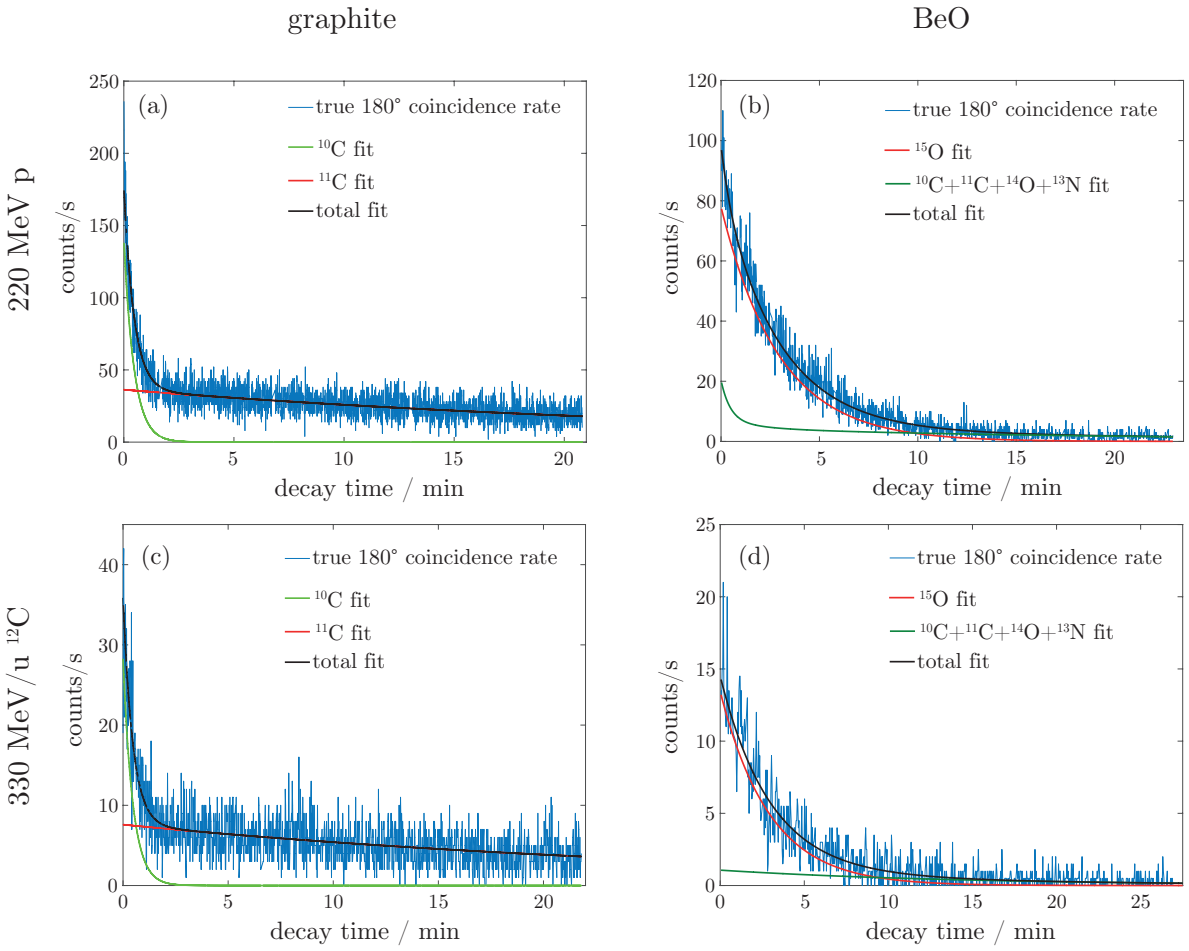


**Figure 4.3:** Examples of measured decay curves for graphite (panel (a) and (c)) and BeO targets (panel (b) and (d)) irradiated with protons (panel (a) and (b)) and $^{12}$C ions (panel (c) and (d)).

It can be observed that for the graphite targets the activity decreases fast in the first two minutes after irradiation because the short-lived $^{10}$C (half life: 19.29 s) dominates the activity while later only the produced $^{11}$C (half life: 20.334 min) remains. In contrast to these distinct two decay components, the decay curves of the activated BeO are dominated by the produced $^{15}$O (half life: 122.24 s) and the other produced isotopes ($^{10}$C, $^{11}$C, $^{14}$O, $^{13}$N) only contribute a few percent to the total activity. It can also be seen, that the produced activity per irradiation pulse was considerably lower for $^{12}$C ions than for protons which results in a lower signal to noise ratio (and thus less accurate cross section measurements as seen below). This can be explained by the performance of the radiotherapy accelerator operated at MIT: in the facility design phase the maximum intensities (ions per second) that need to be extracted from the synchrotron were defined in terms of dose rate. Due to the much higher LET of $^{12}$C ions compared to protons, the maximum $^{12}$C ion intensity can be a factor of $\sim 30$ lower than the proton intensity and still generate the same dose rate. Also the PET counting statistics that can be collected for range verification during patient treatments with $^{12}$C ions suffers from this relation compared to proton therapy [75]. However, in the experiments at MIT the lower particle numbers in the $^{12}$C ion beam pulses were partially compensated by their larger nuclear reaction cross sections and sharper beamspots (better detection efficiency) compared to protons. Additionally, the $^{12}$C ion irradiation times were increased up to twice the length of the proton pulses to further increase the number of primary particles and thereby the amount of produced activity.

### 4.2.2 PET Isotope Production Cross Sections

The initial activities obtained from the fit functions shown in Figure 4.3 could be converted into the production cross sections by applying Equation 3.7. Figure 4.4 shows the $^{10}$C and $^{11}$C production cross sections as a function of energy (*excitation functions*) for protons impinging on $^{12}$C targets. For comparison also the Q-values (the energy that is absorbed in a nuclear reaction) for both channels calculated by comparing the masses of the nuclei in the initial and in the final state are shown.
A lot of reference data are available for the $^{12}\mathrm{C}(\mathrm{p},\mathrm{pn})^{11}\mathrm{C}$ reaction channel and the cross section data obtained in the present experiments fit rather well into the general systematics. There is a good agreement between the present data and the reference data from the literature except those from the very early publications by Hintz et al. [179] and Aamodt et al. [180] and the very recent work by Bäumer et al. [181] and Bäcker et al. [182]. While deviations of the cross section values obtained in the present experiments from values published in the 1950s are not particularly surprising, the deviation from the cross section at 100 MeV reported by Bäumer et al. ($\sim 5\%$ from error bar to error bar and $\sim 17\%$ from value to value) needs more attention and is therefore discussed in the following. The approach to determine the $^{11}$C production cross section via the measurement of the amount of induced activity is comparable to the approach described in this work, however, their experimental method is quite different. While the experiment described here was set up in-beam and the induced $\beta^+$ activity was measured with scintillation detectors coupled by a coincidence unit, Bäumer et al. transported their irradiated targets from the proton therapy center in Essen to a low background gamma spectrometry facility in Dortmund $\sim 35$ km away to analyze the samples there using a well-characterized high purity germanium detector for measurement of the 511 keV gamma photons. They used

the same graphite target material type with high purity as used in this work, therefore no differences can be expected from the material, but the irradiation fields used are quite different: while in the present work the targets were irradiated with a single pencil beam impinging on the target center, Bäumer et al. irradiated their targets with a scanned beam producing a homogeneous fluence on the target. Only slight differences (not more than $\sim 3\%$ according to a dosimetric study by Gomá et al. [183]) may originate from the different way of determining the number of primary particles impinging on the target.

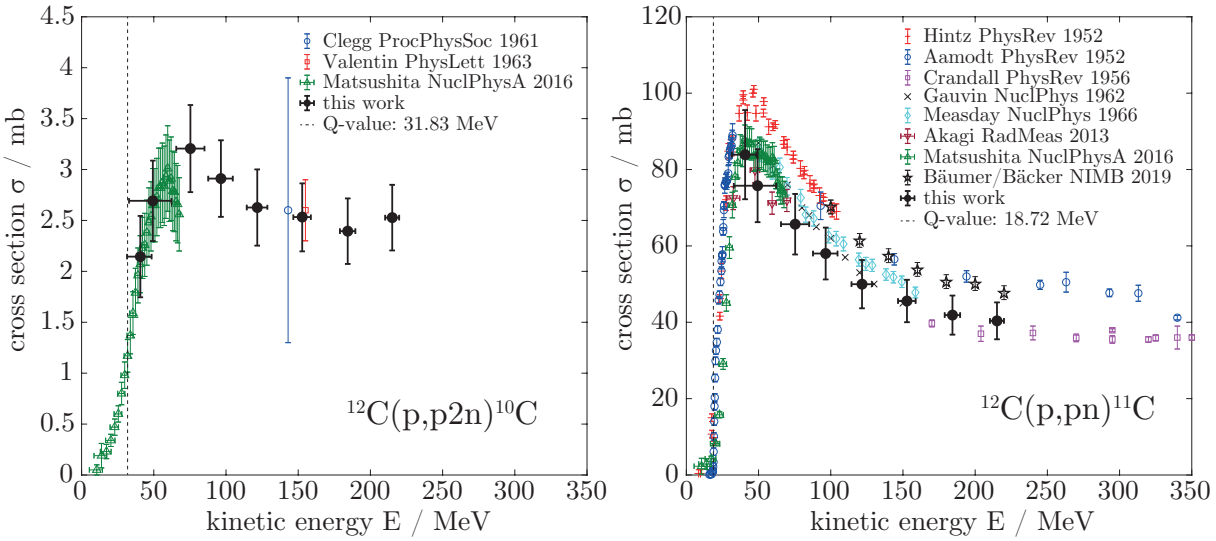


**Figure 4.4:** Cross sections for the production of $^{10}$C and $^{11}$C target fragments by protons on C targets as a function of energy. The black filled circles are the data measured in the present experiments by irradiating graphite targets. The $^{10}$C reference data are from [184, 185] and [186]. The $^{11}$C reference data are from [186, 179, 180, 187, 188, 189, 190, 181, 182]. The dashed lines mark the calculated Q-values for the reactions, which represent the $^{10}$C and $^{11}$C production thresholds.

In this work the clinical monitor calibration determined by an absorbed dose to water measurement under dosimetric reference conditions was used while Bäumer et al. did separate measurements with a Faraday cup. The possible origin of the discrepancies between primary particle fluences determined by means of ionization chamber measurements and Faraday cup measurements has been widely discussed [191, 192] and it is still not finally resolved which method gives the more accurate results. Therefore, a conservative estimate on the accuracy of the ionization chamber based monitor calibration is included in the uncertainty calculation (see Section 3.5.8.2). The origin of the remaining discrepancy between the $^{11}$C production cross sections determined in the present experiments and those of Bäumer et al. and Bäcker et al. are not clear yet but common efforts to investigate this point are ongoing.
The $^{12}$C(p, p2n)$^{10}$C reaction channel has been less investigated in previous studies than the channel for $^{11}$C production, however, there is also reasonable agreement between the $^{10}$C production cross sections presented here and the few data available in the literature. The decrease to higher energies measured by Matsushita et al. [186] might be an edge artifact due to their experimental method (PET imaging of thick targets after irradiation). Also the fact that they measured $^{10}$C production cross section values greater than zero below the Q-value of the reaction is probably an artifact because they obtained their

energy information by correlation of the induced activity with the depth in their target. However, this relation is strongly smeared at high depths by the energy loss straggling. Figure 4.5 shows the $^{10}$C and $^{11}$C production cross sections as a function of energy for $^{12}$C ions impinging on C targets.

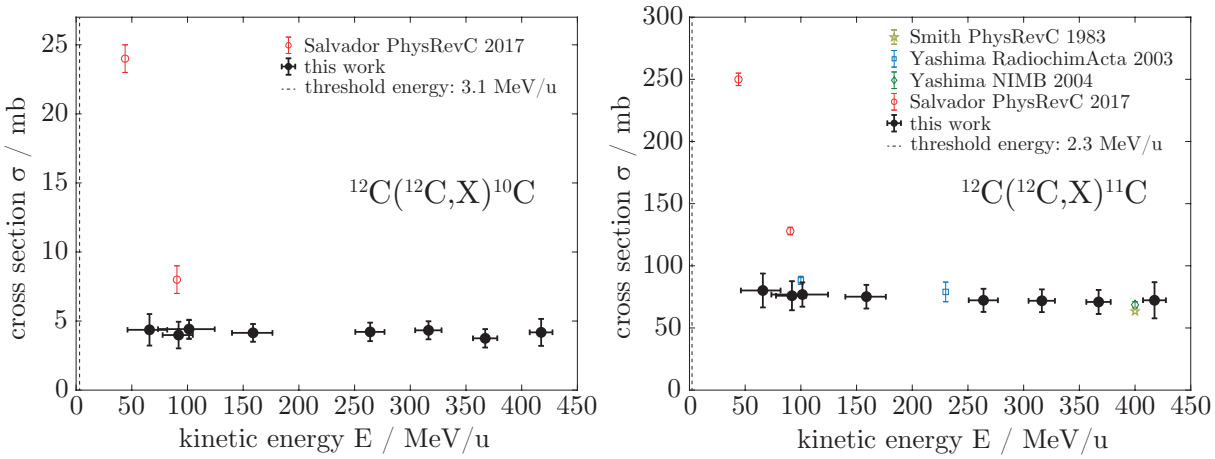


**Figure 4.5:** Cross sections for the production of $^{10}$C and $^{11}$C target fragments by $^{12}$C ions on C targets as a function of energy. The black filled circles are the data measured in the present experiments by irradiating graphite targets. The $^{10}$C reference data are from [193]. The $^{11}$C reference data are from [194, 195, 196] and [193]. The dashed lines mark the FLUKA calculated thresholds for the $^{10}$C and $^{11}$C production reactions.

In the case of $^{12}$C projectiles the simple calculation of a single Q-value as done for the proton-induced reactions is not sufficient to describe the reaction threshold appropriately due to the several different projectile fragmentation channels that are possible. Therefore, the reaction thresholds shown in Figure 4.5 were calculated using an appropriate built-in FLUKA routine that returns the corresponding energy threshold for each fragmentation channel. The minimum energy threshold among all possible fragmentation channels is used here as reaction threshold. However, it is important to note that unless complete fusion occurs, usually not all nucleons take part in a nucleus-nucleus reaction, and therefore the required energy per nucleon is actually greater for most of the collision processes than that given by the reaction threshold. Moreover, due to its not straightforward determination, the Coulomb barrier has not been considered in the calculation of the reaction thresholds. Therefore, the values shown in Figure 4.5 should only be used as rough indicator of the actual minimum energy per nucleon needed for the reaction to occur. The available data for target fragmentation induced by $^{12}$C projectiles is much more sparse than for protons. The few datapoints from experiments at the Bevalac [194] and at the HIMAC accelerator [195, 196] compare reasonably well with the present cross sections while the newer datapoints from Salvador et al. measured at GANIL [193] are significantly higher. In contrast to the proton data (see Figure 4.4), no rise of the $^{10}$C and $^{11}$C production cross sections on $^{12}$C targets towards lower energies can be observed for incident $^{12}$C ions in the energy range investigated in this work.
Figure 4.6 shows the same data as Figure 4.4 and Figure 4.5, but as the ratio of the $^{10}$C and $^{11}$C production cross sections both for protons (left panel) and $^{12}$C ions (right panel) impinging on C targets as a function of energy. Most of the systematic uncertainties cancel out when calculating the ratio, therefore the error bars are considerably smaller

than in Figures 4.4 and 4.5. However, the remaining uncertainties due to the counting statistics are larger for the $^{12}$C ion measurements than for the proton measurements due to the lower beam intensities (see decay curves in Figure 4.3). A comparison with literature data is only possible for experiments where $^{10}$C and $^{11}$C production were measured simultaneously. This is only the case for the datasets from Matsushita et al. [186] and Salvador et al. [193].

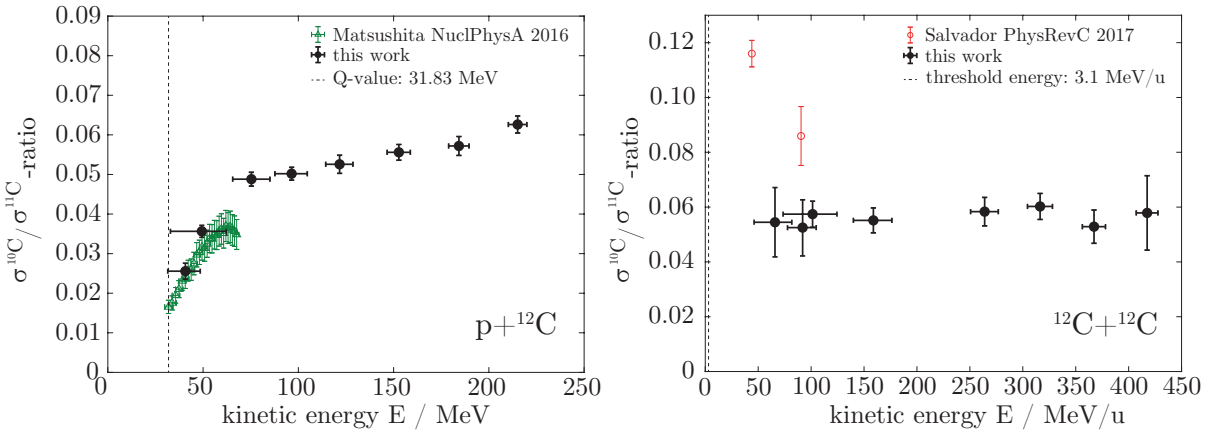


**Figure 4.6:** Ratio of the production cross sections for $^{10}$C and $^{11}$C target fragments produced by protons (left panel) and $^{12}$C ions (right panel) on C targets as a function of energy. The experimental data are from [186] and [193]. The dashed lines mark the calculated Q-value for the proton-induced $^{10}$C production reaction and the FLUKA calculated threshold for the corresponding $^{12}$C ion-induced reaction.

The present proton data compare reasonably well with those by [186] (their values below the Q-value of 31.83 MeV are not shown, see discussion above) while for $^{12}$C ions the ratios presented here are again lower than those reported by Salvador et al. [193]. For protons, the two-neutron-removal reaction cross section ($^{10}$C production) relative to the cross section for removal of only one neutron ($^{11}$C production) decreases with decreasing energy while for $^{12}$C projectiles, no energy-dependency could be observed at all in the investigated energy range of this study (down to $\sim$ 75 MeV/u).
Figure 4.7 shows the $^{15}$O production cross section as a function of energy for protons and $^{12}$C ions impinging on O targets. For the $^{16}$O(p, pn)$^{15}$O reaction channel, the measured dataset fits well into the literature data and extends them towards higher energies. For the corresponding $^{12}$C ion reaction, there is fair agreement with the higher energy datapoint by Salvador et al. [193] but again (see also Figure 4.5) the rise of the cross section towards lower energies which they report could not be reproduced in the present experiments. Their experimental method is comparable to the present approach (monitoring of the 511 keV photon emission with a pair of scintillators and a coincidence logic), but they do not report any random coincidence correction. However, as shown in Figure 3.14, without this correction the produced activity of the generated isotopes and consequently their production cross sections may be overestimated. Therefore, one could speculate that the discrepancy between the cross sections reported by Salvador et al. and the values presented here could be due to a missing correction for random coincidences in the method by Salvador et al. [193]. Another point where their experiment and the measurements presented in this work differ considerably is the method how the beam energy was varied:

While at MIT the energy is actively changed by the synchrotron, Salvador et al. had to use degrader plates which introduces the issue that the beam gets already contaminated by fragments before hitting the target and the energy spectrum gets broadened due to straggling. Another point where their method differs from the one presented here is that their target had to be moved to the measurement position after the irradiation while our setup could measure in-beam. Further research or comparisons could help to clarify where exactly those differences come from.

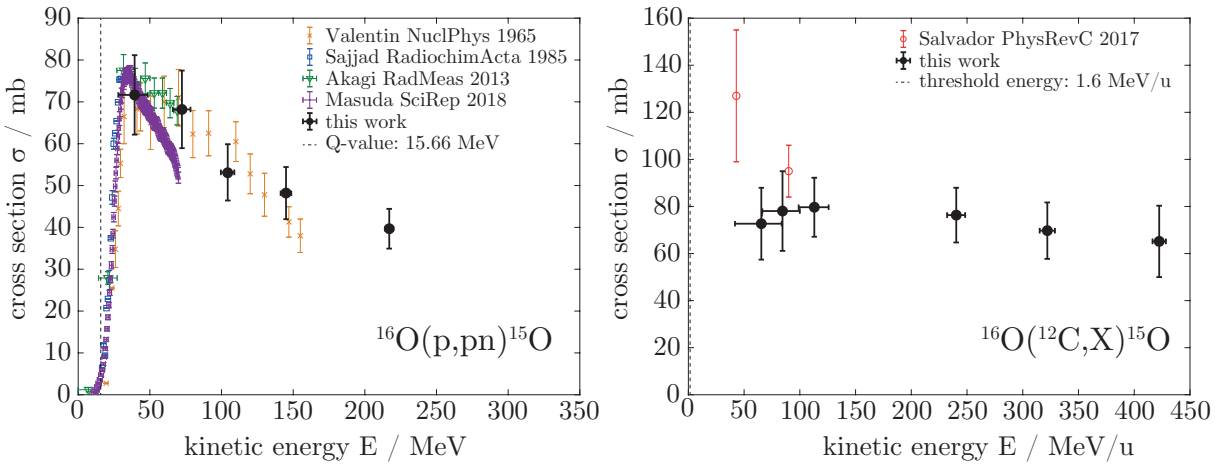


**Figure 4.7:** Cross sections for the production of $^{15}$O target fragments by protons (left panel) and $^{12}$C ions (right panel) on O targets as a function of energy. The black filled circles are the data measured in the present experiments by irradiating BeO targets. The reference data for protons are from [197, 198, 190] and [199]. The reference data for $^{12}$C ions are from [193]. The dashed lines mark the calculated Q-value for the proton-induced $^{15}$O production reaction and the FLUKA calculated threshold for the corresponding $^{12}$C ion-induced reaction.

Generally, the threshold energies (expressed in MeV/u) are considerably lower for the $^{12}$C ion reactions than for the proton-induced reactions. For protons this leads to a gap of $\sim 2-5$ mm between the end of the activity profiles and the Bragg peak [75], while $^{12}$C ions produce target fragments almost until the end of their range. Thus for $^{12}$C ions there is a clear range correlation not only in the $\beta^+$-activity profiles of the $^{10}$C and $^{11}$C projectile fragments (see Figure 2.12) but also in those of the $^{10}$C, $^{11}$C and $^{15}$O target fragments created along the beam path.
The cross section data plotted in Figure 4.4, 4.5 and 4.7 are also compiled in Table 4.3 and Table 4.4.

**Table 4.3:** Measured cross sections for the production of $^{10}$C and $^{11}$C target fragments by protons and $^{12}$C ions on $^{12}$C targets. The kinetic energy has asymmetric uncertainty intervals.

| projectile | target | thickness / mm | kinetic energy / MeV/u | $^{10}$C production cross section / mb | $^{11}$C production cross section / mb |
|---|---|---|---|---|---|
| p | $^{12}$C | 9.91 | $215.1^{+4.8}_{-4.9}$ | $2.53 \pm 0.33$ | $40.4 \pm 4.8$ |
| p | $^{12}$C | 9.90 | $184.3^{+5.3}_{-5.4}$ | $2.40 \pm 0.33$ | $41.9 \pm 5.1$ |
| p | $^{12}$C | 9.91 | $152.8^{+6.0}_{-6.2}$ | $2.53 \pm 0.34$ | $45.6 \pm 5.6$ |
| p | $^{12}$C | 9.85 | $121.7^{+7.0}_{-7.3}$ | $2.63 \pm 0.38$ | $50.0 \pm 6.3$ |
| p | $^{12}$C | 9.83 | $96.5^{+8.2}_{-8.8}$ | $2.91 \pm 0.38$ | $58.0 \pm 6.8$ |
| p | $^{12}$C | 9.91 | $75.4^{+9.6}_{-9.8}$ | $3.21 \pm 0.43$ | $65.7 \pm 7.9$ |
| p | $^{12}$C | 9.83 | $49.3^{+12.9}_{-16.5}$ | $2.69 \pm 0.40$ | $75.8 \pm 9.6$ |
| p | $^{12}$C | 4.99 | $40.7^{+7.8}_{-9.2}$ | $2.15 \pm 0.41$ | $83.4 \pm 11.7$ |
| $^{12}$C | $^{12}$C | 9.91 | $417.5^{+10.2}_{-10.3}$ | $4.18 \pm 0.99$ | $72.3 \pm 14.5$ |
| $^{12}$C | $^{12}$C | 9.90 | $367.3^{+10.8}_{-11.0}$ | $3.75 \pm 0.67$ | $70.9 \pm 9.7$ |
| $^{12}$C | $^{12}$C | 9.91 | $316.4^{+11.7}_{-11.9}$ | $4.33 \pm 0.66$ | $71.9 \pm 9.2$ |
| $^{12}$C | $^{12}$C | 9.91 | $264.0^{+12.9}_{-13.3}$ | $4.21 \pm 0.68$ | $72.2 \pm 9.3$ |
| $^{12}$C | $^{12}$C | 9.91 | $158.8^{+17.4}_{-18.9}$ | $4.15 \pm 0.65$ | $75.2 \pm 9.5$ |
| $^{12}$C | $^{12}$C | 9.90 | $101.4^{+23.0}_{-27.9}$ | $4.42 \pm 0.69$ | $76.9 \pm 9.8$ |
| $^{12}$C | $^{12}$C | 5.01 | $92.0^{+12.8}_{-14.3}$ | $3.99 \pm 0.99$ | $75.9 \pm 11.7$ |
| $^{12}$C | $^{12}$C | 4.99 | $65.9^{+15.9}_{-19.7}$ | $4.37 \pm 1.17$ | $80.2 \pm 13.7$ |

**Table 4.4:** Measured cross sections for the production of $^{15}$O target fragments by protons and $^{12}$C ions on $^{16}$O targets. The kinetic energy has asymmetric uncertainty intervals.

| projectile | target | thickness / mm | kinetic energy / MeV/u | $^{15}$O production cross section / mb |
|---|---|---|---|---|
| p | $^{16}$O | 3.93 | $217.0^{+2.8}_{-2.9}$ | $39.7 \pm 4.8$ |
| p | $^{16}$O | 3.92 | $145.0^{+3.7}_{-3.8}$ | $48.2 \pm 6.3$ |
| p | $^{16}$O | 3.91 | $104.2^{+4.6}_{-4.8}$ | $53.2 \pm 6.8$ |
| p | $^{16}$O | 3.88 | $72.4^{+6.0}_{-6.4}$ | $68.2 \pm 9.4$ |
| p | $^{16}$O | 3.91 | $39.4^{+9.1}_{-11.4}$ | $71.7 \pm 9.6$ |
| $^{12}$C | $^{16}$O | 3.92 | $422.4^{+5.9}_{-6.0}$ | $65.1 \pm 15.4$ |
| $^{12}$C | $^{16}$O | 3.91 | $322.0^{+6.8}_{-6.9}$ | $69.8 \pm 12.2$ |
| $^{12}$C | $^{16}$O | 3.88 | $240.3^{+8.0}_{-8.2}$ | $76.4 \pm 11.8$ |
| $^{12}$C | $^{16}$O | 3.82 | $113.0^{+12.9}_{-14.0}$ | $79.7 \pm 12.7$ |
| $^{12}$C | $^{16}$O | 3.91 | $84.5^{+15.6}_{-18.1}$ | $78.0 \pm 17.2$ |
| $^{12}$C | $^{16}$O | 3.90 | $65.5^{+18.3}_{-23.6}$ | $72.7 \pm 15.5$ |

## 4.3 Radiation Transport Calculations

The cross sections measured in the experiments performed within the scope of this thesis are useful for nuclear reaction modeling in radiation transport codes. For $^{4}$He ions the dose calculation accuracy of the Monte Carlo codes TOPAS/Geant4 and FLUKA and the treatment planning system TRiP98 could be improved by using the $^{4}$He mass-changing cross sections shown in Section 4.1.2 for optimization of the corresponding nuclear reaction model. The PET isotope production cross sections shown in Section 4.2.2 for protons were validated by applying them for a transport calculation and comparing the calculated $\beta^{+}$-activity profiles with measured profiles from a PET measurement found in the literature. The optimization of the FLUKA physics models on basis of the cross sections for PET isotope production by $^{12}$C ions (Figures 4.5 and 4.7) is in progress [200].

### 4.3.1 Nuclear Reaction Model Optimization for $^{4}$He Ions

As discussed in Section 2.6 the comparison of radiation transport code predictions with recent dose measurements showed that there was a need for the adjustment of the $^{4}$He nuclear reaction models implemented in transport codes commonly used for ion beam therapy applications, in particular TRiP98 [4] and FLUKA [113]. The Tripathi parametrization of the total reaction cross section $\sigma_R$ (see Section 2.8.2.2) used in TRiP98, but implemented also in several Monte Carlo codes, was optimized on basis of the measured cross sections as shown in Figure 4.2. Furthermore the FLUKA code developers have also adjusted their total reaction cross section model (an empirically modified version [129] of the Tripathi model) to fit the novel cross section data shown in Figure 4.2.

#### 4.3.1.1 Validation of Optimized Tripathi Parametrization

The optimized Tripathi parametrization for $^{4}$He ions shown in Figure 4.2 could be validated by comparison of calculated depth dose profiles in water with dose measurements recently performed at HIT [113] as shown in Figure 4.8. The profiles were normalized to the entrance channel because the entrance dose is rather independent of the fragmentation model and typically the beam monitors of a particle therapy system are calibrated by performing an absolute dose measurement at low depth [183]. As discussed in Section 4.1.3, the original Tripathi model underestimates the $^{4}$He reaction cross section and therefore the number of ions fragmenting during their way through the water target is predicted too low. By increasing the reaction cross section in the intermediate energy range as done on basis of the novel experimental cross section data (shown in Figure 4.2) also the number of $^{4}$He ions that actually reaches the Bragg peak depth without fragmentation decreases. This results in a degradation of the Bragg peak dose and leads to a good agreement of calculated and measured dose profiles.
The degradation of the Bragg peak dose with depth has also some influence on the optimization of a spread out Bragg peak (SOBP). If a flat SOBP is planned with a transport code with inaccurate nuclear reaction models the SOBP can actually appear tilted with an under- or over-dosage (depending if the cross sections are modeled too low or too high, see Figure 2.9). This effect could be observed during radiobiological experiments

performed at HIT as reported by Krämer et al. [4]: An SOBP was planned with TRiP98 for a flat dose using the original Tripathi model but during the measurement it appeared tilted. Figure 4.9 shows a recalculation of this SOBP with TOPAS using the original and the optimized Tripathi model.

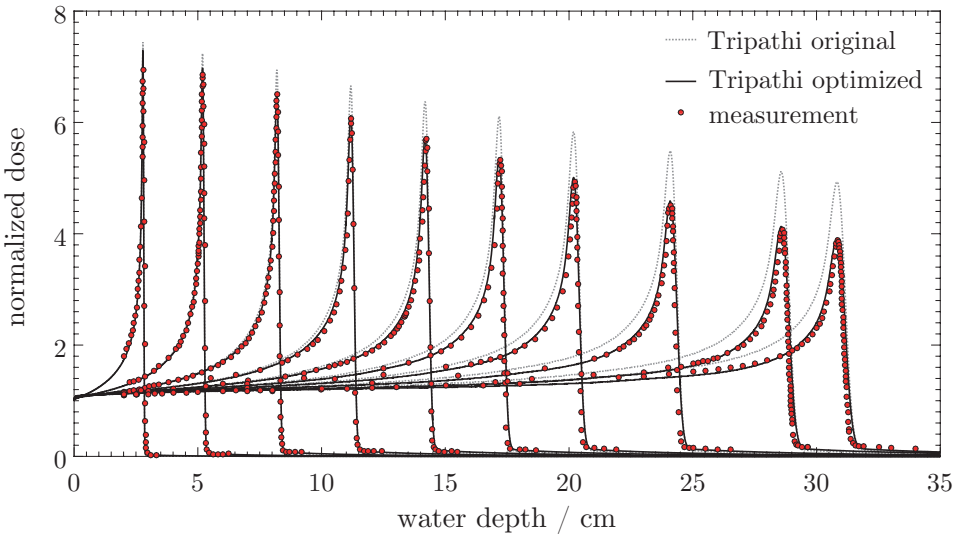


**Figure 4.8:** $^4$He Bragg curves in water in the energy range $50 - 220$ MeV/u calculated with the TOPAS/Geant4 Monte Carlo code using the original and the optimized Tripathi model in comparison with dose measurements by Tessonnier et al. [113].

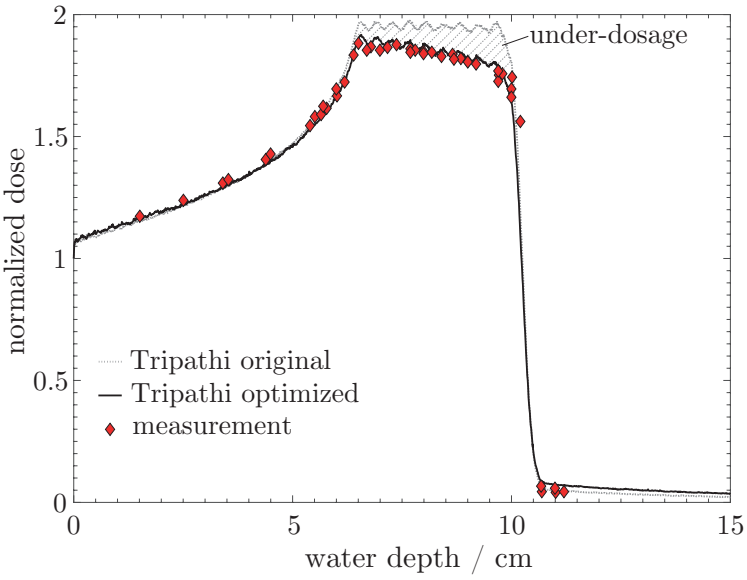


**Figure 4.9:** $^4$He SOBP in water calculated with the TOPAS/Geant4 Monte Carlo code using the original and the optimized Tripathi model in comparison with dose measurements by Krämer et al. [4].

The tilt and under-dosage that were observed experimentally can be reproduced with good accuracy when the optimized version of the Tripathi parametrization is used for

dose calculation instead of the original one that was used by Krämer et al.

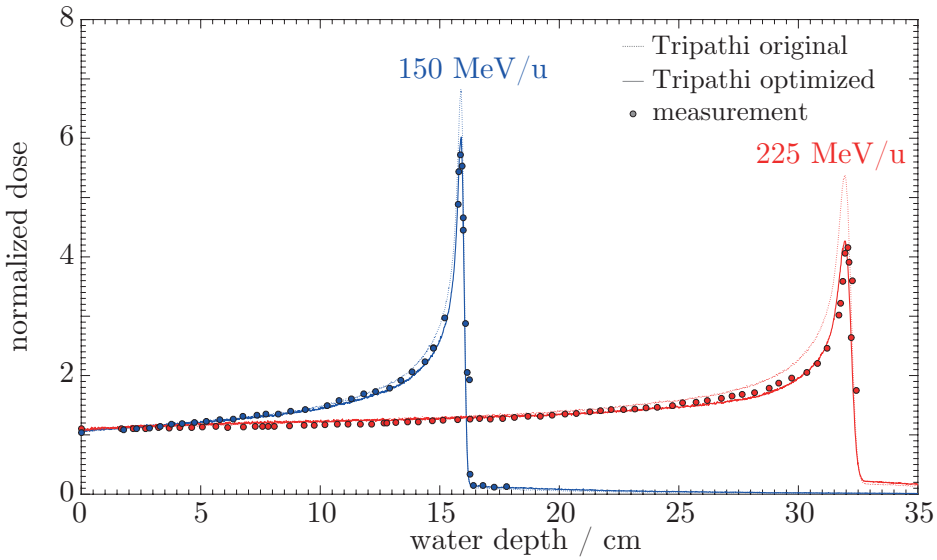


**Figure 4.10:** $^4$He Bragg curves in water calculated with the TOPAS/Geant4 Monte Carlo code using the original and the optimized Tripathi model in comparison with dose measurements by Lyman and Howard [163].

As shown in Figure 4.10, the same improvements in dose calculation can also be observed when comparing calculated dose profiles with historical measurement data from the $^4$He ion therapy beamline at the Bevalac accelerator in Berkeley [163], even if these data have a lower depth resolution in the Bragg peak region than the measurements from HIT.

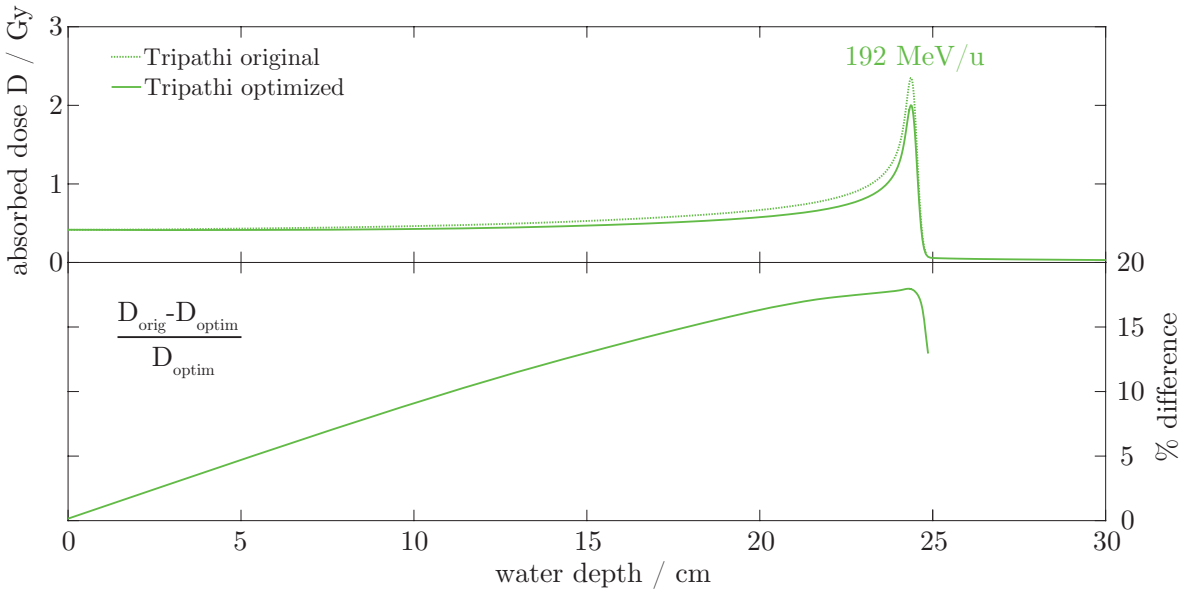


**Figure 4.11:** $^4$He Bragg curve in water calculated with TRiP98 using the original and the optimized Tripathi model plus their percentage difference.

Figure 4.11 shows a 192 MeV/u $^4$He Bragg curve in water calculated with the treatment

planning system TRiP98 using the original and optimized Tripathi model as well as the relative difference as a function of depth. The absorbed dose was planned to be 2 Gy at the Bragg peak calculated with the optimized model. The same degradation of the Bragg peak dose as for the TOPAS/Geant4 calculations can be observed. By increasing the total reaction cross section also an increase in the dose tail caused by fragments would be expected, as visible in the TOPAS/Geant4 calculations (Figures 4.8, 4.9 and 4.10), however, this part of the TRiP98 code is not yet adjusted (unlike in Monte Carlo codes like Geant4, the removal of primary ions and the production of fragments are decoupled in TRiP98). Therefore, the difference between the two calculations (lower panel in Figure 4.11) is only shown up to a depth of 25 cm. Besides absorbed dose profiles TRiP98 can also calculate the RBE using the LEM formalism (see Section 2.4.1). In Section 4.3.1.3 RBE profiles corresponding to the dose profiles shown in Figure 4.11 are presented and discussed.
As seen from the data in this section, calculations related to $^4$He radiotherapy with the original Tripathi model would lead to an under-dosage of the tumor because the Bragg peak doses would be overestimated in the treatment planning. The optimized Tripathi model predicts the shape of the Bragg curves close to the dose measurements and therefore can be considered suitable for $^4$He dose calculation in clinical scenarios.

#### 4.3.1.2 Optimization of the $^4$He Nuclear Reaction Model in FLUKA

The parametrization implemented in FLUKA underestimated the $^4$He reaction cross section in the energy range $\sim 50 - 500$ MeV/u similar to the original Tripathi model shown in Figure 4.2, but with the difference that it had already been increased at low energies to match the data by Ingemarsson et al [166]. Consequently the FLUKA parametrization of $\sigma_R$ was adjusted in the energy range of the measurements described in Section 4.1.2, also taking into account the inelastic scatter contributions as discussed in Sections 2.3.3 and 2.8.1.

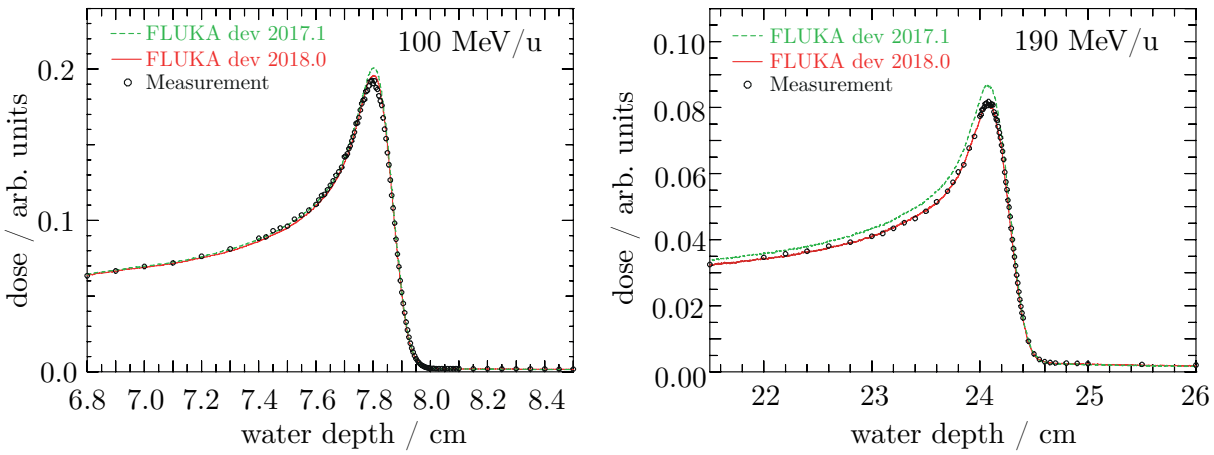


**Figure 4.12:** Zoom in the peak region of Bragg curves in water calculated with FLUKA using the previous and the optimized nuclear reaction model (calculation by G. Aricò, CERN) compared to dose measurements by Tessonnier et al. [113].

Details on the adjustments of the FLUKA models can be found in an article by Aricò et al. [201]. These model changes are implemented in FLUKA from the development version 2018.0 on. The $^4$He dose calculation accuracy of the new FLUKA development version is better than 1% for mono-energetic beams in water [201] whereas previous versions showed deviations of 5% and larger. Also in patient-like geometries satisfactory agreement with measurements could be reached [202]. The examples shown in Figure 4.12 demonstrate the improvement of dose calculation by adjustment of the FLUKA models to the novel cross section data.
The optimization of the FLUKA models has a high clinical relevance because the FLUKA code is used to generate the basic data for the treatment planning system at HIT where the treatment of patients with $^4$He ions is currently being prepared.

#### 4.3.1.3 Impact of Nuclear Model Adjustments on $^4$He RBE Profiles

In addition to the absorbed dose profiles shown in Figure 4.11 also RBE profiles for two different tissues (a radioresistant one with $\alpha/\beta = 2$ Gy and a sensitive one with $\alpha/\beta = 10$ Gy) were calculated with TRiP98. These profiles are shown in Figure 4.13 together with the percentage differences between the profiles obtained with the original Tripathi reaction cross section model and the optimized one.

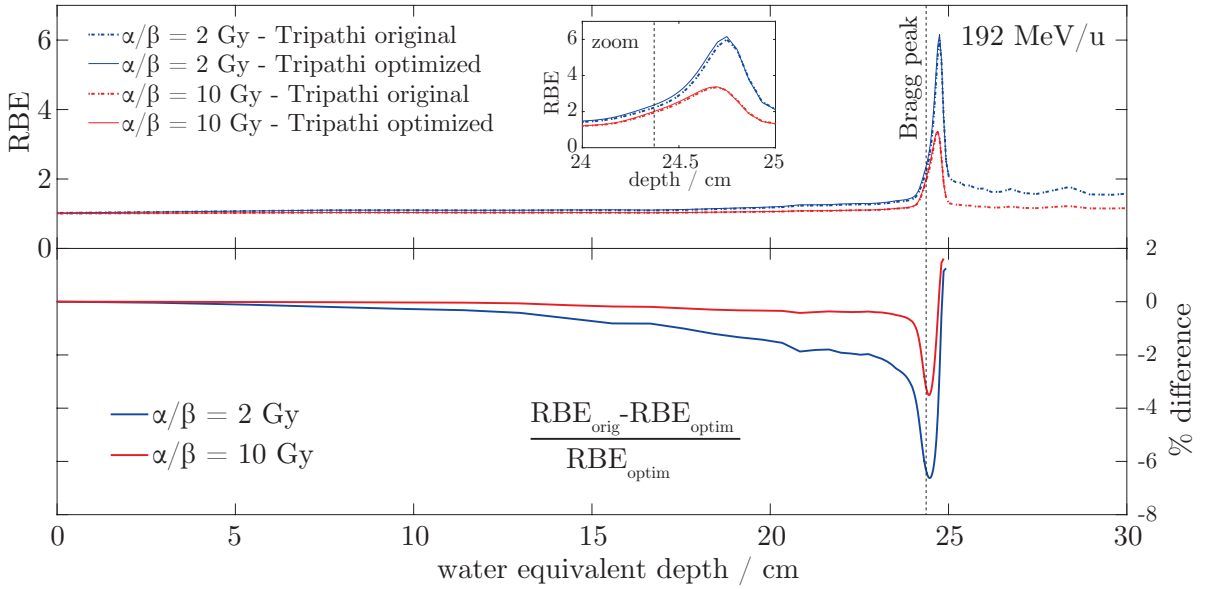


**Figure 4.13:** RBE profiles for 192 MeV/u $^4$He ions calculated with TRiP98 (calculation by D. Boscolo, GSI) for two different tissues using the original and the optimized Tripathi model plus their percentage difference. The LEM IV input parameters were $\alpha = 0.1$ Gy$^{-1}$, $\beta = 0.05$ Gy$^{-2}$ and $D_{cut} = 8$ Gy mimicking normal tissue ($\alpha/\beta = 2$ Gy) and $\alpha = 0.5$ Gy$^{-1}$, $\beta = 0.05$ Gy$^{-2}$ and $D_{cut} = 14$ Gy for a typical tumor tissue ($\alpha/\beta = 10$ Gy).

The RBE profiles appear to be very similar for the two different nuclear reaction models and they can not be distinguished well by eye. However, by looking at the lower panel of Figure 4.13 it can be observed that due to a slight shift of the profiles (visible in the

zoom in the upper panel) their differences increase up to significant values towards larger depths ($\sim$ 4% in the sensitive tissue and $\sim$ 7% in the radioresistant tissue in the Bragg peak region). This shift of the RBE profiles to lower depths for the optimized nuclear model can be attributed to the dose dependency of the RBE (see Section 2.4) rather than to the change in radiation quality as discussed in the following.

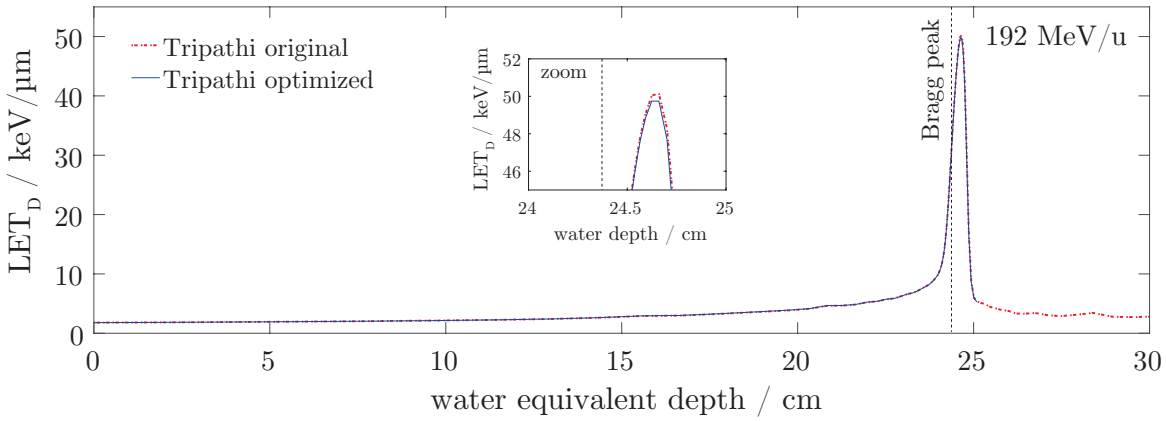


**Figure 4.14:** Dose-averaged linear energy transfer profiles for 192 MeV/u $^4$He ions calculated with TRiP98 (calculation by D. Boscolo, GSI) using the original and the optimized Tripathi model.

Figure 4.14 shows depth profiles of the dose-averaged linear energy transfer $LET_D$, which can serve as a rough measure of the radiation quality [203], for the original and the optimized Tripathi model. The two profiles are almost identical because the primary $^4$He ions dominate the radiation field even if a few percent more of them fragment until the end of their range by increasing the reaction cross section in the transport calculation. For high LET radiation the RBE increases towards lower doses because of the *repair shoulder* typical for x-ray dose response curves but not for high LET particles (see Figure 2.10). The adjustment of the Tripathi reaction cross section model causes a reduction of the Bragg peak dose and thereby increases the RBE effects in this region.
Remarkably, the trend of the RBE deviation between the original and optimized Tripathi model (see lower panel of Figure 4.13) and the corresponding absorbed dose deviation (lower panel of Figure 4.11) are opposite. This means that the physical and radiobiological uncertainties due to inaccurate nuclear reaction models can compensate each other to some degree, especially for radioresistant tissues where RBE effects are more pronounced than in radiosensitive tissues.

### 4.3.2 PET Isotope Production by Protons

Figure 4.15 shows the optimized models for the $^{12}C(p, pn)^{11}C$ and $^{16}O(p, pn)^{15}O$ reactions on basis of the cross sections shown in Section 4.2.2.

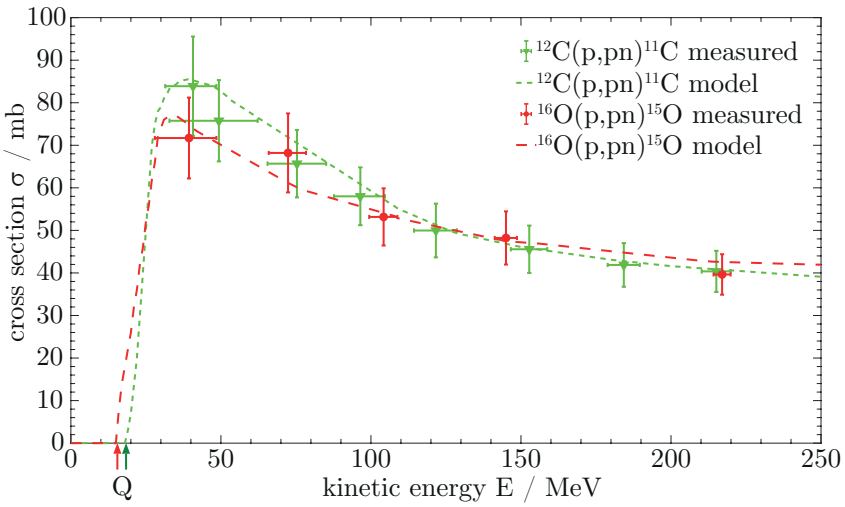


**Figure 4.15:** Cross section models for the $^{12}C(p, pn)^{11}C$ and $^{16}O(p, pn)^{15}O$ reactions based on the measured cross section data in this work and on the calculated Q-values.

The calculated Q-values (18.72 MeV for $^{11}C$ production and 15.66 MeV for $^{15}O$ production, see Figures 4.4 and 4.7) were assumed as reaction thresholds. For the sake of clarity the reference data from the literature which were also used as guidance for the models are not shown in Figure 4.15. The results of the proton transport calculation using the $^{12}C(p, pn)^{11}C$ and $^{16}O(p, pn)^{15}O$ cross sections presented in this work and the $^{16}O(p, X)^{11}C$ and $^{16}O(p, X)^{13}N$ cross sections published by Bauer et al. [77] are shown in Figure 4.16 where the calculated profiles are compared with profiles measured with a PET scanner reported by Espana et al. [122]. The depth in the tissue equivalent gel phantom was converted into water equivalent depth with a conversion factor determined by TOPAS simulations. Considering the noise in the measured activity profiles their shapes are well reproduced for both irradiation protocols (the 5 min protocol being dominated by $^{15}O$, and the 30 min protocol being dominated by $^{11}C$) by the transport calculation using the cross section tables shown in Figure 4.15. This is in contrast to the original work by Espana et al. [122] where standard ICRU and EXFOR cross section tables were applied and none of them could reproduce both the $^{11}C$ and $^{15}O$ profiles accurately. As already pointed out by Espana et al. [122] the tails behind the distal edges of the measured activity profiles are artifacts due to background noise and PET image reconstruction and can therefore be neglected. As seen in comparison with the dose profiles the distal edges of the activity profiles lie some mm before the distal edge of the Bragg curve. This shift is well-known and is due to the threshold energies of the reactions producing the $\beta^+$-emitters (see also Figure 4.4 and 4.7).
This example shows that the calculation of activity depth profiles for protons does not require a full Monte Carlo simulation but only the proton spectrum as a function of depth (which is e.g. available in typical treatment planning systems as basic data) because the created target fragments do not need to be transported. For this kind of calculations cross

section tables can be generated using the cross section data presented in Section 4.2.2 and the respective Q-values. However, in the case of $^{12}$C ions, the projectile fragments are produced with velocities similar to the projectiles and therefore also need to be transported by the code used for calculation of the reference pattern. This is more complex and a typical problem where at least a partial [204] or even a full Monte Carlo simulation [205] is required.

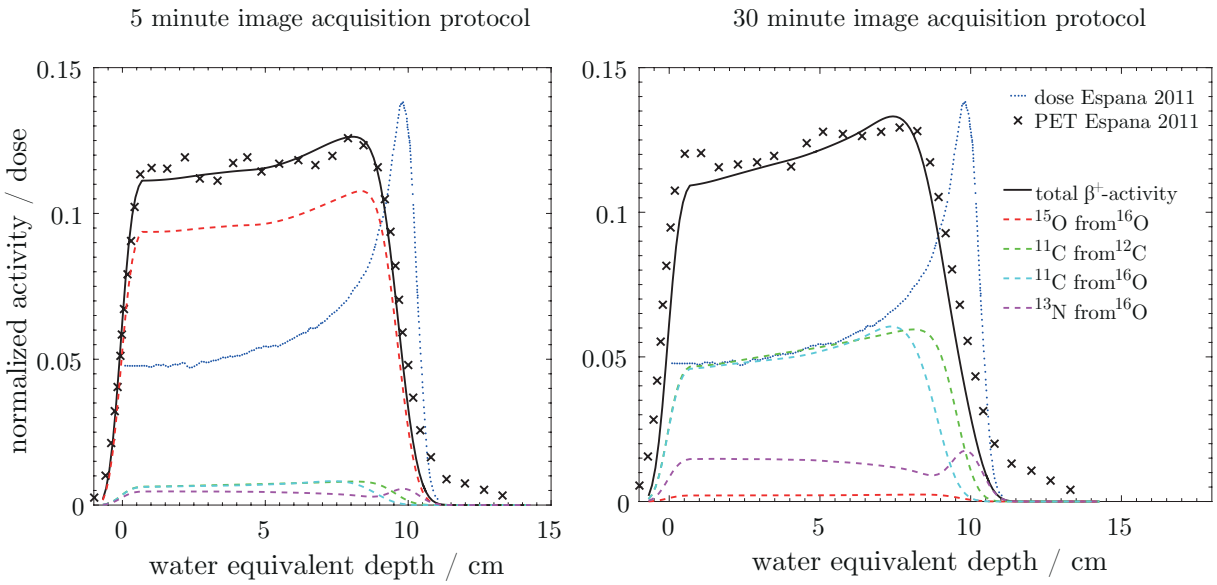


**Figure 4.16:** Measured depth dose distribution in water and $\beta^+$-activity profiles in a tissue equivalent gel phantom irradiated with a 116 MeV proton beam from [122] compared with a proton transport calculation (performed by W. Adi, JLU) based on the measured $^{12}$C(p, pn)$^{11}$C and $^{16}$O(p, pn)$^{15}$O cross sections presented in this work and the $^{16}$O(p, X)$^{11}$C and $^{16}$O(p, X)$^{13}$N cross sections published by Bauer et al. [77]. The activity profiles were obtained with different PET scanner protocols (for 5 min shortly after the irradiation, left panel and for 30 min with a 15 min delay, right panel).

# 5 Conclusion and Outlook

The aim of the present work was to measure nuclear reaction cross sections that can serve as reference data for the optimization of radiation transport codes used in proton and heavy ion therapy. The focus was on charge- and mass-changing cross sections for $^{4}$He ions on H, C, O and Si targets and on cross sections for the production of PET isotopes ($^{10}$C, $^{11}$C and $^{15}$O) by protons and $^{12}$C ions on C and O targets. The former are of particular importance for dose calculation in radiotherapy with $^{4}$He ions, as planned at HIT, and the latter are relevant in the scope of in-vivo range verification of proton and $^{12}$C ion therapy by means of positron emission tomography (PT-PET). The $^{4}$He ion experiments described in this work were performed at HIT while the proton and $^{12}$C ion experiments were carried out at MIT.

Significant improvements in the $^{4}$He dose calculation accuracy of the Monte Carlo codes Geant4 and FLUKA as well as the TRiP98 treatment planning system were achieved by adjusting the nuclear reaction models using the $^{4}$He fragmentation cross sections obtained in the experiments described in this thesis [146, 147]. With the adjusted nuclear reaction model, the FLUKA code is able to calculate $^{4}$He dose distributions with a sub-percent level accuracy [201]. This will be beneficial for the future clinical use of $^{4}$He ions at HIT where the treatment of cancer patients with $^{4}$He ions is currently being prepared. The latest $^{4}$He basic dataset at HIT has been calculated with the FLUKA development version 2018.2 where the $^{4}$He nuclear reaction model is based on the present experimental cross sections. Therefore, future $^{4}$He ion patients will directly profit from the improved dose calculation accuracy resulting from the basic nuclear physics experiments performed within this thesis. The impact of the adjustment to the $^{4}$He nuclear reaction models on the RBE was investigated by means of LEM IV calculations. The effects on RBE profiles were found to be moderate but non-negligible, especially in the Bragg peak region and for radioresistant tissues. Remarkably, the radiobiological uncertainties partly compensate the physical dose calculation uncertainties.

A comparison of the measured cross section data for the production of PET isotopes by protons and $^{12}$C ions [151] with the prediction by the FLUKA models [200] indicates that also for these reactions, in particular for the reaction channels involving $^{12}$C projectiles, significant improvements to the nuclear reaction models can be achieved on basis of the new experimental data. This will improve the accuracy of the code in predicting $\beta^{+}$-activity patterns in particle therapy patients and contribute to a higher precision of the PT-PET in-vivo range verification method.

In future experiments, the $^{4}$He projectile fragmentation studies could be extended to other targets, e.g. calcium, which is important for calculation of radiation transport through bone tissue. Additionally, the measurement of double-differential yields would be interesting and could improve not only the total reaction cross section models but also the fragmentation models in heavy ion transport codes. Such measurements could be realized by measuring time-of-flight spectra with the detector telescope positioned at different angles. Measurements at energies beyond 220 MeV/u would be relevant to space radiation protection. The study on the production of PET isotopes can also be extended to $^{4}$He projectiles, which is still relatively unexplored.

# Bibliography


[1] Durante, M., Orecchia, R. & Loeffler, J. S. Charged-particle therapy in cancer: clinical uses and future perspectives. *Nature Reviews Clinical Oncology* **14**, 483–495 (2017).

[2] Schardt, D., Elsässer, T. & Schulz-Ertner, D. Heavy-ion tumor therapy: Physical and radiobiological benefits. *Reviews of Modern Physics* **82**, 383–425 (2010).

[3] Newhauser, W. D. & Zhang, R. The physics of proton therapy. *Physics in Medicine and Biology* **60**, R155–R209 (2015).

[4] Krämer, M., Scifoni, E., Schuy, C., Rovituso, M., Tinganelli, W., Maier, A., Kaderka, R., Kraft-Weyrather, W., Brons, S., Tessonnier, T., Parodi, K. & Durante, M. Helium ions for radiotherapy? Physical and biological verifications of a novel treatment modality. *Medical Physics* **43**, 1995–2003 (2016).

[5] Haberer, T., Debus, J., Eickhoff, H., Jäkel, O., Schulz-Ertner, D. & Weber, U. The Heidelberg Ion Therapy Center. *Radiotherapy and Oncology* **73**, 186–190 (2004).

[6] Saunders, W., Castro, J. R., Chen, G. T. Y., Collier, J. M., Zink, S. R., Pitluck, S., Char, D., Gutin, P., Gauger, G., Tobias, C. A. & Alpen, E. L. Helium-ion radiation therapy at the Lawrence Berkeley Laboratory: Recent results of a Northern California Oncology Group clinical trial. *Radiation Research* **104**, 227–234 (1985).

[7] Ludewigt, B. A., Chu, W. T., Phillips, M. H. & Renner, T. R. Accelerated helium-ion beams for radiotherapy and stereotactic radiosurgery. *Medical Physics* **18**, 36–42 (1991).

[8] Agostinelli, S. et al. GEANT4 - a simulation toolkit. *Nuclear Instruments and Methods in Physics Research A* **506**, 250–303 (2003).

[9] Ferrari, A., Sala, P. R., Fassò, A. & Ranft, J. FLUKA: a multi-particle transport code. *CERN-2005-10, INFN/TC_05/11, SLAC-R-773* (2005).

[10] Böhlen, T. T., Cerutti, F., Chin, M. P. W., Fassò, A., Ferrari, A., Ortega, P. G., Mairani, A., Sala, P. R., Smirnov, G. & Vlachoudis, V. The FLUKA Code: Developments and Challenges for High Energy and Medical Application. *Nuclear Data Sheets* **120**, 211–214 (2014).

[11] Battistoni, G., Bauer, J., Boehlen, T. T., Cerutti, F., Chin, M. P. W., Dos Santos Augusto, R., Ferrari, A., Ortega, P. G., Kozlowska, W., Magro, G., Mairani, A., Parodi, K., Sala, P. R., Schoofs, T., P. Tessonnier & Vlachoudis, V. The FLUKA Code: An Accurate Simulation Tool for Particle Therapy. *Frontiers in Oncology* **11**, 1–24 (2016).

[12] Durante, M. & Paganetti, H. Nuclear physics in particle therapy: a review. *Reports on Progress in Physics* **79**, 096702 (2016).

[13] Baumann, K.-S., Horst, F., Zink, K. & Gomà, C. Comparison of PENH, FLUKA, and Geant4/TOPAS for absorbed dose calculations in air cavities representing ionization chambers in high-energy photon and proton beams. *Medical Physics* **46**, 4639–4653 (2019).

[14] Parodi, K. & Polf, J. C. In vivo range verification in particle therapy. *Medical Physics* **45**, e1037–e1050 (2018).

[15] Enghardt, W., Debus, J., Haberer, T., Hasch, B. G., Hinz, R., Jäkel, O., Krämer, M., Lauckner, K., Pawelke, J. & Pönisch, F. Positron emission tomography for quality assurance of cancer therapy with light ion beams. *Nuclear Physics A* **654**, 1047c–1050c (1999).

[16] Enghardt, W., Crespo, P., Fiedler, F., Hinz, R., Parodi, K., Pawelke, J. & Pönisch, F. Charged hadron tumour therapy monitoring by means of PET. *Nuclear Instruments and Methods in Physics Research A* **525**, 284–288 (2004).

[17] Kraan, A. C. Range verification methods in particle therapy: underlying physics and Monte Carlo modeling. *Frontiers in Oncology* **5**, 150 (2015).

[18] Brahme, A., Roos, J. E. & Lax, I. Solution of an integral equation encountered in rotation therapy. *Physics in Medicine and Biology* **27**, 1221–1229 (1982).

[19] Webb, S. Optimisation of conformal radiotherapy dose distribution by simulated annealing. *Physics in Medicine and Biology* **34**, 1349–1370 (1989).

[20] Bortfeld, T., Bürkelbach, J., Boesecke, R. & Schlegel, W. Methods of image reconstruction from projections applied to conformation radiotherapy. *Physics in Medicine and Biology* **35**, 1423–1434 (1990).

[21] Bortfeld, T. IMRT: a review and preview. *Physics in Medicine and Biology* **51**, R363–379 (2006).

[22] Kawrakow, I. & Rogers, D. W. O. The EGSnrc Code System: Monte Carlo Simulation of Electron and Photon Transport. *NRCC Report PIRS-701* (2003).

[23] Gottschalk, B., Cascio, E. W., Daartz, J. & Wagner, M. S. On the nuclear halo of a proton pencil beam stopping in water. *Physics in Medicine and Biology* **60**, 5627–5654 (2015).

[24] Tommasino, F., Scifoni, E. & Durante, M. New Ions for Therapy. *International Journal of Particle Therapy* **2**, 428–438 (2016).

[25] Wilson, R. R. Radiological use of fast protons. *Radiology* **46**, 487–491 (1946).

[26] Castro, J. R. Heavy Ion Therapy: Bevalac Epoch. *International Symposium on Hadron Therapy* **LBL-35418**, 1–10 (1993).

[27] Chu, W. T., Ludewigt, B. A. & Renner, T. R. Instrumentation for treatment of cancer using proton and light-ion beams. *Review of Scientific Instruments* **64**, 2055 (1993).

[28] Jäkel, O., Schulz-Ertner, D., Karger, C. P., Nikoghosyan, A. & Debus, J. Heavy Ion Therapy: Status and Perspectives. *Technology in Cancer Research and Treatment* **2**, 377–387 (2003).

[29] Jermann, M. Particle Therapy Statistics in 2014. *International Journal of Particle Therapy* **2**, 50–54 (2015).

[30] Kamada, T., Tsujii, H., Blakely, E. A., Debus, J., De Neve, W., Durante, M., Jäkel, O., Mayer, R., Orecchia, R., Pötter, R., Vatnitsky, S. & Chu, W. T. Carbon ion radiotherapy in Japan: an assessment of 20 years of clinical experience. *Lancet Oncology* **16**, e93–e100 (2015).

[31] Kraft, G. Tumor Therapy with Heavy Charged Particles. *Progress in Particle and Nuclear Physics* **45**, 473–544 (2000).

[32] Pedroni, E., Bacher, R., Blattmann, H., Böhringer, T., Coray, A., Lomax, A., Lin, S., Munkel, G., Scheib, S., Schneider, U. & Tourovsky, A. The 200-MeV proton therapy project at the Paul Scherrer Institute: Conceptual design and practical realization. *Medical Physics* **22**, 37–53 (1995).

[33] Haberer, T., Becher, W., Schardt, D. & Kraft, G. Magnetic scanning system for heavy ion therapy. *Nuclear Instruments and Methods in Physics Research A* **330**, 296–305 (1993).

[34] Hall, E. J. Intensity-modulated radiation therapy, protons, and the risk of second cancers. *International Journal of Radiation Oncology, Biology, Physics* **65**, 1–7 (2006).

[35] Krämer, M., Jäkel, O., Haberer, T., Kraft, G., Schardt, D. & Weber, U. Treatment planning for heavy-ion radiotherapy: physical beam model and dose optimization. *Physics in Medicine and Biology* **45**, 3299–3317 (2000).

[36] Krämer, M. & Scholz, M. Treatment planning for heavy-ion radiotherapy: calculation and optimization of biologically effective dose. *Physics in Medicine and Biology* **45**, 3319–3030 (2000).

[37] Badano, L., Benedikt, M., Bryanz, P. J., Crescenti, M., Holy, P., Maier, A. T., Pullia, M., Rossi, S. & Knaus, P. Proton-Ion Medical Machine Studyy (PIMMS). *CERN-TERA Foundation-MedAustron Oncology-2000 Collaboration* **CERN-PS-99-010-DI**, 1–223 (2000).

[38] Grün, R., Friedrich, T., Krämer, M., Zink, K., Durante, M., Engenhart-Cabillic, R. & Scholz, M. Physical and biological factors determining the effective proton range. *Medical Physics* **40**, 111716 (2013).

[39] Eulitz, J., Raschke, F., Schulz, E., Lutz, B., Dutz, A., Löck, S., Wohlfahrt, P., Enghardt, W., Karpowitz, C., Krause, M. & Lühr, A. Predicting late magnetic resonance image changes in glioma patients after proton therapy. *Acta Oncologica* 1–4 (2019).

[40] Sokol, O., Krämer, M., Hild, S., Durante, M. & Scifoni, E. Kill painting of hypoxic tumors with multiple ion beams. *Physics in Medicine and Biology* **64**, 045008 (2019).

[41] Knopf, A. C. & Lomax, A. In vivo proton range verification: a review. *Physics in Medicine and Biology* **58**, R131–160 (2013).

[42] Bert, C. & Durante, M. Motion in radiotherapy: particle therapy. *Physics in Medicine and Biology* **56**, R113–144 (2011).

[43] Durante, M. & Debus, J. Heavy Charged Particles: Does Improved Precision and Higher Biological Effectiveness Translate to Better Outcome in Patients? *Seminars in Radiation Oncology* **28**, 160–167 (2018).

[44] PTCOG patient statistics (2018). URL `http://www.ptcog.ch/index.php/patient-statistics`.

[45] Bethe, H. A. Zur Theorie des Durchgangs schneller Korpuskularstrahlen durch Materie. *Annalen der Physik* **397**, 325–400 (1930).

[46] Bloch, F. Zur Bremsung rasch bewegter Teilchen beim Durchgang durch Materie. *Annalen der Physik* **408**, 285–320 (1933).

[47] Fermi, E. The Ionization Loss of Energy in Gases and in Condensed Materials. *Physical Review* **57**, 485 (1940).

[48] Bichsel, H. Shell corrections in stopping powers. *Physical Review A* **65**, 052709 (2002).

[49] ICRU Report 90: Key Data for Ionizing-Radiation Dosimetry: Measurement Standards and Applications. *Journal of the ICRU* **14** (2016).

[50] Landau, L. On the energy loss of fast particles by ionization. *Journal of Physics (USSR)* **8**, 201–205 (1944).

[51] Kraft, G., Scholz, M. & Bechthold, U. Tumor therapy and track structure. *Radiation and Environmental Biophysics* **38**, 229–237 (1999).

[52] Molière, G. Theorie der Streuung schneller geladener Teilchen II Mehrfach- und Vielfachstreuung. *Zeitschrift für Naturforschung* **3a**, 78–97 (1948).

[53] Bethe, H. A. Molière's Theory of Multiple Scattering. *Physical Review* **89**, 1256–1266 (1953).

[54] Serber, R. Nuclear Reactions at High Energies. *Physical Review* **72**, 1114–1115 (1947).

[55] Townsend, L. W., Wilson, J. W., Norbury, J. W. & Bidasaria, H. B. An Abrasion-Ablation Model Description of Galactic Heavy-Ion Fragmentation. *NASA Technical Paper* **2305** (1984).

[56] Cucinotta, F. A., Townsend, L. W. & Wilson, J. W. Description of Alpha-Nucleus Interaction Cross Sections for Cosmic Ray Shielding Studies. *NASA Technical Paper* **3285** (1993).

[57] Zeitlin, C. & La Tessa, C. The Role of Nuclear Fragmentation in Particle Therapy and Space Radiation Protection. *Frontiers in Oncology* **29**, 2–13 (2016).

[58] Lühr, A., Hansen, D. C., Teiwes, R., Sobolevsky, N., Jäkel, O. & Bassler, N. The impact of modeling nuclear fragmentation on delivered dose and radiobiology in ion therapy. *Physics in Medicine and Biology* **57**, 5169–5185 (2012).

[59] Gottschalk, B., Platais, R. & Paganetti, H. Nuclear interactions of 160 MeV protons stopping in copper: A test of Monte Carlo nuclear models. *Medical Physics* **26**, 2597–2601 (1999).

[60] Patera, V. et al. The FOOT (Fragmentation Of Target) Experiment. *Proceedings of Science* **128**, 1–6 (2017).

[61] Pfuhl, T., Horst, F., Schuy, C. & Weber, U. Dose build-up effects induced by delta electrons and target fragments in proton Bragg curves - measurements and simulations. *Physics in Medicine and Biology* **63**, 175002 (2018).

[62] Giraudo, M., Schuy, C., Weber, U., Rovituso, M., Santin, G., Norbury, J. W., Tracino, E., Menicucci, A., Bocchini, L., Lobascio, C., Durante, M. & La Tessa, C. Accelerator-Based Tests of Shielding Effectiveness of Different Materials and Multilayers using High-Energy Light and Heavy Ions. *Radiation Research* **190**, 526–537 (2018).

[63] MacCabee, H. D. & Ritter, M. A. Fragmentation of High-Energy Oxygen-Ion Beams in Water. *Radiation Research* **60**, 409–421 (1974).

[64] Schimmerling, W., Miller, J., Wong, M., Rapkin, M., Howard, J., Spieler, H. G. & Jarret, B. V. The Fragmentation of 670 AMeV Neon-20 as a Function of Depth in Water: I. Experiment. *Radiation Research* **120**, 36–71 (1989).

[65] Schall, I., Schardt, D., Geissel, H., Irnich, H., Kankeleit, E., Kraft, G., Magel, A., Mohar, M. F., Münzenberg, G., Nickel, F., Scheidenberger, C. & Schwab, W. Charge-changing nuclear reactions of relativistic light-ion beams ($5 \leq Z \leq 10$) passing through thick absorbers. *Nuclear Instruments and Methods in Physics Research Section B* **117**, 221–234 (1996).

[66] Haettner, E., Iwase, H. & Schardt, D. Experimental fragmentation studies with $^{12}$C therapy beams. *Radiation Protection Dosimetry* **122**, 485–487 (2006).

[67] Gunzert-Marx, K., Iwase, H., Schardt, D. & Simon, R. S. Secondary beam fragments produced by 200 MeV u$^{-1}$ $^{12}$C ions in water and their dose contributions in carbon ion radiotherapy. *New Journal of Physics* **10**, 075003 (2008).

[68] Haettner, E., Iwase, H., Krämer, M., Kraft, G. & Schardt, D. Experimental study of nuclear fragmentation of 200 and 400 MeV/u $^{12}$C ions in water for applications in particle therapy. *Physics in Medicine and Biology* **58**, 8265–8279 (2013).

[69] Golovchenko, A. N., Skvarc, J., Yasuda, N., Giacomelli, M., Tretyakova, S. P., Ilic, R., R, B., Toulemonde, M. & Murakami, T. Total charge-changing and partial cross-section measurements in the reactions of $\sim 110 - 250$ MeV/nucleon $^{12}$C in carbon, paraffin, and water. *Physical Review C* **66**, 014609 (2002).

[70] Toshito, T. et al. Measurements of total and partial charge-changing cross sections for $200-$ to $400-$ MeV/nucleon $^{12}$C on water and polycarbonate. *Physical Review C* **75**, 054606 (2007).

[71] Rovituso, M., Schuy, C., Weber, U., Brons, S., Cortés-Giraldo, M. A., La Tessa, C., Piasetzky, E., Izraeli, D., Schardt, D., Toppi, M., Scifoni, E., Krämer, M. & Durante, M. Fragmentation of 120 and 200 MeV $u^{-1}$ $^4$He ions in water and PMMA targets. *Physics in Medicine and Biology* **62**, 1310–1326 (2017).

[72] Marafini, M. *et al.* Secondary radiation measurements for particle therapy applications: nuclear fragmentation produced by $^4$He ion beams in a PMMA target. *Physics in Medicine and Biology* **62**, 1291–1309 (2017).

[73] Aricò, G., Gehrke, T., Jakubek, J., Gallas, R., Berke, S., Jäkel, O., Mairani, A., Ferrari, A. & Martisiková, M. Investigation of mixed ion fields in the forward direction for 220.5 MeV/u helium ion beams: comparison between water and PMMA targets. *Physics in Medicine and Biology* **62**, 8003–8024 (2017).

[74] Nichols, A. L. & Capote, R. Nuclear Data for Medical Applications - Recent Developments and Future Requirements. *Nuclear Data Sheets* **120**, 239–241 (2014).

[75] Parodi, K., Enghardt, W. & Haberer, T. In-beam PET measurements of $\beta^+$ radioactivity induced by proton beams. *Physics in Medicine and Biology* **47**, 21–36 (2002).

[76] Parodi, K., Pönisch, F. & Enghardt, W. Experimental study on the feasibility of in-beam PET for accurate monitoring of proton therapy. *IEEE Transactions on Nuclear Science* **52**, 778–786 (2005).

[77] Bauer, J., Unholtz, D., Kurz, C. & Parodi, K. An experimental approach to improve the Monte Carlo modelling of offline PET/CT-imaging of positron emitters induced by scanned proton beams. *Physics in Medicine and Biology* **58**, 5193–5213 (2013).

[78] Hofmann, T., Pinto, M., Mohammadi, A., Nitta, M., Nishikido, F., Iwao, Y., Tashima, H., Yoshida, E., Chacon, A., Safavi-Naeini, M., Rosenfeld, A., Yamaya, T. & Parodi, K. Dose reconstruction from PET images in carbon ion therapy: a deconvolution approach. *Physics in Medicine and Biology* **64**, 025011 (2019).

[79] Bauer, J., Tessonnier, T., Debus, J. & Parodi, K. Offline imaging pf positron emitters induced by therapeutic helium, carbon and oxygen ion beams with a full-ring PET/CT scanner: experiments in reference targets. *Physics in Medicine and Biology* (2019).

[80] Failla, G. & Henshaw, P. S. The Relative Biological Effectiveness of X-rays and Gamma Rays. *Radiology* **17**, 1–43 (1931).

[81] Harder, D. Die Biophysik der relativen biologischen Wirksamkeit. *Biophysik* **1**, 225–258 (1964).

[82] Neary, G. J. Chromosome Aberrations and the Theory of RBE. *International Journal of Radiation Biology* **9**, 477 (1965).

[83] Ward, J. F. The Complexity of DNA Damage: Relevance to Biological Consequences. *International Journal of Radiation Biology* **66**, 427–433 (1994).

[84] Prise, K. M., Pinto, M., Newman, H. C. & Michael, B. D. A review of studies of ionizing radiation-induced double-strand break clustering. *Radiation Research* **156**, 572–576 (2001).

[85] Friedrich, T., Durante, M. & Scholz, M. Simulation of DSB yield for high LET radiation. *Radiation Protection Dosimetry* **166**, 61–65 (2015).

[86] Kamlah, F., Hänze, J., Arenz, A., Seay, U., Hasan, D., Juricko, J., Bischoff, B., Gottschald, O. R., Fournier, C., Taucher-Scholz, G., Scholz, M., Seeger, W., Engenhart-Cabillic, R. & Rose, F. Comparison of the effects of carbon ion and photon irradiation on the angiogenic response in human lung adenocarcinoma cells. *International Journal of Radiation Oncology, Biology, Physics* **80**, 1541–1549 (2011).

[87] Scholz, M. & Kraft, G. Calculation of Heavy Ion Inactivation Probabilities Based on Track Structure, X Ray Sensitivity and Target Size. *Radiation Protection Dosimetry* **52**, 29–33 (1994).

[88] Elsässer, T. & Scholz, M. Cluster Effects within the Local Effect Model. *Radiation Research* **167**, 319–329 (2007).

[89] Elsässer, T., Kraft-Weyrather, W., Friedrich, T., Durante, M., Iancu, G., Krämer, M., Kragl, G., Brons, S., Winter, M., Weber, K.-J. & Scholz, M. Quantification of the Relative Biological Effectiveness for Ion Beam Radiotherapy: Direct Experimental Comparison of Proton and Carbon Ion Beams and a Novel Approach for Treatment Planning. *International Journal of Radiation Oncology, Biology, Physics* **78**, 1177–1183 (2010).

[90] Friedrich, T., Scholz, U., Elsässer, T., Durante, M. & Scholz, M. Calculation of the biological effects of ion beams based on the microscopic spatial damage distribution pattern. *International Journal of Radiation Biology* **88**, 103–107 (2012).

[91] Grün, R., Friedrich, T., Krämer, M., Zink, K., Durante, M., Engenhart-Cabillic, R. & Scholz, M. Assessment of potential advantages of relevant ions for particle therapy: A model based study. *Medical Physics* **42**, 1037 (2015).

[92] Blakely, E. A., Tobias, C. A., Ngo, F. Q. H. & Curtis, S. B. Physical and Cellular Radiobiological Properties of Heavy Ions in Relation to Cancer Therapy Application. *Biological and Medical Research with Accelerated Heavy Ions at the Bevalac* **LBL-11220**, 73–88 (1980).

[93] Weber, U. & Kraft, G. Comparison of carbon ions versus protons. *Cancer Journal* **15**, 325–332 (2009).

[94] Paganetti, H., Blakely, E., Carabe-Fernandez, A., Carlson, D. J., Das, I. J., Dong, L., Grosshans, D., Held, K. D., Mohan, R., Moiseenko, V., Niemierko, A., Stewart, R. D. & Willers, H. Report of the AAPM TG-256 on the relative biological effectiveness of proton beams in radiation therapy. *Medical Physics* **46**, e53–e78 (2019).

[95] Grün, R., Friedrich, T., Krämer, M. & Scholz, M. Systematics of relative biological effectiveness measurements for proton radiation along the spread out Bragg peak: Experimental validation of the local effect model. *Physics in Medicine and Biology* **62**, 890–908 (2017).

[96] Wohlfahrt, P., Möhler, C., Stützer, K., Greilich, S. & Richter, C. Dual-energy CT based proton range prediction in head and pelvic tumor patients. *Radiotherapy and Oncology* **125**, 526–533 (2017).

[97] Parodi, K., Mairani, A., Brons, S., Hasch, B. G., Sommerer, F., Naumann, J., Jäkel, O., Haberer, T. & Debus, J. Monte Carlo simulations to support start-up and treatment planning of scanned proton and carbon ion therapy at a synchrotron-based facility. *Physics in Medicine and Biology* **57**, 3759–3784 (2012).

[98] Iancu, G., Krämer, M., Zink, K., Durante, M. & Weber, U. Implementation of an Efficient Monte Carlo Algorithm in TRiP: Physical Dose Calculation. *International Journal of Particle Therapy* **2**, 415–425 (2015).

[99] Metropolis, N. & Ulam, S. The Monte Carlo Method. *Journal of the American Statistical Association* **44**, 335–341 (1949).

[100] von Neumann, J. Various Techniques Used in Connection with Random Digits. *Journal of Research of the National Bureau of Standards* **3**, 36–38 (1951).

[101] Renner, F., Wulff, J., Kapsch, R.-P. & Zink, K. Uncertainties in Monte Carlo-based absorbed dose calculations for an experimental benchmark. *Physics in Medicine and Biology* **60**, 7637 (2015).

[102] Renner, F. Benchmark-Experiment zur Verifikation von Strahlungstransportrechnungen für die Dosimetrie in der Strahlentherapie. *Zeitschrift für Medizinische Physik* **26**, 209–223 (2016).

[103] Mein, S., Dokic, I., Klein, C., Tessonnier, T., Böhlen, T. T., Magro, G., Bauer, J., Ferrari, A., Parodi, K., Haberer, T., Debus, J., Abdollahi, A. & Mairani, A. Biophysical modeling and experimental validation of relative biological effectiveness (RBE) for $^{4}$He ion beam therapy. *Radiation Oncology* **14**, 1–16 (2019).

[104] Sato, T., Niita, K., Matsuda, N., Hashimoto, S., Iwamoto, Y., Furuta, T., Noda, T., S. Ogawa, Iwase, H., Nakashima, H., Fukahori, T., Okumura, K., Kai, T., Chiba, S. & Sihver, L. Overview of particle and heavy ion transport code system PHITS. *Annals of Nuclear Energy* **82**, 110–115 (2015).

[105] Combs, S. E., Nikoghosyan, A., Jaekel, O., Karger, C. P., Haberer, T., Münter, M. W., Huber, P. E., Debus, J. & Schulz-Ertner, D. Carbon ion radiotherapy for pediatric patients and young adults treated for tumors of the skull base. *Cancer* **115**, 1348–1355 (2009).

[106] Blakely, E. A. & Chang, Y. Late effects from hadron therapy. *Radiotherapy and Oncology* **73**, 134–140 (2004).

[107] Facoetti, A., Barcellini, A., Valvo, F. & Pullia, M. The Role of Particle Therapy in the Risk of Radio-induced Second Tumors: A Review of the Literature. *Anticancer Research* **39**, 4613–4617 (2019).

[108] Mohamad, O., Tabuchi, T., Nitta, Y., Nomoto, A., Sato, A., Kasuya, G., Makishima, H., Choy, H., Yamada, S., Morishima, T., Tsuiji, H., Miyashiro, I. & Kamada, T. Risk of subsequent primary cancers after carbon ion radiotherapy, photon radiotherapy, or surgery for localised prostate cancer: a propensity score-weighted, retrospective, cohort study. *The Lancet Oncology* **20**, 674–685 (2019).

[109] Mizumoto, M., Oshiro, Y., Yamamoto, T., Kohzuki, H. & Sakurai, H. Proton Beam Therapy for Pediatric Brain Tumor. *Neurologia medico-chirurgica* **57**, 343–355 (2017).

[110] Mairani, A., Dokic, I., Magro, G., Tessonnier, T., Kamp, F., Carlson, D. J., Ciocca, M., Cerutti, F., Sala, P. R., Ferrari, A., Böhlen, T. T., Jäkel, O., Parodi, K., Debus, J., Abdollahi, A. & Haberer, T. Biologically optimized helium ion plans: calculation approach and its in vitro validation. *Physics in Medicine and Biology* **61**, 4283–4299 (2016).

[111] Knäusl, B., Fuchs, H., Dieckmann, K. & Georg, D. Can particle beam therapy be improved using helium ions? - a planning study focusing on pediatric patients. *Acta Oncologica* **55**, 751–759 (2016).

[112] Tessonnier, T., Mairani, A., Chen, W., Sala, P., Cerutti, F., Ferrari, A., Haberer, T., Debus, J. & Parodi, K. Proton and helium ion radiotherapy for meningioma tumors: a Monte Carlo-based treatment planning comparison. *Radiation Oncology* **13** (2018).

[113] Tessonnier, T., Mairani, A., Brons, S., Sala, P., Cerutti, F., Ferrari, A., Haberer, T., Debus, J. & Parodi, K. Helium ions at the heidelberg ion beam therapy center: comparisons between FLUKA Monte Carlo code predictions and dosimetric measurements. *Physics in Medicine and Biology* **62**, 6784–6803 (2017).

[114] Owen, H., Lomax, A. & Jolly, S. Current and future accelerator technologies for charged particle therapy. *Nuclear Instruments and Methods in Physics Research Section A* **809**, 96–104 (2016).

[115] Jongen, Y., Abs, M., Blondin, A., Kleeven, W., Zaremba, S., Vandeplassche, D., Aleksandrov, V., Gursky, S., Karamyshev, O., Karamysheva, G., Kazarinov, N., Kostromin, S., Morozov, N., Samsonov, E., Shirkov, G., Shevtsov, V., Syresin, E. & Tuzikov, A. Compact superconducting cyclotron C400 for hadron therapy. *Nuclear Instruments and Methods in Physics Research Section A* **624**, 47–53 (2010).

[116] Stichelbaut, F. & Jongen, Y. Properties of an energy degrader for light ions. *Progress in Nuclear Science and Technology* **4**, 272–275 (2014).

[117] Fiorina, E. et al. Monte Carlo simulation tool for online treatment monitoring in hadrontherapy with in-beam PET: A patient study. *Physica Medica* (2018).

[118] Zhu, X., Espana, S., Daartz, J., Liebsch, N., Ouyang, J., Paganetti, H., Bortfeld, T. R. & Fakhri, G. E. Monitoring proton radiation therapy with in-room PET imaging. *Physics in Medicine and Biology* **56**, 4041–4057 (2011).

[119] Parodi, K., Paganetti, H., Shih, H. A., Michaud, S., Loeffler, J. S., Delaney, T. F., Liebsch, N. J., Munzenrider, J. E., Fischman, A. J., Knopf, A. & Bortfeld, T. Patient Study of In Vivo Verification of Beam Delivery and Range, Using Positron Emission Tomography and Computed Tomography Imaging After Proton Therapy. *International Journal of Radiation Oncology, Biology, Physics* **68**, 920–934 (2007).

[120] Combs, S. E., Bauer, J., Unholtz, D., Kurz, C., Welzel, T., Habermehl, D., Haberer, T., Debus, J. & Parodi, K. Monitoring of patients treated with particle therapy using positron-emission-tomography (PET): the MIRANDA study. *BMC Cancer* **12**, 1–6 (2012).

[121] Lühr, A. et al. Dependence of simulated positron emitter yields in ion beam cancer therapy on modeling nuclear fragmentation. *Applied Radiation and Isotopes* **83**, 165–170 (2014).

[122] Espana, S., Zhu, X., Daartz, J., Fakhri, G. E., Bortfeld, T. & Paganetti, H. The reliability of proton-nuclear interaction cross-section data to predict proton-induced PET images in proton therapy. *Physics in Medicine and Biology* **56**, 2687–2698 (2011).

[123] Kox, S., Gamp, A., Perrin, C., Arvieux, J., Bertholet, R., Bruandet, J. F., Buenerd, M., Cherkaoui, R., Cole, A. J., El-Masri, Y., Longequeue, N., Menet, J., Merchez, F. & Viano, J. B. Trends of total reaction cross sections for heavy ion collisions in the intermediate energy range. *Physical Review C* **35**, 1678–1691 (1987).

[124] DeVries, R. M. & Peng, J. C. Nucleus-nucleus total reaction cross sections. *Physical Review C* **22**, 1055–1064 (1980).

[125] Bradt, H. L. & Peters, B. The Heavy Nuclei of the Primary Cosmic Radiation. *Physical Review* **77**, 54–70 (1950).

[126] Kox, S., Gamp, A., Perrin, C., Arvieux, J., Bertholet, R., Bruandet, J. F., Buenerd, M., El Masri, Y., Longequeue, N. & Merchez, F. Transparency effects in heavy-ion collisions over the energy range $100 - 300$ MeV/nucleon. *Physics Letters B* **159**, 15–18 (1985).

[127] Tripathi, R. K., Cucinotta, F. A. & Wilson, J. W. Accurate universal parameterization of absorption cross sections. *Nuclear Instruments and Methods in Physics Research B* **117**, 347–349 (1996).

[128] Tripathi, R. K., Cucinotta, F. A. & Wilson, J. W. Accurate universal parameterization of absorption cross sections III - light systems. *Nuclear Instruments and Methods in Physics Research B* **155**, 349–356 (1999).

[129] Andersen, V., Ballarini, F., Battistoni, G., Campanella, M., Carboni, M., Cerutti, F., Empl, A., Fassò, A., Ferrari, A., Gadioli, E., Garzelli, M. V., Lee, K., Ottolenghi, A., Pelliccioni, M., Pinsky, L. S., Ranft, J., Roesler, S., Sala, P. R. & Wilson, T. L. The FLUKA code for space applications: recent developments. *Advances in Space Research* **34**, 1302–1310 (2004).

[130] Shen, W., Wang, B., Feng, J., Zhan, W., Zhu, Y. & Feng, E. Total reaction cross section for heavy-ion collisions and its relation to the neutron excess degree of freedom. *Nuclear Physics A* **491**, 130–146 (1989).

[131] Durante, M. & Cucinotta, F. A. Physical basis of radiation protection in space travel. *Reviews of Modern Physics* **83**, 1245 (2011).

[132] Norbury, J. W. & Slaba, T. C. Space radiation accelerator experiments - The role of neutrons and light ions. *Life Sciences in Space Research* **3**, 90–94 (2014).

[133] Santin, G., Ivanchenko, V., Evans, H., Nieminen, P. & Daly, E. GRAS: A General-Purpose 3-D Modular Simulation Tool for Space Environment Effects Analysis. *IEEE Transactions on Nuclear Science* **52**, 2294–2299 (2005).

[134] Dementyev, A. V. & Sobolevsky, N. M. SHIELD - universal Monte Carlo hadron transport code: scope and applications. *Radiation Measurements* **30**, 553–557 (1999).

[135] Wilson, J. W., Badavi, F. F., Cucinotta, F. A., Shinn, J. L., Badhwar, G. D., Silberberg, R., Tsao, C. H., Townsend, L. W. & Tripathi, R. L. HZETRN: Description of a free-space ion and nucleon transport and shielding computer program. *NASA Technical Paper* **3495** (1995).

[136] Norbury, J. W. Nuclear physics and space radiation. *Journal of Physics: Conference Series* **381**, 012117 (2012).

[137] Norbury, J. W., Miller, J., Adamczyk, A. M., Heilbronn, L. H., Townsend, L. W., Blattnig, S. R., Norman, R. B., Guetersloh, S. B. & Zeitlin, C. J. Nuclear data for space radiation. *Radiation Measurements* **47**, 315–363 (2012).

[138] Knoll, G. F. *Radiation Detection and Measurement* (Wiley, 1989), 2 edn.

[139] Novotny, R. The $BaF_2$ spectrometer TAPS: A system for high energy photon and neutral meson detection. *Nuclear Tracks and Radiation Measurements* **21**, 23–26 (1993).

[140] Laval, M., Moszynski, M., Allemand, R., Cormoreche, E., Guinet, P., Odru, R. & Vacher, J. Barium fluoride - Inorganic scintillator for subnanosecond timing. *Nuclear Instruments and Methods in Physics Research* **206**, 169–176 (1983).

[141] Novotny, R., Döring, W., Hejny, V., Kotulla, M., Krusche, B., Metag, V., Nold, M., Ströher, H. & Wolf, M. A Plastic-$BaF_2$ Phoswich Telescope for Charged/Neutral Particle and Photon Detection. *IEEE Transactions on Nuclear Science* **43**, 1260–1266 (1996).

[142] Agodi, C., Alba, R., Bellia, G., Coniglione, R., Zoppo, A. D., Maiolino, C., Migneco, E., Piatelli, P., Sapienza, P. & Chen, Y. $BaF_2$ scintillator: A stand-alone detector for $\gamma$-rays and light charged particles. *Nuclear Instruments and Methods in Physics Research A* **269**, 595–598 (1988).

[143] Zeitlin, C., Guetersloh, S., Heilbronn, L., Miller, J., Fukumura, A., Iwata, Y., Murakami, T., Sihver, L. & Mancusi, D. Fragmentation cross sections of medium-energy $^{35}$Cl, $^{40}$Ar, and $^{48}$Ti beams on elemental targets. *Physical Review C* **77**, 034605 (2008).

[144] Goulding, F. S. Heavy-Ion Identification Using Detector Telescopes. *Treatise on Heavy-Ion Science* 225–271 (1985).

[145] Brun, R. & Rademakers, F. ROOT - An Object Oriented Data Analysis Framework. *Nuclear Instruments and Methods in Physics Research A* **389**, 81–86 (1997).

[146] Horst, F., Schuy, C., Weber, U., Brinkmann, K.-T. & Zink, K. Measurement of charge- and mass-changing cross sections for $^{4}$He $+^{12}$ C collisions in the energy range 80-220 MeV/u for applications in ion beam therapy. *Physical Review C* **96**, 024624 (2017).

[147] Horst, F., Aricò, G., Brinkmann, K.-T., Brons, S., Ferrari, A., Haberer, T., Mairani, A., Parodi, K., Reidel, C.-A., Weber, U., Zink, K. & Schuy, C. Measurement of $^{4}$He charge- and mass-changing cross sections on H, C, O, and Si targets in the energy range $70 - 220$ MeV/u for radiation transport calculations in ion-beam therapy. *Physical Review C* **99**, 014603 (2019).

[148] Valin, I. et al. A reticle size CMOS pixel sensor dedicated to the STAR HFT. *Journal of Instrumentation* **7**, C01102 (2012).

[149] Gunzert-Marx, K., Schardt, D., Simon, R. S., Gutermuth, F., Radon, T., Dangendorf, V. & Nolte, R. Response of a $BaF_2$ scintillation detector to quasi-monoenergetic fast neutrons in the range of 45 to 198 MeV. *Nuclear Instruments and Methods in Physics Research Section A* **536**, 146–153 (2005).

[150] Zeitlin, C., Miller, J., Guetersloh, S., Heilbronn, L., Fukumura, A., Iwata, Y., Murakami, T., Blattnig, S., Norman, R. & Mashnik, S. Fragmentation of $^{14}$N, $^{16}$O, $^{20}$Ne, and $^{24}$Mg nuclei at 290 to 1000 MeV/nucleon. *Physical Review C* **83**, 034909 (2011).

[151] Horst, F., Adi, W., Aricò, G., Brinkmann, K.-T., Durante, M., Reidel, C.-A., Rovituso, M., Weber, U., Zaunick, H.-G., Zink, K. & Schuy, C. Measurement of PET isotope production cross sections for protons and carbon ions on carbon and oxygen targets for applications in particle therapy range verification. *Physics in Medicine and Biology* **64**, 205012 (2019).

[152] Tobias, C. A., Chatterjee, A. & Smith, A. R. Radioactive fragmentation of $N^{7+}$ ion beam observed in beryllium target. *Physics Letters* **37A**, 119–120 (1971).

[153] Berger, M. J., Hubbell, J. H., Seltzer, S. M., Chang, J., Coursey, J. S., Sukumar, R., Zucker, D. S. & Olsen, K. XCOM: Photon Cross Sections Database. *NIST Standard Reference Database 8 (XGAM)* (2010).

[154] Eckerman, K. F., Westfall, R. J., Ryman, J. C. & Cristy, M. Availability of Nuclear Decay Data in Electronic Form, Including Beta Spectra not Previously Published. *Health Physics* **67**, 338–345 (1994).

[155] Levin, C. S. & Hoffman, E. J. Calculation of positron range and its effect on the fundamental limit of positron emission tomography system spatial resolution. *Physics in Medicine and Biology* **781-799**, 781–799 (1999).

[156] Stöckmann, H.-J. A new method to analyse composite exponential decay curves. *Nuclear Instruments and Methods* **150**, 273–281 (1978).

[157] Perl, J., Shin, J., Schuemann, J., Faddegon, B. & Paganetti, H. TOPAS: an innovative proton Monte Carlo platform for research and clinical applications. *Medical Physics* **39**, 6818–6837 (2012).

[158] Ferrari, A. & Sala, P. R. The Physics of High Energy Reactions. *Proceedings of the Workshop on Nuclear Reaction Data and Nuclear Reactors* 424 (1998).

[159] Sorge, H. Flavor production in Pb(160A GeV) on Pb collisions: Effect of color ropes and hadronic rescattering. *Physical Review C* **52**, 3291 (1995).

[160] Cerutti, F., Battistoni, G., Capezzali, G., Colleoni, P., Ferrari, A., Gadioli, E., Mairani, A. & Pepe, A. Low energy nucleus-nucleus reactions: the BME approach and its interface with FLUKA. *Proceedings of the 11th International Conference on Nuclear Reaction Mechanisms* 507–5011 (2006).

[161] Geant4 Collaboration. Release 10.5. *Geant4 Physics Reference Manual* (2019).

[162] Sihver, L., Tsao, C. H., Silberberg, R., Kanai, T. & Barghouty, A. F. Total reaction and partial cross section calculations in proton-nucleus ($Z_t \leq 26$) and nucleus-nucleus reactions ($Z_p$ and $Z_t \leq 26$). *Physical Review C* **47**, 1225–1236 (1993).

[163] Lyman, J. & Howard, J. Dosimetry and instrumentation for helium and heavy ions. *International Journal of Radiation Oncology, Biology, Physics* **3**, 81–85 (1977).

[164] Böhlen, T. T., Cerutti, F., Dosanjh, M., Ferrari, A., Gudowska, I., Mairani, A. & Quesada, J. M. Benchmarking nuclear models of FLUKA and GEANT4 for carbon ion therapy. *Physics in Medicine and Biology* **55**, 5833 (2010).

[165] Auce, A., Carlson, R. F., Cox, A. J., Ingemarsson, A., Johansson, R., Renberg, P. U., Sundberg, O., Tibell, G. & Zorro, R. Reaction cross sections for 75-190 MeV alpha particles on targets from $^{12}$C to $^{208}$Pb. *Physical Review C* **50**, 871–879 (1994).

[166] Ingemarsson, A., Nyberg, J., Renberg, P. U., Sundberg, O., Carlson, R. F., Cox, A. J., Auce, A., Johansson, R., Tibelli, G., Khoa, D. T. & Warner, R. E. New results for reaction cross sections of intermediate energy $\alpha$-particles on targets from $^{9}$Be to $^{208}$Pb. *Nuclear Physics A* **676**, 3–31 (2000).

[167] DeVries, R. M., DiGiacomo, N. J., Kapustinsky, J. S., Peng, J. C., Sondheim, W. E., Sunier, J. W., Cramer, J. G., Loveman, R. E., Gruhn, C. R. & Wieman, H. H. Dominance of nucleon-nucleon interactions in $\alpha + ^{12}$ C total reaction cross sections. *Physical Review C* **26**, 301–303 (1982).

[168] Tanihata, I., Hamagaki, H., Hashimoto, O., Nagamiya, S., Shida, Y., Yoshikawa, N., Yamakawa, O., Sugimoto, K., Kobayashi, T., Greiner, D. E., Takahashi, N. & Nojiri, Y. Measurements of interaction cross sections and radii of He isotopes. *Physics Letters* **160B**, 380–384 (1985).

[169] Jaros, J., Wagner, A., Anderson, L., Chamberlain, O., Fuzesy, R. Z., Gallup, J., Gorn, W., Schroeder, L., Shannon, S., Shapiro, G. & Steiner, H. Nucleus-nucleus total cross sections for light nuclei at 1.55 and 2.89 GeV/c per nucleon. *Physical Review C* **18**, 2273–2292 (1978).

[170] Ferrando, P., Webber, W. R., Goret, P., Kish, J. C., Schrier, D. A., Soutoul, A. & Testard, O. Measurement of $^{12}$C, $^{16}$O, and $^{56}$Fe charge changing cross sections in helium at high energy, comparison with cross sections in hydrogen, and application to cosmic-ray propagation. *Physical Review C* **37**, 1490–1501 (1988).

[171] Webber, W. R., Kish, J. C. & Schrier, D. A. Total charge and mass changing cross sections of relativistic nuclei in hydrogen, helium, and carbon targets. *Physical Review C* **41**, 520–532 (1990).

[172] Warner, R. E., Patty, R. A., Voyles, P. M., Nadasen, A., Becchetti, D. F., Brown, J. A., Esbensen, H., Galonsky, A., Kolata, J. J., Kruse, J., Lee, M. Y., Ronningen, R. M., Schwandt, P., von Schwarzenberg, J., Sherrill, B. M., Subotic, K., Wang, J. & Zecher, P. Total reaction and 2n-removal cross sections of 20 - 60A MeV $^{4,6,8}$He, $^{6-9,11}$Li, and $^{10}$Be on Si. *Physical Review C* **54**, 1700–1709 (1996).

[173] Sourkes, A. M., Houdayer, A., van Oers, W. T. H., Carlson, R. F. & Brown, R. E. Total reaction cross section for protons on $^{3}$He and $^{4}$He between 18 and 48 MeV. *Physical Review C* **13**, 451 (1976).

[174] Kozodaev, M. S., Kulyukin, M. M., Sulyaev, R. M., Filippov, A. I. & Shcherbakov, Y. A. Interactions between 630 MeV protons and $^{4}$He nuclei. *Soviet Physics JETP* **38**, 511–516 (1960).

[175] Neumaier, S. R., Alkhazov, G. D., Andronenko, M. N., Dobrovolsky, A. V., Egelhof, P., Gavrilov, G. E., Geissel, H., Irnich, H., Khanzadeev, A. V., Korolev, G. A., Lobodenko, A. A., Münzenberg, G., Mutterer, M., Schwab, W., Seliverstov, D. M., Suzuki, T., Timofeev, N. A., Vorobyov, A. A. & Yatsoura, V. I. Small-angle proton elastic scattering from the neutron-rich isotopes $^{6}$He and $^{8}$He, and from $^{4}$He, at 0.7 GeV in inverse kinematics. *Nuclear Physics A* **712**, 247–268 (2002).

[176] Peng, J. C., DeVries, R. M. & DiGiacomo, N. J. Energy dependence of nucleus-nucleus total cross sections. *Physics Letters B* **98**, 244–247 (1981).

[177] Sihver, L., Lantz, M. & Kohama, A. Improved parametrization of the transparency parameter in Kox and Shen models of total reaction cross sections. *Physical Review C* **89**, 067602 (2014).

[178] Fuchs, H., Ströbele, J., Schreiner, T., Hirtl, A. & Georg, D. A pencil beam algorithm for helium ion beam therapy. *Medical Physics* **39**, 6726–6737 (2012).

[179] Hintz, N. M. & Ramsey, N. F. Excitation Functions to 100 MeV. *Physical Review* **88**, 19–27 (1952).

[180] Aamodt, R. L., Peterson, V. & Phillips, R. $C^{12}(p,pn)C^{11}$ Cross Section from Threshold to 340 MeV. *Physical Review* **88**, 739–744 (1952).

[181] Bäumer, C., Bäcker, C. M., Gerhardt, M., Grusell, E., Koska, B., Kröninger, K., Nitsch, C., Rullkötter, H., Siregar, H. M., Timmermann, B., Verbeek, N., Wulff, J. & Yazgan, A. Measurement of absolute activation cross sections from carbon and aluminum for proton therapy. *Nuclear Instruments and Methods in Physics Research B* **440**, 75–81 (2019).

[182] Bäcker, C. M., Bäumer, C., Gerhardt, M., Kröninger, K., Nitsch, C., Siregar, H. M., Timmermann, B., Verbeek, N., Weingarten, J., Wulff, J. & Yazgan, A. Measurement of nuclear activation cross sections of protons on natural carbon for proton beam energies between 100 and 220 MeV. *Nuclear Instruments and Methods in Physics Research B* **454**, 50–55 (2019).

[183] Gomà, C., Lorentini, S., Meer, D. & Safai, S. Proton beam monitor chamber calibration. *Physics in Medicine and Biology* **59**, 4961–4971 (2014).

[184] Clegg, A. B., Foley, K. J., Salmon, G. L. & Segel, R. E. Gamma Radiation from the Medium Energy Proton Bombardment of Lithium, Beryllium, Boron, Carbon and Nitrogen. *Proceedings of the Physical Society* **78**, 681 (1961).

[185] Valentin, L., Albouy, G., Cohen, J. P. & Gusakow, M. Reactions induites par des protons de 155 MeV sur des noyaux legers. *Physics Letters* **7**, 163–164 (1963).

[186] Matsushita, K., Nishio, T., Tanaka, S., Tsuneda, M., Sugiura, A. & Ieki, K. Measurement of proton-induced target fragmentation cross sections in carbon. *Nuclear Physics A* **946**, 163–164 (2016).

[187] Crandall, W. E., Millburn, G. P., Pyle, R. V. & Birnbaum, W. $C^{12}(x,xn)C^{11}$ and $Al^{27}(x,x2pn)Na^{24}$ Cross Sections at High Energies. *Physical Review* **101**, 329–337 (1956).

[188] Gauvin, H., Lefort, M. & Tarrago, X. Émission d'hélions dans les réactions de spallation. *Nuclear Physics* **39**, 447–463 (1962).

[189] Measday, D. F. The $^{12}C(p,pn)^{11}C$ Reaction from 50 to 160 MeV. *Nuclear Physics* **78**, 476–480 (1966).

[190] Akagi, T., Yagi, M., Yamashita, T., Murakami, M., Yamakawa, Y., Kitamura, K., Ogura, K., Kondo, K. & Kawanishi, S. Experimental study for the production cross sections of positron emitters induced from $^{12}$C and $^{16}$O nuclei by low-energy proton beams. *Radiation Measurements* **59**, 262–269 (2013).

[191] Palmans, H. & Vanitsky, S. M. Comment on 'Proton beam monitor chamber calibration'. *Physics in Medicine and Biology* **61**, 6585–6593 (2016).

[192] Gomà, C., Lorentini, S., Meer, D. & Safai, S. Reply to comment on 'Proton beam monitor chamber calibration'. *Physics in Medicine and Biology* **61**, 6594–6601 (2016).

[193] Salvador, S., Colin, J., Cussol, D., Divay, C., Fontbonne, J.-M. & Labalme, M. Cross section measurements for production of positron emitters for PET imaging in carbon therapy. *Physical Review C* **95**, 044607 (2017).

[194] Smith, A. R., McCaslin, J. B., Geaga, J. V., Hill, J. C. & Vary, J. P. Cross sections for the production of $^{11}$C in C targets by $^{12}$C at relativistic energies. *Physical Review C* **28**, 1614–1617 (1983).

[195] Yashima, H., Uwamino, Y., Iwase, H., Sugita, H., Nakamura, T., Ito, S. & Fukumura, A. Measurement and calculation of radioactivities of spallation products by high-energy heavy ions. *Radiochimica Acta* **91**, 689–696 (2003).

[196] Yashima, H., Uwamino, Y., Iwase, H., Sugita, H., Nakamura, T., Ito, S. & Fukumura, A. Cross sections for the production of residual nuclides by high-energy heavy ions. *Nuclear Instruments and Methods in Physics Research B* **226**, 243–263 (2004).

[197] Valentin, L. Réactions (p,n) et (p,pn) Induites à moyenne énergie sur des noyaux légers. *Nuclear Physics* **62**, 81–102 (1965).

[198] Sajjad, M., Lambrecht, R. M. & Wolf, A. P. Cyclotron Isotopes and Radiopharmaceuticals: XXXVI Investigation of Some Excitation Functions for the Preparation of $^{15}$O, $^{13}$N and $^{11}$C. *Radiochimica Acta* **38**, 57–64 (1985).

[199] Masuda, T., Kataoka, J., Arimoto, M., Takabe, M., Nishio, T., Matsushita, K., Miyake, T., Yamamoto, S., Inaniwa, T. & Toshito, T. Measurement of nuclear reaction cross sections by using Cherenkov radiation toward high-precision proton therapy. *Scientific Reports* **8**, 2570 (2018).

[200] Aricò, G., Battistoni, G., Cerutti, F., Horst, F., Mairani, A., Schuy, C., Weber, U. & Ferrari, A. Benchmarking of FLUKA production cross sections of positron emission tomography isotopes for in-vivo range verification in hadron therapy. *Submitted to EPJ Conference Series* (2020).

[201] Aricò, G., Ferrari, A., Horst, F., Mairani, A., Reidel, C.-A., Schuy, C. & Weber, U. Developments of the nuclear reaction and fragmentation models in FLUKA for ion collisions at therapeutic energies. *Proceedings of the 15th International Conference on Nuclear Reaction Mechanisms, Varenna, Italy* 321–326 (2019).

[202] Mein, S., Kopp, B., Tessonnier, T., Ackermann, B., Ecker, S., Bauer, J., Choi, K., Aricò, G., Ferrari, A., Haberer, T., Debus, J., Abdollahi, A. & Mairani, A. Dosimetric validation of Monte Carlo and analytical dose engines with raster-scanning $^{1}$H, $^{4}$He, $^{12}$C, and $^{16}$O ion-beams using an anthropomorphic phantom. *Physica Medica* **64**, 123–131 (2019).

[203] Grün, R., Friedrich, T., Traneus, E. & Scholz, M. Is the dose-averaged LET a reliable predictor for the relative biological effectiveness? *Medical Physics* **46**, 1064–1074 (2019).

[204] Pönisch, F., Parodi, K., Hasch, B. G. & Enghardt, W. The modelling of positron emitter production and PET imaging during carbon ion therapy. *Physics in Medicine and Biology* **49**, 5217–5232 (2004).

[205] Sommerer, F., Cerutti, F., Parodi, K., Ferrari, A., Enghardt, W. & Aiginger, H. In-beam PET monitoring of mono-energetic $^{16}$O and $^{12}$C beams: experiments and FLUKA simulations for homogeneous targets. *Physics in Medicine and Biology* **54**, 3979–3996 (2009).

**Der Lebenslauf wurde aus der elektronischen Version der Arbeit entfernt.**

**The curriculum vitae was removed from the electronic version of the paper.**

## Publication List

Parts of the research presented in this thesis have been published in the following peer-reviewed publications:

- Horst, F., Adi, W., Aricò, G., Brinkmann, K.-T., Durante, M., Reidel, C.-A., Rovituso, M., Weber, U., Zaunick, H.-G., Zink, K. & Schuy, C. Measurement of PET isotope production cross sections for protons and carbon ions on carbon and oxygen targets for applications in particle therapy range verification. *Physics in Medicine and Biology* **64**, 205012 (2019).
- Horst, F., Aricò, G., Brinkmann, K.-T., Brons, S., Ferrari, A., Haberer, T., Mairani, A., Parodi, K., Reidel, C.-A., Weber, U., Zink, K. & Schuy, C. Measurement of $^{4}$He charge- and mass-changing cross sections on H, C, O, and Si targets in the energy range $70 - 220$ MeV/u for radiation transport calculations in ion-beam therapy. *Physical Review C* **99**, 014603 (2019).
- Horst, F., Schuy, C., Weber, U., Brinkmann, K.-T. & Zink, K. Measurement of charge- and mass-changing cross sections for $^{4}$He $+^{12}$ C collisions in the energy range 80-220 MeV/u for applications in ion beam therapy. *Physical Review C* **96**, 024624 (2017).

Other peer-reviewed publications:

- Aricò, G., Battistoni, G., Cerutti, F., Horst, F., Mairani, A., Schuy, C., Weber, U. & Ferrari, A. Benchmarking of FLUKA production cross sections of positron emission tomography isotopes for in-vivo range verification in hadron therapy. *Submitted to EPJ Conference Series* (2020).
- Burg, J. M., Horst, F., Wulff, J., Timmermann, B., Vorwerk, H. & Zink, K. Optical range determination of clinical proton beams in water. A comparison with standard measurement methods. *Accepted for publication in Physica Medica* (2020).
- Reidel, C.-A., Schuy, C., Horst, F., Ecker, S., Finck, C., Durante, M. & Weber, U. Fluence perturbation from fiducial markers due to edge-scattering measured with pixel sensors for $^{12}$C ion beams. *Accepted for publication in Physics in Medicine and Biology* (2020).

- Pfuhl, T., Horst, F., Schuy, C. & Weber, U. Comment on: "Technical note: Simulation of dose buildup in proton pencil beams". *Medical Physics* **46**, 5876–5877 (2019).
- Baumann, K.-S., Horst, F., Zink, K. & Gomà, C. Comparison of PENH, FLUKA, and Geant4/TOPAS for absorbed dose calculations in air cavities representing ionization chambers in high-energy photon and proton beams. *Medical Physics* **46**, 4639–4653 (2019).
- Rosmej, O. N., Andreev, N. E., Zaehter, S., Zahn, N., Christ, P., Borm, B., Radon, T., Sokolov, A., Pugachev, L. P., Khaghani, D., Horst, F., Borisenko, N. G., Sklizkov, G. & Pimenov, V. G. Interaction of relativistically intense laser pulses with long-scale near critical plasmas for optimization of laser based sources of MeV electrons and gamma-rays. *New Journal of Physics* **21**, 043044 (2019).
- Schuy, C., La Tessa, C., Horst, F., Rovituso, M., Durante, M., Giraudo, M., Bocchini, L., Baricco, M., Castallero, A., Fioreh, G. & Weber, U. Experimental Assessment of Lithium Hydride's Space Radiation Shielding Performance and Monte Carlo Benchmarking. *Radiation Research* **191**, 154–161 (2019).
- Mao, J. Y., Rosmej, O., Ma, Y., Li, M. H., Aurand, B., Gaertner, F., Wang, W. M., Schoenlein, A., Zielbauer, B., Eisenbart, U., Bagnoud, V., Wagner, F., Horst, F., Syha, M., Mathias, S., Li, Y. T., Aeschlimann, M., Chen, L. M. & Kuehl, T. Energy enhancement of the target surface electron by using a 200 TW sub-picosecond laser. *Optics Letters* **43**, 3909–3912 (2018).
- Pfuhl, T., Horst, F., Schuy, C. & Weber, U. Dose build-up effects induced by delta electrons and target fragments in proton Bragg curves - measurements and simulations. *Physics in Medicine and Biology* **63**, 175002 (2018).
- Horst, F., Czarnecki, D., Harder, D. & Zink, K. The absorbed doses to water and the TLD-100 signal contributions associated with the neutron contamination of a clinical 18 MV photon beam. *Radiation Measurements* **106**, 331–335 (2017).
- Horst, F., Fehrenbacher, G. & Zink, K. On the neutron radiation field and air activation around a medical electron linac. *Radiation Protection Dosimetry* **174**, 147–158 (2017).
- Horst, F., Czarnecki, D. & Zink, K. The influence of neutron contamination on dosimetry in external photon beam radiotherapy. *Medical Physics* **42**, 6529–6539 (2015).
- Horst, F., Fehrenbacher, G., Radon, T., Kozlova, E., Rosmej, O., Czarnecki, D., Schrenk, O., Breckow, J. & Zink, K. A TLD-based ten channel system for the spectrometry of bremsstrahlung generated by laser-matter interaction. *Nuclear Instruments and Methods in Physics Research Section A* **782**, 60–76 (2015).

# Eidesstattliche Erklärung

Ich erkläre: Ich habe die vorgelegte Dissertation selbstständig und ohne unerlaubte fremde Hilfe und nur mit den Hilfen angefertigt, die ich in der Dissertation angegeben habe. Alle Textstellen, die wörtlich oder sinngemäß aus veröffentlichten Schriften entnommen sind, und alle Angaben, die auf mündlichen Auskünften beruhen, sind als solche kenntlich gemacht. Ich stimme einer eventuellen Überprüfung meiner Dissertation durch eine Antiplagiat-Software zu. Bei den von mir durchgeführten und in der Dissertation erwähnten Untersuchungen habe ich die Grundsätze guter wissenschaftlicher Praxis, wie sie in der "Satzung der Justus-Liebig-Universität Giessen zur Sicherung guter wissenschaftlicher Praxis" niedergelegt sind, eingehalten.

| | |
|---|---|
| Ort, Datum | Felix Ernst Horst |

# Acknowledgements

I would like to thank all those who contributed directly or indirectly to this work. It was a real pleasure for me to work with so many fantastic people on such interesting topics. I am grateful for everything that I have learned during my PhD time and besides that it was always very fun.
First of all, I thank Prof. Klemens Zink who paved my way for this PhD by strongly supporting me since my time as a Bachelor student. His lectures awakened my interest in the exciting field of radiotherapy and medical physics which now results in this thesis. Whenever I had an idea, he was optimistic and encouraged me to follow it. I also enjoyed a lot our conference visits around the world.
The second person I would like to thank is Prof. Kai-Thomas Brinkmann who kindly accepted me as PhD student. Even if medical physics is not his original field of research he was always very interested in the progress of my work and could contribute a lot with his broad knowledge in nuclear and detector physics. Besides this intellectual input, I am thankful to him for providing us with a lot of experiment hardware, scintillators and electronics - and not to forget also the manpower from his group.
Another person without whom this thesis would not exist and whom I thank very much is Dr. Uli Weber. He invited me to join his newly established radiation physics group at GSI and proposed the topics that I have worked on. In addition to his organizational activities as a group leader he attended almost every experiment and night shift and provided many important suggestions for the measurements. His broad knowledge about particle therapy physics and technology was very helpful at all stages of my work and his availability around the clock still amazes me.
I thank Prof. Marco Durante for being available as a co-examiner. He was always strongly promoting the importance of nuclear physics for heavy ion therapy and radiation biophysics which is highly beneficial for our research. The test beamtimes in Trento, which he organized for us at short notice, saved us a lot of time and furthermore we could enjoy the nice view on the mountains in northern Italy.
I experienced the interdisciplinary character of the GSI biophysics department always as very inspiring. I thank especially my colleagues from the radiation physics group: Dr. Christoph Schuy, Dr. Daria Boscolo, Claire-Anne Reidel and Francesca Luoni. Without Christoph's help in planning, setting up and conducting the experiments as well as the data analysis afterwards, we would never have obtained such nice results. I am also thankful for the other contributions to this work, e.g. the CMOS measurements to align our telescopes and several CAD drawings done by Claire or the many TRiP iterations done by Daria.
I also felt very home in our IMPS corridor at THM where I started studying almost 10 years ago and later learned how to work scientifically. I want to thank my former and recent colleagues, especially those from our radiotherapy group: Dr. Damian Czarnecki, Dr. Philip von Voigts-Rhetz, Kilian Baumann, Ralph Schmidt, Mohamad Alissa, Yuri Simeonov, Jan Burg, Veronika Flatten and also Matthias Witt who works at MIT since a few years.
I also appreciated a lot to work together with the colleagues from the II. Physics Institute

at JLU and thank especially Dr. Hans-Georg Zaunick, René Schubert and Wihan Adi for building all the nice detectors for us.
A special thanks goes to the FLUKA developers, in particular Dr. Alfredo Ferrari and Dr. Giulia Aricò at CERN and Dr. Andrea Mairani at HIT for trust in our work and supporting our experiments. This collaboration, initiated by Prof. Katia Parodi from LMU Munich, showed out to be very fruitful and allowed us to translate our experimental findings into clinical application.
The accelerator and medical physics teams at HIT and MIT are acknowledged for stable operation of their machines during our experimental beamtimes and their kind help even if a problem occurred in the middle of the night. Also our test beamtimes in Trento and Essen worked very smoothly thanks to their technical crews.
Many of the above mentioned people helped me proofreading. Additionally, I thank Prof. Gerhard Kraft for helping me writing the history chapter and Dr. Thomas Friedrich for help with the radiobiology chapter.
Finally, I also want to say thanks to my non-academic environment for support and also for diversion from the scientific stress that is sometimes unavoidable.